ASTROGLIOSIS AND NEUROINFLAMMATION UNDERLIE SCOLIOSIS UPON CILIA DYSFUNCTION

Morgane Djebar[1], Isabelle Anselme[1], Guillaume Pezeron[2], Pierre-Luc Bardet[1], Yasmine Cantaut-Belarif[3], Alexis Eschstruth[1], Diego López Santos[1], Hélène Le Ribeuz[1], Arnim Jenett[4], Hanane Khoury[1], Joëlle Véziers[5], Caroline Parmentier[6], Aurélie Hirschler[7], Christine Carapito[7], Ruxandra Bachmann-Gagescu[8], Sylvie Schneider-Maunoury[1]* and Christine Vesque[1]*

1 Sorbonne Université, CNRS UMR7622, INSERM U1156, Institut de Biologie Paris Seine (IBPS) - Developmental Biology Unit, 75005, Paris, France
2 Molecular Physiology and Adaptation (PhyMA - UMR7221), Muséum National d'Histoire Naturelle, CNRS, Paris, France
3 Institut du Cerveau et de la Moelle épinière (ICM), Sorbonne Université, Inserm U 1127, CNRS UMR 7225, F-75013, Paris, France
4 TEFOR Paris-Saclay, CNRS UMS2010 / INRA UMS1451, Université Paris-Saclay.
5 Inserm UMR 1229, CHU Nantes PHU4 OTONN, SC3M facility, Inserm UMS 016, CNRS 3556, Université de Nantes, Nantes, France.
6 Sorbonne Université, CNRS UMR8246, INSERM U1130, Institut de Biologie Paris Seine (IBPS) – Neurosciences Paris Seine (NPS), 75005, Paris, France
7 Laboratoire de Spectrométrie de Masse Bio-Organique, IPHC, UMR 7178, Université de Strasbourg, CNRS, Infrastructure Nationale de Protéomique ProFI - FR2048, Strasbourg, France.
8 Institute of Medical Genetics, University of Zurich, Wagistrasse 12, 8952 Schlieren, Zurich, Switzerland; Institute of Molecular Life Sciences, University of Zurich, Winterthurerstrassse 190, 8057 Zurich, Switzerland
* Co-corresponding authors, co-last authors.
sylvie.schneider-maunoury@sorbonne-universite.fr
christine.vesque@sorbonne-universite.fr

ABSTRACT

Cilia defects lead to scoliosis in zebrafish, but the underlying pathogenic mechanisms are poorly understood and may diverge depending on the mutated gene. Here, we dissected the mechanisms of scoliosis onset in a zebrafish mutant for the *rpgrip1l* gene encoding a ciliary transition zone protein. *rpgrip1l* mutant fish developed scoliosis with near-total penetrance but asynchronous onset in juveniles. Taking advantage of this asynchrony, we found that curvature onset was preceded by ventricle dilations and was concomitant to the perturbation of Reissner fiber polymerization and to the loss of multiciliated tufts around the subcommissural organ. Rescue experiments showed that Rpgrip1l was exclusively required in *foxj1a*-expressing cells to prevent axis curvature. Genetic interactions investigations ruled out Urp1/2 levels as a main driver of scoliosis in *rpgrip1* mutants. Transcriptomic and proteomic studies identified neuroinflammation associated with increased Annexin levels as a potential mechanism of scoliosis development in *rpgrip1l* juveniles. Investigating the cell types associated with *annexin2* over-expression, we uncovered astrogliosis, arising in glial cells surrounding the diencephalic and rhombencephalic ventricles just before scoliosis onset and increasing with time in severity. Anti-inflammatory drug treatment reduced scoliosis penetrance and severity and this correlated with reduced astrogliosis and macrophage/microglia enrichment around the diencephalic ventricle. Mutation of the *cep290* gene encoding another transition zone protein also associated astrogliosis with scoliosis. Thus, we propose astrogliosis induced by perturbed ventricular homeostasis and associated with immune cell activation as a novel pathogenic mechanism of zebrafish scoliosis caused by cilia dysfunction.

INTRODUCTION

Idiopathic scoliosis (IS) is a 3D rotation of the spine without vertebral anomalies that affects about 3% of adolescents worldwide. Its etiology remained mysterious, mainly because of the lack of appropriate animal models and the complexity of its inheritance profile in large families presenting a severe scoliosis trait (Patten et al., 2015). Since the description of the first IS model in the zebrafish *ptk7* gene mutant (Hayes et al., 2014), a number of mutants for genes encoding ciliary proteins were shown to develop scoliosis at late larval and juvenile stage (4 to 12 weeks post-fertilization, wpf) without any vertebral fusion or fracture, highlighting the link between cilia function and straight axis maintenance in that species (Grimes et al., 2016; Wang et al., 2022).

Cilia are microtubular organelles with sensory and/or motile functions. Zebrafish mutants in genes involved in cilia motility or in intraflagellar transport display severe embryonic axis curvature and are usually not viable beyond larval stages (Grimes et al., 2016; Rose et al., 2020). In contrast, mutants in genes implicated in ciliary gating or ciliary trafficking encoding respectively components of the transition zone (TZ) or of the BBsome complex survive to adult stage and develop scoliosis with variable penetrance (Bentley-Ford et al., 2022; Masek et al., 2022; Song et al., 2020; Wang et al., 2022). The molecular basis for these differences is still poorly understood, even if progress has been made in our understanding of zebrafish scoliosis. Cilia-driven movements of the cerebrospinal fluid (CSF) are involved in zebrafish axis straightness, both in embryos and juveniles (Boswell and Ciruna, 2017; Grimes et al., 2016) and are tightly linked to the assembly and maintenance of the Reissner fiber (RF), a SCO-spondin polymer secreted by the subcommissural organ (SCO) and running down the brain and spinal cord CSF-filled cavities (Cantaut-Belarif et al., 2018). RF loss at embryonic stage in null *sspo* mutants generates ventral curvatures of the posterior axis of the body and is lethal while its loss at juvenile stage in hypomorphic *sspo* mutants triggers scoliosis with full penetrance (Cantaut-Belarif et al., 2018; Rose et al., 2020; Troutwine et al., 2020). Signaling downstream of the RF in embryos implicates Urp1 and Urp2, two neuropeptides of the Urotensin 2 family expressed in ventral CSF-contacting neurons (CSF-cNs), which act on dorsal muscles in embryos and larvae (Cantaut-Belarif et al., 2020; Gaillard et al., 2023; Lu et al., 2020; Zhang et al., 2018). Their combined mutations or the mutation of their receptor gene *uts2r3* lead to scoliosis

at adult stages (Bearce et al., 2022; Gaillard et al., 2023; Zhang et al., 2018). However, whether RF maintenance and Urp1/2 signaling are perturbed in juvenile scoliotic mutants of genes encoding TZ proteins ("TZ mutants") and how these perturbations are linked to scoliosis is unknown, especially because TZ mutants do not display any sign of embryonic or larval cilia motility defects (Wang et al., 2022). Moreover, two scoliotic models develop axial curvature while maintaining a RF showing that their curvature onset occurs independently of RF loss (Meyer-Miner et al., 2022; Xie et al., 2023). Finally, neuro-inflammation has been described in a small subset of zebrafish IS models for which anti-inflammatory/anti-oxidant treatments (with NAC or NACET) partially rescue scoliosis penetrance and severity (Rose et al., 2020; Van Gennip et al., 2018).

In this paper we dissect the mechanisms of scoliosis appearance in a novel deletion allele of the zebrafish TZ *rpgrip1l* gene. *RPGRIP1L* mutations have been found in neurodevelopmental ciliopathies, Meckel syndrome (MKS) and Joubert syndrome (JS) (Delous et al., 2007)(Arts et al., 2007) characterized by severe brain malformations. Other organs such as the kidney and liver are variably affected. Some JS patients also present with severe scoliosis, but this phenotypic trait is of variable penetrance (Delous et al., 2007)(Brancati et al., 2008). Functional studies performed in mouse and zebrafish have shown that *Rpgrip1l* is required for proper central nervous system patterning due to complex perturbations of Sonic Hedgehog signaling (in mice) and cilia planar positioning (in mice and zebrafish) (Andreu-Cervera et al., 2021; Mahuzier et al., 2012; Vierkotten et al., 2007). Zebrafish *rpgrip1l* mutants are viable and develop an axis curvature phenotype at juvenile stages with nearly full penetrance. Using a variety of approaches, we show that i) Rpgrip1l is required in ciliated cells surrounding ventricular cavities for maintaining a straight axis; ii) at juvenile stages, *rpgrip1l* mutants develop cilia defects associated with ventricular dilations and loss of the RF; iii) increased *urp1/2* expression in *rpgrip1l* mutants does not account for spine curvature defects; and iv) a pervasive astrogliosis process associated with neuroinflammation participates in scoliosis onset and progression. Finally, we show that astrogliosis is conserved in another zebrafish ciliary TZ mutant, *cep290*, identifying a novel mechanism involved in scoliosis upon ciliary dysfunction.

67 **RESULTS**

68

69 ***Rpgrip1l*** $^{-/-}$ ***fish develop scoliosis asynchronously at juvenile stage***

70 To study the mechanisms of scoliosis appearance upon ciliary dysfunction in zebrafish,
71 we produced a viable zebrafish deletion mutant in the *rpgrip1l* gene encoding a ciliary
72 transition zone protein (*rpgrip1l*$^{\Delta}$, identified in ZFIN as *rpgrip1l*^{bps1}) Supplementary
73 Figure S1A). We made a 26 kb deletion by CRISPR-Cas9 double-cut, which removes
74 22 out of the 26 exons of the protein (Supplementary Figure S1A) and triggers protein
75 truncation at amino-acid (aa) position 88 out of 1256. 90-100% of *rpgrip1l*$^{\Delta/\Delta}$ embryos
76 and larvae were straight (0-10%, depending on the clutch, displayed a sigmoid
77 curvature). They did not display any additional defects found in many ciliary mutant
78 embryos or larvae such as randomized left-right asymmetry, kidney cysts or retinal
79 anomalies (Bachmann-Gagescu et al., 2011; Kramer-Zucker et al., 2005; Tsujikawa
80 and Malicki, 2004)(Figure 1A and Supplementary Figure S1B, D, E). Another allele
81 with a frameshift mutation in exon 4 (*rpgrip1l*^{ex4}, identified in ZFIN as *rpgrip1l*^{bps2})
82 showed a similar phenotype (Supplementary Figure S1A, B). Considering the large
83 size of the deletion, we considered the *rpgrip1l*$^{\Delta}$ allele as a null and called it *rpgrip1l*$^{-/-}$
84 thereafter. *rpgrip1l*$^{-/-}$ animals developed scoliosis during juvenile stages. Scoliosis
85 appearance was asynchronous between clutches, from 4 weeks post fertilization (wpf)
86 (around 1 cm length) to 11 wpf (1.8- 2.3 cm), and also within a clutch. It started with
87 slight upward bending of the tail (the *tail-up* phenotype) and progressed toward severe
88 curvature (Figure 1A, B) with 90% penetrance in adults (100% in females and 80% in
89 males) (Figure 1C). Micro-computed tomography (µCT) at two different stages (5 wpf
90 and 23 wpf) confirmed that spine curvature was three-dimensional and showed no
91 evidence of vertebral fusion, malformation or fracture (Figure 1D-G and Supplementary
92 Movie 1).

93 Thus, the ciliary *rpgrip1l*$^{-/-}$ mutant shows almost totally penetrant, late-onset juvenile
94 scoliosis without vertebral anomalies, making it a valuable model for studying the
95 etiology of human idiopathic scoliosis. Furthermore, the asynchronous onset of
96 curvature is an asset for studying the chronology of early defects leading to scoliosis.

97

98

99 ***Reintroducing* RPGRIP1L *in foxj1a lineages suppresses scoliosis in rpgrip1l$^{-/-}$***
100 ***fish***
101 Since *rpgrip1l* is ubiquitously expressed in zebrafish (Mahuzier et al., 2012), scoliosis
102 could have different tissue origins, including a neurological origin as shown for the *ptk7*
103 and *ktnb1* scoliotic fish (Meyer-Miner et al., 2022; Van Gennip et al., 2018). Indeed, no
104 tissue-specific rescue has been performed in mutants for zebrafish ciliary TZ or BBS
105 genes. We tested if introducing by transgenesis a tagged human RPGRIP1L protein
106 under the control of the *col2a1a (Dale and Topczewski, 2011)* or *foxj1a* (Van Gennip
107 et al., 2018) enhancers (Figure 1H) would reduce scoliosis penetrance and severity.
108 The *foxj1a* enhancer drives expression in motile ciliated cells, among which ependymal
109 cells lining CNS cavities (Van Gennip et al., 2018), while the *col2a1a* regulatory region
110 drives expression in cartilage cells including intervertebral discs and semi-circular
111 canals, tissues that have been proposed to be defective in mammalian scoliosis
112 models (Hitier et al., 2015; Karner et al., 2015). After selecting F1 transgenic fish that
113 expressed the Myc-tagged RPGRIP1L protein in the targeted tissue at 2.5 dpf, we
114 introduced one copy of each transgene into the *rpgrip1l$^{-/-}$* background. The
115 Foxj1a:5XMycRPGRIP1L transgene was sufficient to fully suppress scoliosis in
116 *rpgrip1l$^{-/-}$* fish: none of the transgenic *rpgrip1l$^{-/-}$* fish became scoliotic while virtually all
117 the non-transgenic *rpgrip1l$^{-/-}$* siblings did (Figure 1I, J). In contrast, RPGRIP1L
118 expression triggered by the *col2a1a* promoter did not have any beneficial effect on
119 scoliosis penetrance (Figure 1I, J). In conclusion, *rpgrip1l* expression in *foxj1a*-
120 expressing cells is sufficient to maintain a straight axis.
121
122 ***Rpgrip1l$^{-/-}$ adult fish display cilia defects along CNS cavities***
123 We observed normal cilia in the neural tube of *rpgrip1l$^{-/-}$* embryos (Supplementary
124 Figure S1C). In 3 month-adults, scanning electron microscopy (SEM) at the level of
125 the rhombencephalic ventricle (RhV) showed cilia tufts of multiciliated ependymal cells
126 (MCC) lining the ventricle in controls and straight *rpgrip1l$^{-/-}$* fish (Supplementary Figure
127 S1F-G, F'-G'). In scoliotic *rpgrip1l$^{-/-}$* fish, cilia tufts were sparse and disorganized
128 (Supplementary Figure S1H, H'). Cilia of mono-ciliated ependymal cells were present
129 in *rpgrip1l$^{-/-}$* fish, some of them with irregular shape (Supplementary Figure S1, F", G'',
130 H'' and H''').
131

132 ***MCC defects at SCO level correlate with scoliosis appearance at juvenile stages***
133 We then took advantage of the asynchrony in scoliosis onset to correlate, at a given
134 stage, cilia defects at different levels of the CNS cavities with the spine curvature status
135 (straight or curved) of *rpgrip1l*$^{-/-}$ juveniles. We analyzed cilia defects in three CNS
136 regions implicated in scoliosis appearance: the spinal cord central canal (since
137 scoliosis develops in the spine), the forebrain choroid plexus (fChP) whose cilia defects
138 have been associated with scoliosis in *katnb1*$^{-/-}$ fish (Meyer-Miner et al., 2022) and the
139 subcommissural organ (SCO), which secretes SCO-spondin whose absence leads to
140 scoliosis (Rose et al., 2020; Troutwine et al., 2020).
141 In the spinal cord central canal of 8 wpf juvenile fish, cilia density was reduced to the
142 same extent in *rpgrip1l*$^{-/-}$ fish irrespective of the fish curvature status (Figure 2 A-C, E).
143 In addition, cilia length increased in straight mutants and was more heterogenous than
144 controls in scoliotic mutants (Figure 2 A'-C', D). Arl13b content appeared severely
145 reduced in mutants (Figure 2 A"-C"). In the fChP, mono- and multi-ciliated cell
146 populations were observed with a specific distribution along the anterior-posterior axis,
147 as previously described (D'Gama et al., 2021). At the level of the habenula nuclei, cells
148 of dorsal and ventral midline territories were monociliated, while lateral cells presented
149 multicilia tufts (Supplementary Figure S2 K-K''). *rpgrip1l*$^{-/-}$ juveniles presented an
150 incomplete penetrance of ciliary defects in the fChP, with no correlation between cilia
151 defects and the curvature status (Supplementary Figure S2, L-O'').
152 The SCO lies at the dorsal midline of the diencephalic ventricle (DiV), under the
153 posterior commissure (PC) (Figure 2 G, H, Supplementary Figure 2A, C). Cilia in and
154 around the SCO have not been described previously in zebrafish. We showed that, in
155 control animals, Sco-spondin (Sspo) secreting cells varied in number along SCO
156 length, from 24 cells anteriorly to 6-8 cells posteriorly (Supplementary Figure 2 A, A',
157 C) and were monociliated at all anteroposterior levels (Figure 2G-H, Supplementary
158 Figure 2 A'). The Sspo protein produced from one copy of the transgene Scospondin-
159 GFP^{ut24} (Troutwine et al., 2020) formed cytoplasmic granules around SCO cell nuclei,
160 under emerging primary cilia (Supplementary Figure 2A'). Conversely, MCCs lateral to
161 the SCO did not secrete Sspo and were prominent towards posterior (Figure 2H,
162 Supplementary Figure 2C), as observed in the rat brain (Collins and Woollam, 1979).
163 Monocilia of Sspo secreting cells were still present but appeared longer in straight
164 *rpgrip1l*$^{-/-}$ juveniles and could not be individualized anymore at anterior SCO level in

165 scoliotic fish: we observed a weaker and denser acetylated and glutamylated tubulin
166 staining that likely corresponded to longer intertwined cilia (Figure 2 I, I', K, K'). Lateral
167 multicilia tufts were preserved in straight *rpgrip1l*$^{-/-}$ juveniles (n=5) (Figure 2 J) but were
168 missing at posterior SCO level in tail-up or scoliotic *rpgrip1l*$^{-/-}$ fish (n=7) (Figure 2L).
169 Thus, *rpgrip1l* mutants develop both monocilia and multicilia defects at juvenile stages,
170 but cilia defects in the spinal cord and in the fChP do not correlate with axis curvature
171 status of the fish. By contrast, the loss of MCC cilia at the SCO strictly correlates with
172 scoliosis onset, suggesting a causal relationship.
173
174 ***Rpgrip1l*$^{-/-}$ *juveniles show ventricular dilations and loss of the Reissner fiber at***
175 ***scoliosis onset***
176
177 Ciliary beating is an essential actor of CSF flow and of ventricular development in
178 zebrafish larvae (Kramer-Zucker et al., 2005) (Olstad et al., 2019). Thus, ciliary defects
179 in the brain and spinal cord of *rpgrip1l*$^{-/-}$ fish could lead to abnormal ventricular and
180 central canal volume and content. In the spinal cord, the lumen of the central canal
181 was enlarged at thoracic and lumbar levels in all *rpgrip1l*$^{-/-}$ mutant juveniles, with no
182 correlation to the axis curvature status (Figure 2 A-C; F). To determine the timing of
183 brain ventricular dilations relative to scoliosis, we analyzed ventricular volume at the
184 onset of spine curvature (Figure 3A-G). Ventricular reconstruction was performed on
185 cleared brains of 4 control and 4 *rpgrip1l*$^{-/-}$ (3 tail-up and 1 straight) fish at 5 wpf, stained
186 with ZO1 to highlight the ventricular border and with DiI to outline brain shape, focusing
187 on the RhV at the level of the posterior midbrain and hindbrain (Figure 3A-D). We
188 identified a significant increase in ventricle volume in *rpgrip1l*$^{-/-}$ fish compared to
189 controls, that was restricted to the ventral regions of the RhV in regions ROI4.4 (green
190 sphere in Figure 3C) and ROI6 (green sphere in Figure 3D), as confirmed by numerical
191 sections (Figure 3E, G). Ventricle dilations were also present, although to a lesser
192 extent, in the RhV of the unique straight *rpgrip1l*$^{-/-}$ fish of this study (green squares and
193 triangle in Figure 3F, G).
194 Defective ependymal ciliogenesis has been associated with abnormal CSF flow and
195 defective Reissner Fiber (RF) maintenance in several scoliotic zebrafish models
196 (Grimes et al., 2016)(Rose et al., 2020). The RF runs along the length of the body,
197 within brain ventricles and central canal (Figure 3H). It is mainly composed of Sspo

198 secreted by the SCO and floor plate (FP) and its loss at juvenile stages triggers
199 scoliosis in zebrafish (Rose et al., 2020)(Troutwine et al., 2020). To visualize the RF,
200 we used an antiserum that labels the RF in zebrafish embryos (Didier et al.,
201 1995)(Cantaut-Belarif et al., 2018) and we confirmed the results by introducing one
202 copy of the *sspo-GFP* knock-in allele, sco-spondin-GFP^{ut24,} (Troutwine et al., 2020) by
203 genetic cross into *rpgrip1l*$^{-/-}$ animals. The RF formed normally in *rpgrip1l*$^{-/-}$ embryos, as
204 expected given the absence of embryonic curvature (Supplementary Figure S1 C). To
205 study its maintenance in *rpgrip1l*$^{-/-}$ juveniles, we immunostained spinal cord longitudinal
206 sections of 7-8 wpf curved or straight fish of the same clutch. The RF was visualized
207 as a 1 µm diameter rod in the central canal of the neural tube and few dots were
208 present in the apical cytoplasm of FP cells (Figure 3I) as well as in the SCO of all
209 controls (n=8, Figure 3L, O) and in ventricles caudal to the SCO, but not rostral to it as
210 expected (Supplementary Figure S2E, H). The RF was also present in all *rpgrip1l*$^{-/-}$
211 straight fish (n=9, Figure 3J, Supplementary Figure S2I). In contrast, in *rpgrip1l*$^{-/-}$ tail-
212 up and scoliotic fish, the RF was absent at all axis levels and a few SCO-spondin-
213 positive debris were present in the central canal (n=8, Figure 3K). Transverse sections
214 at the level of the SCO and fChP as well as caudal to the SCO in severely scoliotic fish
215 revealed abnormally packed material in the ventricles (Figure 3N, Q, Supplementary
216 Figure S2G, J). In juveniles with a slight tail-up phenotype, SCO-secreting cells
217 produced Sspo-GFP cytoplasmic granules as in controls (Supplementary Figure S2B,
218 B', n=7/7), and polymers of Sspo-GFP accumulate in the adjacent DiV, which suggests
219 that Sspo-GFP aggregates are produced by the SCO.
220 Thus, our study uncovers a strict temporal correlation between the loss of MCC at
221 posterior SCO level, impaired RF polymerization and scoliosis onset in *rpgrip1l*$^{-/-}$
222 juvenile fish.
223
224 ***Urp1/2 upregulation does not contribute to scoliosis penetrance or severity in***
225 ***rpgrip1l*$^{-/-}$ *fish***
226
227 In scoliotic fish where the RF is not maintained at juvenile stage, *urp1* and *urp2* levels
228 are downregulated (Rose et al., 2020). *urp1* and *urp2* encode peptides of the Urotensin
229 2 family, expressed in ventral spinal CSF-cNs (Parmentier et al., 2011; Quan et al.,
230 2015). Their expression levels have to be finely tuned to keep a straight axis since their

231 combined loss-of-function induces larval kyphosis that evolves into adult scoliosis
232 (Bearce et al., 2022; Gaillard et al., 2023), while an increased dose of Urp1/2 peptides
233 induces an upward curvature in embryos (Zhang et al., 2018) and juveniles (Gaillard
234 et al., 2023; Lu et al., 2020). We therefore monitored via qRT-PCR *urp1 and urp2*
235 expression levels on individual straight or scoliotic *rpgrip1l*$^{-/-}$ juvenile and/or adult fish.
236 *urp2* was the most highly expressed gene among all *urotensin 2* members at juvenile
237 stage (Figure 4A, D, E and Supplementary Figure S3A-E. *urp2* expression was
238 upregulated in 5 weeks juveniles, both in straight and scoliotic fish and its upregulation
239 was maintained in adult scoliotic fish (Figure 4A).
240 Given the early and long-lasting upregulation of *urp1/2* in *rpgrip1l*$^{-/-}$ fish, we attempted
241 to rescue axis curvature by decreasing global Urp1/2 production via genetic means.
242 To that end, we generated double (*rpgrip1l*$^{+/-}$*; urp2*$^{+/-}$) heterozygous fish using the
243 recently generated *urp2* deletion allele (Gaillard et al., 2023) and crossed them to
244 produce double mutants. Using a curvature quantification method on whole fish
245 (Supplementary Figure S3I and methods), we observed that the removal of one or two
246 *urp2* functional allele(s) in *rpgrip1l*$^{-/-}$ fish did not lower their curvature index (Figure 4B,
247 C), neither at two mpf (Supplementary Figure S3 F) nor at four mpf (Supplementary
248 Figure S3 G-H). We observed that *urp2* mRNA amounts were reduced by removing
249 one or two functional copies of *urp2*, probably as a consequence of mRNA decay
250 (Gaillard et al., 2023) (Figure 4D). We also showed that none of the other *urotensin 2*
251 family members was upregulated by a compensation mechanism upon *urp2* loss
252 (Figure 4E for *urp1* and Supplementary Figure S3C-E for *urp, uts2a* and *uts2b*).
253 Thus, lowering global Urp1/2 expression level in *rpgrip1l* mutants did not have any
254 beneficial effect on the axis curvature phenotype, ruling out altered *urp1/2* signaling as
255 a main driver of scoliosis in *rpgrip1l* mutants.
256
257 ***Regulators of motile ciliogenesis, inflammation genes and annexins are***
258 ***upregulated in rpgrip1l*$^{-/-}$ *juveniles***
259
260 To get further insight into the early mechanisms driving spine curvature in *rpgrip1l*
261 mutants, we obtained the transcriptome of the brain and dorsal trunk of 7 *rpgrip1l*$^{-/-}$
262 juveniles at scoliosis onset (6 tail-up and 1 straight 5 wpf juveniles) and 5 control
263 siblings (2 *rgprip1l*$^{+/+}$ and 3 *rgprip1l*$^{+/-}$). Differential gene expression (DGE) analysis

264 was performed with the DSEQ2 software within the Galaxy environment. A complete
265 annotated gene list is displayed in Supplementary Table 1 (Trunk) and Table 2 (Brain).
266 Filtering the gene list to select for P-adj < 0.05 and Log2 FC > 0.75 or < -0.75 recovered
267 a vast majority of upregulated genes in the dorsal trunk (75 downregulated vs 614
268 upregulated genes) and, to a lesser extent, in the brain (1 downregulated, *rpgrip1l,* vs
269 60 upregulated genes) as illustrated on the volcano plots from DGE analysis of the
270 brain (Figure 5A) and trunk (Figure 5B). 54 out of 60 genes upregulated in the brain
271 were also upregulated in the trunk, suggesting that, in the trunk, these genes were
272 specific to the CNS (Figure 5D). In both the brain (Figure 5C) and the trunk
273 (Supplementary Figure S4A), the most upregulated biological processes in GO term
274 analysis included cilium movement and cilium assembly. Among the 20 most
275 significant GO terms found for upregulated genes in the trunk, 8 were related to ciliary
276 movement/assembly (Supplementary Figure S4A). The upregulation in both tissues of
277 *foxj1a,* encoding a master transcriptional activator of genes involved in cilia motility (Yu
278 et al., 2008) (Figure 5E) likely contributed to this enrichment. To confirm this
279 hypothesis, we compared our dataset with those of targets of Foxj1 from (Choksi et al.,
280 2014; Mukherjee et al., 2019; Quigley and Kintner, 2017). We found that 106 out of
281 614 upregulated genes were targets of Foxj1, among which 77 were direct targets
282 (Supplementary Table 3). Several genes encoding regulators of embryonic axis
283 curvature were also upregulated in *rpgrip1l*$^{-/-}$ fish, among which *pkd1b* (Mangos et al.,
284 2010), *urp1* and *urp2* (Bearce et al., 2022; Gaillard et al., 2023; Zhang et al., 2018)
285 and *sspo* (Cantaut-Belarif et al., 2018; Rose et al., 2020; Troutwine et al., 2020) (Figure
286 5E). Finally, GO terms enrichment analysis also highlighted processes associated with
287 inflammation and innate and adaptive immune responses, as described for the scoliotic
288 *ptk7* model (Van Gennip et al., 2018) sharing for example *irg1l* and complement genes
289 up-regulation (Figure 5 C, E, and Supplementary Figure S4A).
290 In order to confirm these results and to identify processes affected at the post-
291 transcriptional level in *rpgrip1l* mutants, we performed a quantitative proteomic
292 analysis by mass spectrometry of brains from 5 *rpgrip1l*$^{-/-}$ adult fish and 5 control
293 siblings. This analysis detected 5706 proteins present in at least 4 over the 5 replicates,
294 of which 172 are associated with a P value < 0.05 and a Log2FC > +0.75 and < -0.75.
295 127 proteins were present in higher and 45 in lower quantity, as illustrated on the
296 volcano plot (Figure 5F and Supplementary Table 4). Pathways enriched in *rpgrip1l*$^{-/-}$

297 brains included regulation of vesicular trafficking and membrane repair processes, as
298 well as proteolysis and catabolic processes, suggesting profound perturbation of
299 cellular homeostasis (Supplementary Figure S4B). Among the proteins that were
300 present in highest quantity in mutants, several members of the Annexin family were
301 identified: Anxa2a, Anxa1a, Anxa5b (Figure 5F and Supplementary Figure S4C.
302 Annexins are associated with membranes from endo and exovesicles as well as
303 plasma membranes and involved in a wide array of intracellular trafficking processes
304 such as cholesterol endocytosis, plasma membrane repair as well as modulation of
305 immune system functions (Boye and Nylandsted, 2016; Grewal et al., 2016; Rentero
306 et al., 2018). Of note, only four proteins of that list, Anxa2a, C4, C7a and Stat3, were
307 the products of genes up-regulated in the transcriptomic study (indicated in red in
308 Figure 5E). In agreement with the common enriched GO terms in both studies (Figure
309 5C and Supplementary Figure S4B), these four proteins are associated with immune
310 response. Overall, *rpgrip1l*$^{-/-}$ mutants at scoliosis onset present deregulated pathways
311 in common with other scoliotic models such as activation of immune response genes,
312 but also specific deregulated pathways such a marked activation of the Foxj1a ciliary
313 motility program and an increase of Annexin levels.
314
315 ***Astrogliosis precedes scoliosis onset of rpgrip1l*$^{-/-}$ *juvenile fish***
316
317 Both transcriptomic and proteomic analysis highlighted the occurrence of innate and
318 adaptive immune responses in *rpgrip1l*$^{-/-}$ fish. Several upregulated genes, such as
319 *irg1l, mmp9 and anxa2,* are reported to be expressed in macrophages and/or microglia
320 but also in epithelia or neurons (Hall et al., 2014) (Kuhlmann et al., 2014) (Shan et al.,
321 2015). We therefore investigated in which cell type(s) Anxa2, the most upregulated
322 protein in the *rpgrip1l*$^{-/-}$ brain proteome, was expressed. Immunostaining of brain
323 sections revealed a strong Anxa2 staining on cells lining brain ventricles, such as SCO
324 cells and ventral ependymal cells of the rhombencephalic ventricle (RhV) (Fig 6B', D')
325 in *rpgrip1l*$^{-/-}$ adult fish, which was barely detectable in controls (Figure 6A', C'), and to
326 a lesser extent on other brain regions (Supplementary Fig S5 A'-F'), suggesting a
327 deregulation of ependymal cell homeostasis. In mutants, Anxa2 staining spread over
328 long cellular extensions reaching the pial surface of the rhombencephalon (Figure 6D'
329 and Supplementary Figure S5F'). This cell shape is characteristic of radial glial cells,

330 a cell type that behaves as neural and glial progenitors and also plays astrocytic
331 functions in zebrafish, as anamniote brains are devoid of stellate astrocytes (Jurisch-
332 Yaksi et al., 2020; Lyons and Talbot, 2015). To confirm the glial nature of Anxa2-
333 positive cells around brain ventricles in *rpgrip1l*$^{-/-}$ fish, we double-labeled brain sections
334 with GFAP, a glial cell marker, and Anxa2. In adult *rpgrip1l*$^{-/-}$ fish, SCO cells were
335 strongly double-positive for Anxa2 and GFAP (Fig 6B, B'), while controls displayed
336 much weaker labeling for GFAP in the SCO and no labeling for Anxa2 (Fig 6 A, A').
337 We made similar observations at rhombencephalic ventricle (RhV) and other brain
338 levels: ependymal cells were positive for Anxa2 and strongly positive for GFAP, and
339 GFAP labeling was much higher in mutants than in controls (Fig 6 C-D'; supplementary
340 Figure S5A-F'). GFAP overexpression is a hallmark of astrogliosis, a process in which
341 astroglial cells react to the perturbed environment, as shown during brain infection,
342 injury, ischemia or neurodegeneration (Escartin et al., 2021; Matusova et al., 2023;
343 Zamanian et al., 2012). Thus, the strong increase of GFAP staining combined with
344 Anxa2 overexpression in brain ependymal cells of *rpgrip1*$^{l-/-}$ adult fish strongly suggests
345 that these cells undergo astrogliosis as observed in other animal models following CNS
346 injury (Chen et al., 2017; Zamanian et al., 2012).
347 To assay whether an astrogliosis-like phenotype was already present at scoliotic onset,
348 we immunostained GFAP on juvenile brain sections of straight and tail-up mutants and
349 controls. Tail-up juveniles (n=3/3) presented a strong GFAP staining in almost all cells
350 of the SCO and along the ventral rhombencephalic ventricle, higher than control levels
351 (Figure 6 E, I, H, L, M) while the phenotype of straight fish was heterogeneous: two out
352 of four juveniles presented GFAP-positive cells (Figure 6G, K and red dots on Figure
353 6M graph), while the two other did not (Figure 6F, J and green dots on Figure 6M
354 graph) as confirmed by cell quantification (Figure 6M). As scoliosis onset is
355 asynchronous in *rpgrip1l*$^{-/-}$, heterogenous GFAP staining among straight mutant fish
356 may support an early role of astrogliosis at SCO and RhV levels in scoliosis onset.
357
358 ***Immune cell enrichment around the SCO and within tectum parenchyma is***
359 ***detected prior to scoliosis onset.***
360
361 Astrogliosis may be reinforced or induced by an inflammatory environment containing
362 cytokines released by microglia or macrophages or the presence of high levels of ROS

363 and NO (Sofroniew, 2015). We thus performed immunostaining for the LCP1/L-Plastin
364 marker, which labels both macrophages and microglia (Figure 6N-Q'), in adjacent
365 sections to those used for GFAP (Figure 6E-L). We found that the scoliotic fish
366 presented a higher number of LCP1-positive cells of ameboid shape within SCO cells
367 (Figure 6Q, Q', R). Strikingly, the straight mutants (2/4) that presented a high GFAP
368 staining within SCO cells (Figure 6G, K) also showed a higher number of LCP1-positive
369 cells around the SCO (Figure 6P, P'; red dots in Figure 6R) than in controls (Figure
370 6N, N'), while the other straight mutants did not ((Figure 6F, J, O, O', green dots in
371 Figure 6M) suggesting positive regulation between astrogliosis and
372 macrophages/microglia recruitment. LCP1+ cells were also detected in other regions
373 of the brain (Supplementary Figure S5 G-K). In the optic tectum, where resident LCP1-
374 positive macrophages/microglia were present in controls, a two-fold increase in the
375 number of ramified LCP1^{+} cells was observed in straight *rpgrip1l*$^{-/-}$ juveniles compared
376 to controls (Supplementary Figure S5H-J). Surprisingly, scoliotic *rpgrip1l*$^{-/-}$ fish showed
377 similar LCP1^{+} cell number as control fish in the tectum (Supplementary Figure S5G),
378 suggesting a transient increase of macrophage/microglia activation preceding
379 scoliosis.
380 Our data thus uncovers an early astrogliosis process initiated asynchronously at the
381 SCO and RhV levels of straight *rpgrip1l*$^{-/-}$ fish, favored by a transient inflammatory
382 state, and preceding the loss of multiciliated tufts around the SCO and that of the RF,
383 that we only detected in curved *rpgrip1l*$^{-/-}$ fish. Astrogliosis then spreads along the brain
384 ventricles and becomes prominent in brain of scoliotic fish. In addition, we found among
385 the upregulated genes in dorsal trunk at scoliosis onset, a number of activated
386 astrocyte markers (Matusova et al., 2023) such as *s100b*, *c4b*, *gfap*, *glast/slc1a3b*,
387 *viml*, *ctsb* (Supplementary Figure S4D), showing that astrogliosis spread over the
388 whole central nervous system.
389
390 ***Brain neuroinflammation and astrogliosis contribute to scoliosis penetrance***
391 ***and severity in rpgrip1l$^{-/-}$ fish***
392
393 Our data suggest that astrogliosis and neuro-inflammation could play a role in
394 triggering scoliosis in *rpgrip1l* mutants. We thus aimed to counteract inflammation
395 before curvature initiation by performing drug treatment with the hope of reducing

396 scoliosis penetrance and severity. We used the NACET anti-oxidant and anti-
397 inflammatory drug that successfully reduced scoliosis of *sspo* hypomorphic mutant fish
398 (Rose et al., 2020). We first assayed the biological activity of our NACET batch on the
399 ciliary motility mutant *dnaaf1*$^{-/-}$ (Sullivan-Brown et al., 2008). Indeed, NACET was
400 shown to suppress the embryonic tail-down phenotype of the ciliary motility mutant
401 *ccdc151*^{ts} (Rose et al., 2020). We found that 3mM NACET treatment suppressed the
402 *dnaaf1*$^{-/-}$ tail-down phenotype (Supplementary Figure S6A-F). To suppress scoliosis,
403 we treated the progeny of *rpgrip1l*$^{+/-}$ incrosses from 4 to 12 wpf with 1.5 mM NACET
404 as in (Rose et al., 2020).This long-term treatment reduced scoliosis penetrance from
405 92% to 58% and markedly reduced spinal curvature index (Figure 7A-C), measured
406 and illustrated as shown in Supplementary Figure S3I.
407 We then asked whether NACET treatment suppressed astrogliosis and
408 neuroinflammation in *rpgrip1l*$^{-/-}$ treated fish. Indeed, the intensity and number of
409 GFAP+ cells within the SCO were reduced in slightly curved fish and alleviated in
410 straight fish (Figure 7E, F). Furthermore, the quantification of Lcp1-positive cells in the
411 SCO region showed a drastic reduction of these cells in NACET-treated fish, back to
412 levels found in *rpgrip1l*$^{+/+}$ fish (Figure 7D, E).
413 Our data thus show that *rpgrip1l*$^{-/-}$ juvenile fish display brain astrogliosis and
414 inflammation at scoliosis onset and that an anti-inflammatory/anti-oxidant treatment of
415 *rpgrip1l*$^{-/-}$ juveniles is able to maintain a straight axis in approximately one third of the
416 mutants and to slow down curve progression in the other two thirds. The beneficial
417 effect of NACET on axis curvature correlates with the combined reduction of
418 astrogliosis and immune cell density.
419
420 **Brain astrogliosis is present in zebrafish *cep290* $^{fh297/fh297}$ scoliotic fish**
421
422 To investigate whether abnormal SCO cilia function and brain astrogliosis may be a
423 general mechanism of scoliosis development in TZ mutants, we studied the
424 *cep290*$^{fh297/fh297}$ zebrafish mutant. Zebrafish *cep290* mutants display variable axis
425 curvature defects at embryonic stages as well as slow retinal degeneration, and
426 develop juvenile scoliosis (Lessieur et al., 2019; Wang et al., 2022). Like *RPGRIP1L*,
427 the human *CEP290* gene encodes a TZ protein and its mutation leads to severe
428 neurodevelopmental ciliopathies (Baala et al., 2007). All *cep290*$^{fh297/fh297}$ juveniles

429 developed a fully penetrant scoliosis by 4 wpf in our fish facility (n: 30/30). We analyzed
430 cilia presence within the SCO by immunostaining on sections (Figure 8A-F'). At 4 wpf,
431 the SCO had not reached its final adult width (14 versus 24 cells wide in the anterior
432 SCO), and each of its cells harbored a short monocilium labeled by glutamylated
433 tubulin (Figure 8A-C). Multicilia tufts on SCO lateral walls were not as clearly visible as
434 in adults (Figure 2F) but patches of glutamylated tubulin staining were detected on
435 both sides of the posterior SCO (Figure 8B-C'). In *cep290*$^{-/-}$, monocilia of the SCO
436 appeared longer than in controls (N=3/3) and pointed towards an abnormally elongated
437 diencephalic ventricle (Figure 8D-F). Lateral patches of glutamylated tubulin staining
438 were present in *cep290*$^{-/-}$ posterior SCO as in controls (Figure 8E-F'). Thus, cilia
439 morphology is perturbed within *cep290*$^{-/-}$ SCO monociliated cells, as well as the overall
440 morphology of the diencephalic ventricle at this level.
441 To test for the presence of astrogliosis, we quantified the number of SCO cells
442 presenting high GFAP labeling on several sections along the A/P extent of the SCO in
443 3 control and 3 *cep290*$^{-/-}$ brains (Figure 8G-K). 50% of SCO cells presented strong
444 GFAP staining in fully scoliotic juveniles, which was not detectable in controls (Figure
445 8H, K, N=2/3), while a lower proportion (22%) of SCO cells was GFAP positive in the
446 juvenile with a milder curvature (Figure 8M, N=1/3). Strong GFAP staining was also
447 detected in some diencephalic radial glial cells (Figure 8K). On the same sections,
448 immune cells were quantified by LCP1 staining. A mean of 4 LCP1 positive cells per
449 SCO field was found in *cep290*$^{-/-}$, versus 1 in controls (Figure 8I, L and N). As in *rpgrip1l*
450 mutants, abnormal monocilia, astrogliosis and immune cell enrichment were evidenced
451 at SCO levels in *Cep290* $^{-/-}$(3/3). Furthermore, astrogliosis was observed within radial
452 glial cells lining the RhV at cerebellar level (Figure 8O-R) and at anterior hindbrain level
453 (Figure 8S-V), as shown in *rpgrip1l*$^{-/-}$ scoliotic brain (Figure 6D, K, L). This indicates
454 that astrogliosis is shared by these two zebrafish scoliotic models, even though they
455 develop axis curvature at different stages (3-4 wpf for *cep290*$^{-/-}$ versus 5-12 wpf for
456 *rpgrip1l*$^{-/-}$).
457
458 **DISCUSSION**
459
460 In this paper we dissected the mechanisms of scoliosis appearance in a zebrafish
461 mutant for the TZ gene *rpgrip1l*, taking advantage of its asynchronous onset to

462 decipher the chronology of events leading to spine torsion. Transcriptome analysis of
463 the brain and trunk at scoliosis onset in *rpgrip1l*$^{-/-}$ fish compared to control siblings
464 revealed increased expression of *urp1/2*, *foxj1a* and its target genes, as well as genes
465 linked to immune response. Genetic experiments ruled out an involvement of
466 increased Urp1/2 signaling in scoliosis development. Cilia defects appeared
467 asynchronously in different CNS regions, while RF loss strictly coincided with scoliosis
468 onset. Strikingly, we observed a strong increase of GFAP staining along the
469 diencephalic and rhombencephalic ventricles, indicative of astrogliosis. This
470 astrogliosis preceded scoliosis onset and then spread posteriorly and increased in
471 severity. In the region of the SCO, the appearance of astrogliosis and
472 neuroinflammation coincided temporally, preceding the onset of RF depolymerization
473 and spine torsion. NACET treatment showed that increased astrogliosis and
474 inflammation participated in the penetrance and severity of scoliosis in *rpgrip1l*$^{-/-}$ fish.
475 Finally, we showed that another TZ gene mutant, *cep290*, also displayed astrogliosis
476 at the time of scoliosis onset. Thus, the cascade of events uncovered in the *rpgrip1l*
477 mutant sheds a new light on the origin of zebrafish scoliosis caused by ciliary TZ
478 defects.
479
480 Cilia motility defects lead to RF loss and to scoliosis in several zebrafish mutants
481 (Grimes et al., 2016; Rose et al., 2020)). *Rpgrip1l* encodes a TZ protein important for
482 cilia integrity and function in many eukaryotic organisms (Andreu-Cervera et al., 2019;
483 Gogendeau et al., 2020; Jensen et al., 2015; Wiegering et al., 2018). Our data show
484 that *rpgrip1l* deficiency in zebrafish affects cilia maintenance differentially depending
485 on the CNS territory and the developmental stage, raising the question of which ciliated
486 cells are responsible for RF loss and scoliosis initiation in this mutant. The full rescue
487 observed after re-introducing RPGRIP1L in *foxj1a*-expressing cells points towards a
488 crucial function of the protein in cells lining CNS cavities. Foxj1a-positive cell
489 populations encompass both monociliated and multiciliated ependymal cells, radial
490 glial progenitors, glial cells of the SCO and the ChP, as well as CSF-contacting sensory
491 neurons in the spinal cord (D'Gama et al., 2021; Prendergast et al., 2023; Ribeiro et
492 al., 2017; Van Gennip et al., 2018). Recent work suggested that impairment of
493 ciliogenesis in the fChP of the *katnb1* mutant could play a role in inducing axis
494 curvature (Meyer-Miner et al., 2022). In the case of the *rpgrip1l* mutant, we temporally

495 uncorrelated fChP cilia defects from scoliosis onset. This, combined with the fact that
496 the total loss of multicilia in the fChP of [*foxj1b*$^{-/-}$, *gmnc*$^{-/-}$] double mutants does not
497 trigger axis curvature (D'Gama et al., 2021) suggests that another *foxj1a*-expressing
498 population is crucial for axis straightness. Our results strongly suggest that cilia defects
499 in the SCO trigger axis curvature in *rpgrip1l* mutants. Two cilia populations were
500 affected in the SCO of *rpgrip1l* mutant juveniles at the onset of scoliosis: cilia of
501 monociliated glial cells that secrete SCO-spondin, which appeared longer in mutants
502 than in controls, and multiciliated tufts at SCO exit, which were lost in scoliotic mutants.
503 Both defects could be responsible for the phenotype, by perturbing CSF flow and
504 content (presence of SCO-spondin aggregates in ventricles) (left side on the Graphical
505 Abstract) and leading to ventricular dilations or by perturbing primary cilia signaling
506 within SCO cells (right side of the Graphical Abstract). The observation that
507 multiciliated cells were not yet fully differentiated in *cep290* mutants at scoliosis onset
508 is in favor of a prominent role of monocilia. This is consistent with the literature showing
509 that most ciliary mutant models develop axis curvature at 3-4 weeks, a stage when
510 brain multiciliated cells are not yet differentiated (D'Gama et al., 2021). Still, as
511 scoliosis onset in *rpgrip1l* mutant is asynchronous from 5 to 12 weeks, MCC loss at
512 SCO exit could contribute to defective RF polymerization.
513
514 Our model for scoliosis appearance in the *rpgrip1l* mutant is presented in the graphical
515 abstract. Since we have observed several straight *rpgrip1l*$^{-/-}$ fish with astrogliosis and
516 increased immune cells presence around the SCO, we propose that *rpgrip1l*$^{-/-}$ SCO
517 and astroglial cells experience altered signaling that activates immune cell recruitment,
518 producing an inflammatory environment. This would promote multicilia loss as a
519 secondary event (Graphical Abstract, orange arrow) (Lattke et al., 2012) leading to RF
520 depolymerization and spine curvature. However, as *sspo* $^{-/-}$ hypomorphic mutants
521 which present aggregates within ventricles have been shown to present an
522 inflammatory response (Rose et al., 2020), it is equally possible that SCO astrogliosis
523 is a downstream consequence of the presence of these proteoglycans aggregates in
524 contact with primary cilia or ventricular cell surfaces (Graphical Abstract , green arrow).
525 These two scenarios may also act in parallel to reinforce scoliosis onset and
526 ependymal cilia loss. Future experiments will help to discriminate between these two
527 scenarios.

528

529 Our transcriptome analysis and qRT-PCR data challenges a model proposed for axis
530 straightness of zebrafish embryos in which the loss of RF leads to a down-regulation
531 of *urp2* and *urp1* expression (Zhang et al., 2018) since we observed an upregulation
532 of both genes before and after RF loss. As forced expression of *urp1/2* induces a tail-
533 up phenotype in embryos and juveniles (Zhang et al., 2018) (Gaillard et al., 2023; Lu
534 et al., 2020), we attempted to rescue *rpgrip1l*$^{-/-}$ axis curvature by down-regulating
535 *urp1/2* expression. No beneficial effect on scoliosis penetrance or severity was
536 observed, indicating that increased *urp1/2* expression level does not significantly
537 contribute to axis curvature in *rpgrip1l*$^{-/-}$ fish.

538

539 In this study, we found an unexpected and strong defect characterized by enhanced
540 GFAP and Anxa2 expression, which we identified as astrogliosis (also called reactive
541 astrogliosis). Astrogliosis is a reaction of astroglial cells to perturbed homeostasis of
542 the CNS, characterized by molecular and phenotypic changes in these cells (Escartin
543 et al., 2021; Matusova et al., 2023). In zebrafish, radial glial cells are endowed with
544 both neurogenic and astrocytic functions, and are thus also called astroglial cells
545 (Jurisch-Yaksi et al., 2020). Astrogliosis in *rpgrip1l* mutants arose in a subdomain of
546 Foxj1a-positive cells, within the DiV and ventral ependymal cells lining the RhV. The
547 observation of astrogliosis in some straight juvenile mutants suggests an early role of
548 this defect in scoliosis onset.

549 Astrogliosis along the ventricular cavities could arise in response to local mechanical
550 or chemical perturbations caused by cilia motility defects, abnormal CSF flow and
551 content and ventricular dilations. In two murine models of primary ciliary dyskinesia,
552 decreased CSF flow was associated with gliosis at juvenile stage (Finn et al., 2014). A
553 response to CSF pertubation in *rpgrip1l* mutants is also suggested by the strong
554 upregulation of Foxj1a and its target genes. *foxj1a* expression is also reported to be
555 upregulated in the CNS of three other scoliotic models in addition to *rpgrip1l*, namely
556 in *ptk7, sspo* and *katnb1* mutants (Escartin et al., 2021; Meyer-Miner et al., 2022; Van
557 Gennip et al., 2018), suggesting that it constitutes a common response to similar
558 ventricular and CSF defects. Interestingly, *foxj1a* expression is also upregulated upon
559 zebrafish embryonic (Cavone et al., 2021; Hellman et al., 2010) or adult (Ribeiro et al.,
560 2017) spinal cord injury. The up-regulation in the *rpgrip1l* mutant proteome of the

561 membrane repair module Anxa2-S100a10-Ahnak (Bharadwaj et al., 2021) (Figure 4C)
562 together with the Foxj1-induced motility module detected in the transcriptomic analysis
563 may indicate ongoing reparation attempts of CNS ventricles and associated neural
564 tissues.

565 Moreover, the presence of few Lcp1+ cells around the mutant SCO suggests that
566 microglia/macrophages could participate in astrogliosis establishment and
567 reinforcement. This dialogue between immune Lcp1+ cells and astroglial cells is
568 evidenced during early stages of regeneration after acute injury or cellular damages
569 (Cavone et al., 2021). In our bulk RNAseq analysis performed at scoliosis onset, we
570 have indications of the upregulation of microglia and macrophage markers (*p2ry12* and
571 *mpeg1*) at trunk levels and of numerous markers of activated astrocytes characterized
572 in several mammalian astrogliosis models (Matusova et al., 2023). A similar dialogue
573 is detected in polycystic kidney disease models where compromised primary cilia
574 signalling leads to uncontrolled cytokines secretion by epithelial cells, a situation that
575 favors local immune cells recruitment and proliferation (Viau et al., 2018).

576 What are the intracellular mechanisms involved in astrogliosis induction in ciliated
577 ventricular cells? Candidate pathways emerge from our multi-omics studies. Proteomic
578 data showed a 2.4-fold increase in GSK3bb amount in *rpgrip1l*$^{-/-}$ mutant brains (P value
579 < 0.001, Supplementary Table 3). In several neurodegenerative murine animal models,
580 GSK3b enzymatic activity was shown to promote inflammation and gliosis (Jorge-
581 Torres et al., 2018; Medina and Avila, 2010; Mines et al., 2011). Another potential
582 trigger of astrogliosis may be a defective mitochondrial activity as the amounts of four
583 proteins involved in electron transport chain activity (*gpd1b, mt-nd6, pdia5 and dmgdh*)
584 were reduced by 40% to 86% in the analysis of mutant brain proteome (Supplementary
585 Table 4). We think this is of particular interest in light of a recent report demonstrating
586 that impaired mitochondrial activity within ciliated astrocytes leads to the induction of
587 the Foxj1 ciliary motility program, the elongation and distortion of astrocyte primary
588 cilia as well as reactive astrogliosis (Ignatenko et al., 2023), three phenotypes also
589 observed in *rpgrip1l*$^{-/-}$ brains.
590

591 Finally, our observation of widespread astrogliosis in two TZ gene mutants, *rpgrip1l*
592 and *cep290*, suggests that it could represent a general mechanism involved in scoliosis
593 downstream of cilia dysfunction. Of note, astrogliosis markers such as *glast/slc1a3b*,

vim, *s100b*, *c4*, *timp2b*, *gfap* and *ctssb.2*, are also upregulated in the transcriptome of *ptk7 mutants* (Van Gennip et al., 2018). We propose that sustained astrogliosis might impair neuronal survival and activity, crucial for proper interoception and locomotor control, thus leading to axis curvature in the context of a rapidly growing axial skeleton. A similar context of astrocytosis associated with spinal cord dilation has been observed in human patients with syringomyelia. This population with a high incidence of scoliosis can present hyper-signals on T2 MRI scans, which were proposed to reflect local astrocytosis and could be validated by biopsies in rare cases (Sherman et al., 1987). Further imaging studies will need to be performed to validate a potential link between developing astrogliosis and the onset and progression of idiopathic scoliosis in humans.

ACKNOWLEDGEMENTS

We are grateful to the IBPS aquatic animal, imaging and bioinformatics facilities and to the ICM sequencing facility for their technical assistance. We thank Michaël Trichet from the IBPS electron microscopy facility for participating in the MEB experiments, the TACGENE facility for providing the Cas9 protein; the TEFOR Paris-Saclay facility for the brain clearing experiment; Thierry Jaffredo and Pierre Charbord for their precious help in transcriptome analysis; Nicolas Baylé for initial characterization of the *rpgrip1l* mutant; Claudia Hoffman for providing *Cep290* fixed samples; Brian Ciruna for sharing the *foxj1a* expressing constructs and detailed NACET treatment protocol; Ryan Gray for sharing the *scospondin-GFP*^{ut24} zebrafish line. This work was supported by funding to SSM from the Fondation pour la Recherche Médicale (Equipe FRM EQU201903007943) and the Fondation Yves Cotrel.

620 **REFERENCES**

621 Affaticati P, Simion M, De Job E, Rivière L, Hermel J-M, Machado E, Joly J-S, Jenett A. 2017.
622 zPACT: Tissue Clearing and Immunohistochemistry on Juvenile Zebrafish Brain. *BIO-*
623 *PROTOCOL* **7**. doi:10.21769/BioProtoc.2636

624 Andreu-Cervera A, Anselme I, Karam A, Laclef C, Catala M, Schneider-Maunoury S. 2019.
625 The ciliopathy gene *ftm/rpgrip1l* controls mouse forebrain patterning via region-specific
626 modulation of hedgehog/gli signaling. *J Neurosci* 2199–18. doi:10.1523/JNEUROSCI.2199-
627 18.2019

628 Andreu-Cervera A, Catala M, Schneider-Maunoury S. 2021. Cilia, ciliopathies and hedgehog-
629 related forebrain developmental disorders. *Neurobiology of Disease* **150**:105236.
630 doi:10.1016/j.nbd.2020.105236

631 Arts HH, Doherty D, Van Beersum SEC, Parisi MA, Letteboer SJF, Gorden NT, Peters TA,
632 Märker T, Voesenek K, Kartono A, Ozyurek H, Farin FM, Kroes HY, Wolfrum U, Brunner
633 HG, Cremers FPM, Glass IA, Knoers NVAM, Roepman R. 2007. Mutations in the gene
634 encoding the basal body protein RPGRIP1L, a nephrocystin-4 interactor, cause Joubert
635 syndrome. *Nat Genet* **39**:882–888. doi:10.1038/ng2069

636 Baala L, Audollent S, Martinovic J, Ozilou C, Babron M-C, Sivanandamoorthy S, Saunier S,
637 Salomon R, Gonzales M, Rattenberry E, Esculpavit C, Toutain A, Moraine C, Parent P,
638 Marcorelles P, Dauge M-C, Roume J, Merrer ML, Meiner V, Meir K, Menez F, Beaufrère A-
639 M, Francannet C, Tantau J, Sinico M, Dumez Y, MacDonald F, Munnich A, Lyonnet S, Gubler
640 M-C, Génin E, Johnson CA, Vekemans M, Encha-Razavi F, Attié-Bitach T. 2007. Pleiotropic
641 Effects of CEP290 (NPHP6) Mutations Extend to Meckel Syndrome. *The American Journal of*
642 *Human Genetics* **81**:170–179. doi:10.1086/519494

643 Bachmann-Gagescu R, Phelps IG, Stearns G, Link BA, Brockerhoff SE, Moens CB, Doherty
644 D. 2011. The ciliopathy gene cc2d2a controls zebrafish photoreceptor outer segment
645 development through a role in Rab8-dependent vesicle trafficking. *Human Molecular Genetics*
646 **20**:4041–4055. doi:10.1093/hmg/ddr332

647 Bearce EA, Irons ZH, O'Hara-Smith JR, Kuhns CJ, Fisher SI, Crow WE, Grimes DT. 2022.
648 Urotensin II-related peptides, Urp1 and Urp2, control zebrafish spine morphology. *eLife*
649 **11**:e83883. doi:10.7554/eLife.83883

650 Bentley-Ford MR, LaBonty M, Thomas HR, Haycraft CJ, Scott M, LaFayette C, Croyle MJ,
651 Andersen RS, Parant JM, Yoder BK. 2022. Evolutionarily conserved genetic interactions
652 between *nphp-4* and *bbs-5* mutations exacerbate ciliopathy phenotypes. *Genetics* **220**:iyab209.

653 doi:10.1093/genetics/iyab209
654 Bharadwaj A, Kempster E, Waisman DM. 2021. The Annexin A2/S100A10 Complex: The
655 Mutualistic Symbiosis of Two Distinct Proteins. *Biomolecules* **11**:1849.
656 doi:10.3390/biom11121849
657 Boswell CW, Ciruna B. 2017. Understanding Idiopathic Scoliosis: A New Zebrafish School of
658 Thought. *Trends in Genetics* **33**:183–196. doi:10.1016/j.tig.2017.01.001
659 Bouyssié D, Hesse A-M, Mouton-Barbosa E, Rompais M, Macron C, Carapito C, Gonzalez De
660 Peredo A, Couté Y, Dupierris V, Burel A, Menetrey J-P, Kalaitzakis A, Poisat J, Romdhani A,
661 Burlet-Schiltz O, Cianférani S, Garin J, Bruley C. 2020. Proline: an efficient and user-friendly
662 software suite for large-scale proteomics. *Bioinformatics* **36**:3148–3155.
663 doi:10.1093/bioinformatics/btaa118
664 Boye TL, Nylandsted J. 2016. Annexins in plasma membrane repair. *Biological Chemistry*
665 **397**:961–969. doi:10.1515/hsz-2016-0171
666 Brancati F, Travaglini L, Zablocka D, Boltshauser E, Accorsi P, Montagna G, Silhavy JL,
667 Barrano G, Bertini E, Emma F, Rigoli L, International JSRD Study Group, Dallapiccola B,
668 Gleeson JG, Valente EM. 2008. RPGRIP1L mutations are mainly associated with the cerebello-
669 renal phenotype of Joubert syndrome-related disorders. *Clin Genet* **74**:164–170.
670 doi:10.1111/j.1399-0004.2008.01047.x
671 Cantaut-Belarif Y, Orts Del'Immagine A, Penru M, Pézeron G, Wyart C, Bardet P-L. 2020.
672 Adrenergic activation modulates the signal from the Reissner fiber to cerebrospinal fluid-
673 contacting neurons during development. *eLife* **9**:e59469. doi:10.7554/eLife.59469
674 Cantaut-Belarif Y, Sternberg JR, Thouvenin O, Wyart C, Bardet P-L. 2018. The Reissner Fiber
675 in the Cerebrospinal Fluid Controls Morphogenesis of the Body Axis. *Current Biology*
676 **28**:2479-2486.e4. doi:10.1016/j.cub.2018.05.079
677 Cavone L, McCann T, Drake LK, Aguzzi EA, Oprişoreanu A-M, Pedersen E, Sandi S,
678 Selvarajah J, Tsarouchas TM, Wehner D, Keatinge M, Mysiak KS, Henderson BEP, Dobie R,
679 Henderson NC, Becker T, Becker CG. 2021. A unique macrophage subpopulation signals
680 directly to progenitor cells to promote regenerative neurogenesis in the zebrafish spinal cord.
681 *Developmental Cell* **56**:1617-1630.e6. doi:10.1016/j.devcel.2021.04.031
682 Chen J, Cui Z, Yang S, Wu C, Li W, Bao G, Xu G, Sun Y, Wang L, Zhang J. 2017. The
683 upregulation of annexin A2 after spinal cord injury in rats may have implication for astrocyte
684 proliferation. *Neuropeptides* **61**:67–76. doi:10.1016/j.npep.2016.10.007
685 Choksi SP, Lauter G, Swoboda P, Roy S. 2014. Switching on cilia: transcriptional networks

686 regulating ciliogenesis. *Development* **141**:1427–1441. doi:10.1242/dev.074666
687 Collins P, Woollam DH. 1979. The ventricular surface of the subcommissural organ: a scanning
688 and transmission electron microscopic study. *J Anat* **129**:623–631.
689 Dale RM, Topczewski J. 2011. Identification of an evolutionarily conserved regulatory element
690 of the zebrafish col2a1a gene. *Developmental Biology* **357**:518–531.
691 doi:10.1016/j.ydbio.2011.06.020
692 Delous M, Baala L, Salomon R, Laclef C, Vierkotten J, Tory K, Golzio C, Lacoste T, Besse L,
693 Ozilou C, Moutkine I, Hellman NE, Anselme I, Silbermann F, Vesque C, Gerhardt C,
694 Rattenberry E, Wolf MTF, Gubler MC, Martinovic J, Encha-Razavi F, Boddaert N, Gonzales
695 M, Macher MA, Nivet H, Champion G, Berthélémé JP, Niaudet P, McDonald F, Hildebrandt
696 F, Johnson CA, Vekemans M, Antignac C, Rüther U, Schneider-Maunoury S, Attié-Bitach T,
697 Saunier S. 2007. The ciliary gene RPGRIP1L is mutated in cerebello-oculo-renal syndrome
698 (Joubert syndrome type B) and Meckel syndrome. *Nat Genet* **39**:875–881. doi:10.1038/ng2039
699 D'Gama PP, Qiu T, Cosacak MI, Rayamajhi D, Konac A, Hansen JN, Ringers C, Acuña-
700 Hinrichsen F, Hui SP, Olstad EW, Chong YL, Lim CKA, Gupta A, Ng CP, Nilges BS, Kashikar
701 ND, Wachten D, Liebl D, Kikuchi K, Kizil C, Yaksi E, Roy S, Jurisch-Yaksi N. 2021. Diversity
702 and function of motile ciliated cell types within ependymal lineages of the zebrafish brain. *Cell*
703 *Reports* **37**:109775. doi:10.1016/j.celrep.2021.109775
704 Didier R, Dastugue B, Meiniel A. 1995. The secretory material of the subcommissural organ of
705 the chick embryo. Characterization of a specific polypeptide by two-dimensional
706 electrophoresis. *Int J Dev Biol* **39**:493–499.
707 Escartin C, Galea E, Lakatos A, O'Callaghan JP, Petzold GC, Serrano-Pozo A, Steinhäuser C,
708 Volterra A, Carmignoto G, Agarwal A, Allen NJ, Araque A, Barbeito L, Barzilai A, Bergles
709 DE, Bonvento G, Butt AM, Chen W-T, Cohen-Salmon M, Cunningham C, Deneen B, De
710 Strooper B, Díaz-Castro B, Farina C, Freeman M, Gallo V, Goldman JE, Goldman SA, Götz
711 M, Gutiérrez A, Haydon PG, Heiland DH, Hol EM, Holt MG, Iino M, Kastanenka KV,
712 Kettenmann H, Khakh BS, Koizumi S, Lee CJ, Liddelow SA, MacVicar BA, Magistretti P,
713 Messing A, Mishra A, Molofsky AV, Murai KK, Norris CM, Okada S, Oliet SHR, Oliveira JF,
714 Panatier A, Parpura V, Pekna M, Pekny M, Pellerin L, Perea G, Pérez-Nievas BG, Pfrieger FW,
715 Poskanzer KE, Quintana FJ, Ransohoff RM, Riquelme-Perez M, Robel S, Rose CR, Rothstein
716 JD, Rouach N, Rowitch DH, Semyanov A, Sirko S, Sontheimer H, Swanson RA, Vitorica J,
717 Wanner I-B, Wood LB, Wu J, Zheng B, Zimmer ER, Zorec R, Sofroniew MV, Verkhratsky A.
718 2021. Reactive astrocyte nomenclature, definitions, and future directions. *Nat Neurosci*

24:312–325. doi:10.1038/s41593-020-00783-4

Finn R, Evans CC, Lee L. 2014. Strain-dependent brain defects in mouse models of primary ciliary dyskinesia with mutations in Pcdp1 and Spef2. *Neuroscience* **277**:552–567. doi:10.1016/j.neuroscience.2014.07.029

Gaillard A-L, Mohamad T, Quan FB, De Cian A, Mosimann C, Tostivint H, Pézeron G. 2023. Urp1 and Urp2 act redundantly to maintain spine shape in zebrafish larvae. *Developmental Biology* **496**:36–51. doi:10.1016/j.ydbio.2023.01.010

Gogendeau D, Lemullois M, Le Borgne P, Castelli M, Aubusson-Fleury A, Arnaiz O, Cohen J, Vesque C, Schneider-Maunoury S, Bouhouche K, Koll F, Tassin A-M. 2020. MKS-NPHP module proteins control ciliary shedding at the transition zone. *PLoS Biol* **18**:e3000640. doi:10.1371/journal.pbio.3000640

Grewal T, Wason SJ, Enrich C, Rentero C. 2016. Annexins – insights from knockout mice. *Biological Chemistry* **397**:1031–1053. doi:10.1515/hsz-2016-0168

Grimes DT, Boswell CW, Morante NFC, Henkelman RM, Burdine RD, Ciruna B. 2016. Zebrafish models of idiopathic scoliosis link cerebrospinal fluid flow defects to spine curvature. *Science* **352**:1341–1344. doi:10.1126/science.aaf6419

Haeussler M, Schönig K, Eckert H, Eschstruth A, Mianné J, Renaud J-B, Schneider-Maunoury S, Shkumatava A, Teboul L, Kent J, Joly J-S, Concordet J-P. 2016. Evaluation of off-target and on-target scoring algorithms and integration into the guide RNA selection tool CRISPOR. *Genome Biol* **17**:148. doi:10.1186/s13059-016-1012-2

Hall CJ, Boyle RH, Sun X, Wicker SM, Misa JP, Krissansen GW, Print CG, Crosier KE, Crosier PS. 2014. Epidermal cells help coordinate leukocyte migration during inflammation through fatty acid-fuelled matrix metalloproteinase production. *Nat Commun* **5**:3880. doi:10.1038/ncomms4880

Hayes M, Gao X, Yu LX, Paria N, Henkelman RM, Wise CA, Ciruna B. 2014. ptk7 mutant zebrafish models of congenital and idiopathic scoliosis implicate dysregulated Wnt signalling in disease. *Nat Commun* **5**:4777. doi:10.1038/ncomms5777

Hellman NE, Liu Y, Merkel E, Austin C, Le Corre S, Beier DR, Sun Z, Sharma N, Yoder BK, Drummond IA. 2010. The zebrafish *foxj1a* transcription factor regulates cilia function in response to injury and epithelial stretch. *Proc Natl Acad Sci USA* **107**:18499–18504. doi:10.1073/pnas.1005998107

Hitier M, Hamon M, Denise P, Lacoudre J, Thenint M-A, Mallet J-F, Moreau S, Quarck G. 2015. Lateral Semicircular Canal Asymmetry in Idiopathic Scoliosis: An Early Link between

752 Biomechanical, Hormonal and Neurosensory Theories? *PLoS ONE* **10**:e0131120.
753 doi:10.1371/journal.pone.0131120
754 Hughes CS, Foehr S, Garfield DA, Furlong EE, Steinmetz LM, Krijgsveld J. 2014.
755 Ultrasensitive proteome analysis using paramagnetic bead technology. *Molecular Systems*
756 *Biology* **10**:757. doi:10.15252/msb.20145625
757 Ignatenko O, Malinen S, Rybas S, Vihinen H, Nikkanen J, Kononov A, Jokitalo ES, Ince-Dunn
758 G, Suomalainen A. 2023. Mitochondrial dysfunction compromises ciliary homeostasis in
759 astrocytes. *Journal of Cell Biology* **222**:e202203019. doi:10.1083/jcb.202203019
760 Jensen VL, Li C, Bowie RV, Clarke L, Mohan S, Blacque OE, Leroux MR. 2015. Formation
761 of the transition zone by Mks5/Rpgrip1L establishes a ciliary zone of exclusion (CIZE) that
762 compartmentalises ciliary signalling proteins and controls PIP $_2$ ciliary abundance. *The EMBO*
763 *Journal* **34**:2537–2556. doi:10.15252/embj.201488044
764 Jorge-Torres OC, Szczesna K, Roa L, Casal C, Gonzalez-Somermeyer L, Soler M, Velasco CD,
765 Martínez-San Segundo P, Petazzi P, Sáez MA, Delgado-Morales R, Fourcade S, Pujol A,
766 Huertas D, Llobet A, Guil S, Esteller M. 2018. Inhibition of Gsk3b Reduces Nfkb1 Signaling
767 and Rescues Synaptic Activity to Improve the Rett Syndrome Phenotype in Mecp2-Knockout
768 Mice. *Cell Reports* **23**:1665–1677. doi:10.1016/j.celrep.2018.04.010
769 Jurisch-Yaksi N, Yaksi E, Kizil C. 2020. Radial glia in the zebrafish brain: Functional,
770 structural, and physiological comparison with the mammalian glia. *Glia* **68**:2451–2470.
771 doi:10.1002/glia.23849
772 Karner CM, Long F, Solnica-Krezel L, Monk KR, Gray RS. 2015. *Gpr126/Adgrg6* deletion in
773 cartilage models idiopathic scoliosis and pectus excavatum in mice. *Hum Mol Genet* **24**:4365–
774 4373. doi:10.1093/hmg/ddv170
775 Kimmel CB, Ballard WW, Kimmel SR, Ullmann B, Schilling TF. 1995. Stages of embryonic
776 development of the zebrafish. *Developmental Dynamics* **203**:253–310.
777 doi:10.1002/aja.1002030302
778 Kramer-Zucker AG, Olale F, Haycraft CJ, Yoder BK, Schier AF, Drummond IA. 2005. Cilia-
779 driven fluid flow in the zebrafish pronephros, brain and Kupffer's vesicle is required for normal
780 organogenesis. *Development* **132**:1907–1921. doi:10.1242/dev.01772
781 Kuhlmann K, Tschapek A, Wiese H, Eisenacher M, Meyer HE, Hatt HH, Oeljeklaus S,
782 Warscheid B. 2014. The Membrane Proteome of Sensory Cilia to the Depth of Olfactory
783 Receptors. *Molecular & Cellular Proteomics* **13**:1828–1843. doi:10.1074/mcp.M113.035378
784 Kwan KM, Fujimoto E, Grabher C, Mangum BD, Hardy ME, Campbell DS, Parant JM, Yost

785 HJ, Kanki JP, Chien C. 2007. The Tol2kit: A multisite gateway-based construction kit for *Tol2*
786 transposon transgenesis constructs. *Developmental Dynamics* **236**:3088–3099.
787 doi:10.1002/dvdy.21343
788 Lattke M, Magnutzki A, Walther P, Baumann B. 2012. Nuclear Factor κB Activation Impairs
789 Ependymal Ciliogenesis and Links Neuroinflammation to Hydrocephalus Formation. *J*
790 *Neurosci* **32**:11511–11523. doi:10.1523/JNEUROSCI.0182-12.2012
791 Lessieur EM, Song P, Nivar GC, Piccillo EM, Fogerty J, Rozic R, Perkins BD. 2019. Ciliary
792 genes arl13b, ahi1 and cc2d2a differentially modify expression of visual acuity phenotypes but
793 do not enhance retinal degeneration due to mutation of cep290 in zebrafish. *PLoS One*
794 **14**:e0213960. doi:10.1371/journal.pone.0213960
795 Lu H, Shagirova A, Goggi JL, Yeo HL, Roy S. 2020. Reissner fibre-induced urotensin
796 signalling from cerebrospinal fluid-contacting neurons prevents scoliosis of the vertebrate
797 spine. *Biology Open* **9**:bio052027. doi:10.1242/bio.052027
798 Lyons DA, Talbot WS. 2015. Glial Cell Development and Function in Zebrafish. *Cold Spring*
799 *Harb Perspect Biol* **7**:a020586. doi:10.1101/cshperspect.a020586
800 Mahuzier A, Gaudé H-M, Grampa V, Anselme I, Silbermann F, Leroux-Berger M, Delacour
801 D, Ezan J, Montcouquiol M, Saunier S, Schneider-Maunoury S, Vesque C. 2012. Dishevelled
802 stabilization by the ciliopathy protein Rpgrip1l is essential for planar cell polarity. *Journal of*
803 *Cell Biology* **198**:927–940. doi:10.1083/jcb.201111009
804 Mangos S, Lam P, Zhao A, Liu Y, Mudumana S, Vasilyev A, Liu A, Drummond IA. 2010. The
805 ADPKD genes *pkd1a/b* and *pkd2* regulate extracellular matrix formation. *Disease Models &*
806 *Mechanisms* **3**:354–365. doi:10.1242/dmm.003194
807 Masek M, Etard C, Hofmann C, Hülsmeier AJ, Zang J, Takamiya M, Gesemann M, Neuhauss
808 SCF, Hornemann T, Strähle U, Bachmann-Gagescu R. 2022. Loss of the Bardet-Biedl protein
809 Bbs1 alters photoreceptor outer segment protein and lipid composition. *Nat Commun* **13**:1282.
810 doi:10.1038/s41467-022-28982-6
811 Matusova Z, Hol EM, Pekny M, Kubista M, Valihrach L. 2023. Reactive astrogliosis in the era
812 of single-cell transcriptomics. *Front Cell Neurosci* **17**:1173200.
813 doi:10.3389/fncel.2023.1173200
814 Medina M, Avila J. 2010. Glycogen Synthase Kinase-3 (GSK-3) Inhibitors for the Treatment
815 of Alzheimers Disease. *CPD* **16**:2790–2798. doi:10.2174/138161210793176581
816 Meyer-Miner A, Van Gennip JLM, Henke K, Harris MP, Ciruna B. 2022. Resolving primary
817 pathomechanisms driving idiopathic-like spinal curvature using a new katnb1 scoliosis model.

818 *iScience* **25**:105028. doi:10.1016/j.isci.2022.105028
819 Mines MA, Beurel E, Jope RS. 2011. Regulation of Cell Survival Mechanisms in Alzheimer's
820 Disease by Glycogen Synthase Kinase-3. *International Journal of Alzheimer's Disease* **2011**:1–
821 11. doi:10.4061/2011/861072
822 Mukherjee I, Roy S, Chakrabarti S. 2019. Identification of Important Effector Proteins in the
823 FOXJ1 Transcriptional Network Associated With Ciliogenesis and Ciliary Function. *Front*
824 *Genet* **10**:23. doi:10.3389/fgene.2019.00023
825 Olstad EW, Ringers C, Hansen JN, Wens A, Brandt C, Wachten D, Yaksi E, Jurisch-Yaksi N.
826 2019. Ciliary Beating Compartmentalizes Cerebrospinal Fluid Flow in the Brain and Regulates
827 Ventricular Development. *Current Biology* **29**:229-241.e6. doi:10.1016/j.cub.2018.11.059
828 Parmentier C, Hameury E, Dubessy C, Quan FB, Habert D, Calas A, Vaudry H, Lihrmann I,
829 Tostivint H. 2011. Occurrence of Two Distinct Urotensin II-Related Peptides in Zebrafish
830 Provides New Insight into the Evolutionary History of the Urotensin II Gene Family.
831 *Endocrinology* **152**:2330–2341. doi:10.1210/en.2010-1500
832 Patten SA, Margaritte-Jeannin P, Bernard J-C, Alix E, Labalme A, Besson A, Girard SL, Fendri
833 K, Fraisse N, Biot B, Poizat C, Campan-Fournier A, Abelin-Genevois K, Cunin V, Zaouter C,
834 Liao M, Lamy R, Lesca G, Menassa R, Marcaillou C, Letexier M, Sanlaville D, Berard J,
835 Rouleau GA, Clerget-Darpoux F, Drapeau P, Moldovan F, Edery P. 2015. Functional variants
836 of POC5 identified in patients with idiopathic scoliosis. *J Clin Invest* **125**:1124–1128.
837 doi:10.1172/JCI77262
838 Perez-Riverol Y, Bai J, Bandla C, García-Seisdedos D, Hewapathirana S, Kamatchinathan S,
839 Kundu DJ, Prakash A, Frericks-Zipper A, Eisenacher M, Walzer M, Wang S, Brazma A,
840 Vizcaíno JA. 2022. The PRIDE database resources in 2022: a hub for mass spectrometry-based
841 proteomics evidences. *Nucleic Acids Research* **50**:D543–D552. doi:10.1093/nar/gkab1038
842 Prendergast AE, Jim KK, Marnas H, Desban L, Quan FB, Djenoune L, Laghi V, Hocquemiller
843 A, Lunsford ET, Roussel J, Keiser L, Lejeune F-X, Dhanasekar M, Bardet P-L, Levraud J-P,
844 Van De Beek D, Vandenbroucke-Grauls CMJE, Wyart C. 2023. CSF-contacting neurons
845 respond to Streptococcus pneumoniae and promote host survival during central nervous system
846 infection. *Current Biology* **33**:940-956.e10. doi:10.1016/j.cub.2023.01.039
847 Quan FB, Dubessy C, Galant S, Kenigfest NB, Djenoune L, Leprince J, Wyart C, Lihrmann I,
848 Tostivint H. 2015. Comparative Distribution and In Vitro Activities of the Urotensin II-Related
849 Peptides URP1 and URP2 in Zebrafish: Evidence for Their Colocalization in Spinal
850 Cerebrospinal Fluid-Contacting Neurons. *PLoS ONE* **10**:e0119290.

doi:10.1371/journal.pone.0119290

Quigley IK, Kintner C. 2017. Rfx2 Stabilizes Foxj1 Binding at Chromatin Loops to Enable Multiciliated Cell Gene Expression. *PLoS Genet* **13**:e1006538. doi:10.1371/journal.pgen.1006538

Rentero C, Blanco-Muñoz P, Meneses-Salas E, Grewal T, Enrich C. 2018. Annexins—Coordinators of Cholesterol Homeostasis in Endocytic Pathways. *IJMS* **19**:1444. doi:10.3390/ijms19051444

Ribeiro A, Monteiro JF, Certal AC, Cristovão AM, Saúde L. 2017. Foxj1a is expressed in ependymal precursors, controls central canal position and is activated in new ependymal cells during regeneration in zebrafish. *Open Biol* **7**:170139. doi:10.1098/rsob.170139

Rose CD, Pompili D, Henke K, Van Gennip JLM, Meyer-Miner A, Rana R, Gobron S, Harris MP, Nitz M, Ciruna B. 2020. SCO-Spondin Defects and Neuroinflammation Are Conserved Mechanisms Driving Spinal Deformity across Genetic Models of Idiopathic Scoliosis. *Current Biology* **30**:2363-2373.e6. doi:10.1016/j.cub.2020.04.020

Schindelin J, Arganda-Carreras I, Frise E, Kaynig V, Longair M, Pietzsch T, Preibisch S, Rueden C, Saalfeld S, Schmid B, Tinevez J-Y, White DJ, Hartenstein V, Eliceiri K, Tomancak P, Cardona A. 2012. Fiji: an open-source platform for biological-image analysis. *Nat Methods* **9**:676–682. doi:10.1038/nmeth.2019

Shan Y, Fang C, Cheng C, Wang Y, Peng J, Fang W. 2015. Immersion infection of germ-free zebrafish with Listeria monocytogenes induces transient expression of innate immune response genes. *Front Microbiol* **6**. doi:10.3389/fmicb.2015.00373

Sherman J, Barkovich A, Citrin C. 1987. The MR appearance of syringomyelia: new observations. *American Journal of Roentgenology* **148**:381–391. doi:10.2214/ajr.148.2.381

Sofroniew MV. 2015. Astrogliosis. *Cold Spring Harb Perspect Biol* **7**:a020420. doi:10.1101/cshperspect.a020420

Song P, Fogerty J, Cianciolo LT, Stupay R, Perkins BD. 2020. Cone Photoreceptor Degeneration and Neuroinflammation in the Zebrafish Bardet-Biedl Syndrome 2 (bbs2) Mutant Does Not Lead to Retinal Regeneration. *Front Cell Dev Biol* **8**:578528. doi:10.3389/fcell.2020.578528

Sullivan-Brown J, Schottenfeld J, Okabe N, Hostetter CL, Serluca FC, Thiberge SY, Burdine RD. 2008. Zebrafish mutations affecting cilia motility share similar cystic phenotypes and suggest a mechanism of cyst formation that differs from pkd2 morphants. *Developmental Biology* **314**:261–275. doi:10.1016/j.ydbio.2007.11.025

884 Troutwine BR, Gontarz P, Konjikusic MJ, Minowa R, Monstad-Rios A, Sepich DS, Kwon RY,
885 Solnica-Krezel L, Gray RS. 2020. The Reissner Fiber Is Highly Dynamic In Vivo and Controls
886 Morphogenesis of the Spine. *Current Biology* **30**:2353-2362.e3. doi:10.1016/j.cub.2020.04.015
887 Tsujikawa M, Malicki J. 2004. Intraflagellar Transport Genes Are Essential for Differentiation
888 and Survival of Vertebrate Sensory Neurons. *Neuron* **42**:703–716. doi:10.1016/S0896-
889 6273(04)00268-5
890 Van Gennip JLM, Boswell CW, Ciruna B. 2018. Neuroinflammatory signals drive spinal curve
891 formation in zebrafish models of idiopathic scoliosis. *Sci Adv* **4**:eaav1781.
892 doi:10.1126/sciadv.aav1781
893 van Rooijen E, Giles RH, Voest EE, van Rooijen C, Schulte-Merker S, van Eeden FJ. 2008.
894 LRRC50, a conserved ciliary protein implicated in polycystic kidney disease. *J Am Soc Nephrol*
895 **19**:1128–1138. doi:10.1681/ASN.2007080917
896 Viau A, Bienaimé F, Lukas K, Todkar AP, Knoll M, Yakulov TA, Hofherr A, Kretz O,
897 Helmstädter M, Reichardt W, Braeg S, Aschman T, Merkle A, Pfeifer D, Dumit VI, Gubler M,
898 Nitschke R, Huber TB, Terzi F, Dengjel J, Grahammer F, Köttgen M, Busch H, Boerries M,
899 Walz G, Triantafyllopoulou A, Kuehn EW. 2018. Cilia-localized LKB 1 regulates chemokine
900 signaling, macrophage recruitment, and tissue homeostasis in the kidney. *The EMBO Journal*
901 **37**:e98615. doi:10.15252/embj.201798615
902 Vierkotten J, Dildrop R, Peters T, Wang B, Rüther U. 2007. Ftm is a novel basal body protein
903 of cilia involved in Shh signalling. *Development* **134**:2569–2577. doi:10.1242/dev.003715
904 Wang J, Thomas HR, Thompson RG, Waldrep SC, Fogerty J, Song P, Li Z, Ma Y, Santra P,
905 Hoover JD, Yeo NC, Drummond IA, Yoder BK, Amack JD, Perkins B, Parant JM. 2022.
906 Variable phenotypes and penetrance between and within different zebrafish ciliary transition
907 zone mutants. *Disease Models & Mechanisms* **15**:dmm049568. doi:10.1242/dmm.049568
908 Wieczorek S, Combes F, Lazar C, Giai Gianetto Q, Gatto L, Dorffer A, Hesse A-M, Couté Y,
909 Ferro M, Bruley C, Burger T. 2017. DAPAR & ProStaR: software to perform statistical
910 analyses in quantitative discovery proteomics. *Bioinformatics* **33**:135–136.
911 doi:10.1093/bioinformatics/btw580
912 Wiegering A, Rüther U, Gerhardt C. 2018. The ciliary protein Rpgrip1l in development and
913 disease. *Developmental Biology* **442**:60–68. doi:10.1016/j.ydbio.2018.07.024
914 Xie H, Kang Y, Liu J, Huang M, Dai Z, Shi J, Wang S, Li L, Li Y, Zheng P, Sun Y, Han Q,
915 Zhang J, Zhu Z, Xu L, Yelick PC, Cao M, Zhao C. 2023. Ependymal polarity defects coupled
916 with disorganized ciliary beating drive abnormal cerebrospinal fluid flow and spine curvature

917 in zebrafish. *PLoS Biol* **21**:e3002008. doi:10.1371/journal.pbio.3002008
918 Yu X, Ng CP, Habacher H, Roy S. 2008. Foxj1 transcription factors are master regulators of
919 the motile ciliogenic program. *Nat Genet* **40**:1445–1453. doi:10.1038/ng.263
920 Zamanian JL, Xu L, Foo LC, Nouri N, Zhou L, Giffard RG, Barres BA. 2012. Genomic
921 Analysis of Reactive Astrogliosis. *J Neurosci* **32**:6391–6410. doi:10.1523/JNEUROSCI.6221-
922 11.2012
923 Zhang X, Jia S, Chen Z, Chong YL, Xie H, Feng D, Wu X, Song DZ, Roy S, Zhao C. 2018.
924 Cilia-driven cerebrospinal fluid flow directs expression of urotensin neuropeptides to straighten
925 the vertebrate body axis. *Nat Genet* **50**:1666–1673. doi:10.1038/s41588-018-0260-3
926 Zhou Y, Zhou B, Pache L, Chang M, Khodabakhshi AH, Tanaseichuk O, Benner C, Chanda
927 SK. 2019. Metascape provides a biologist-oriented resource for the analysis of systems-level
928 datasets. *Nat Commun* **10**:1523. doi:10.1038/s41467-019-09234-6
929
930
931

932 **MATERIAL AND METHODS**

933 ***Zebrafish***

934 Wild-type, *rpgrip1l*^{ex4} and *rpgrip1l*$^{\Delta}$ zebrafish embryos and adults were raised, staged
935 and maintained as previously described (Kimmel et al., 1995). All our experiments
936 were made in agreement with the european Directive 210/63/EU on the protection of
937 animals used for scientific purposes, and the French application decree 'Décret 2013-
938 118'. The projects of our group have been approved by our local ethical committee
939 'Comité d'éthique Charles Darwin'. The authorization number is APAFIS #31540-
940 2021051809258003 v4. The fish facility has been approved by the French 'Service for
941 animal protection and health' with approval number A750525. All experiments were
942 performed on Danio rerio embryos of mixed AB/TL background. Animals were raised
943 at 28.5°C under a 14/10 light/dark cycle.

944 ***Rpgrip1l mutant generation and genotyping***
945
946 Guide RNA preparation and microinjection
947 CRISPR target sites were selected for their high predicted specificity and efficiency
948 using the CRISPOR online tool (Haeussler et al., 2016). Real efficiency was assessed
949 on zebrafish embryos by T7E1 test. The two most efficient guides (Rpgrip1l_x4_G1:
950 GCTTACGGTCCTTCACCAGACGG and Rpgrip1l_x25_G3:
951 CCTCAGTTGACAGGTTTCAGCGG) respectively situated 24 nt from the beginning of
952 exon 4 and 82 nt downstream of exon 25 were kept for further experiments.
953 sgRNA transcription templates were obtained by PCR using T7_Rpgrip1l-x4_G1_Fw
954 primer (5′-
955 GAAATTAATACGACTCACTATAGGCTTACGGTCCTTCACCAGAGTTTTAGAGCTA
956 GAAATAGC- 3′) or T7_Rpgrip1l-x25_G3_Fw (5′-
957 GAAATTAATACGACTCACTATAGGCCTCAGTTGACAGGTTTCAGGTTTTAGAGCT
958 AGAAATAG C-3′) as forward primer and sgRNA_R universal primer (5′-
959 AAAAGCACCGACTCGGTGCCACTTTTTCAAGTTGATAACGGACTAGCCTTATTTT
960 AACTTGCTA TTTCTAGCTCTAAAAC-3′) as reverse primer. sgRNAs were
961 transcribed using Megascript T7 Transcription Kit (Thermo Fisher Scientific, Waltham,
962 MA) and purified using NucleoSpin® RNA Clean up XS kit (Macherey Nagel, Düren,
963 Germany). sgRNA:Cas9 RNP complex was obtain by incubating Cas9 protein (gift of

964 TACGENE, Paris, France) (7.5 µM) with sgRNA (10 µM) in 20 mM Hepes-NaOH pH
965 7.5, 150 mM KCl for 10 min at 28 °C. 1–2 nl was injected per embryo. For deletion,
966 Rpgrip1l_x4_G1 and Rpgrip1l_x25_G3 RNP complexes were mixed half and half.
967 We kept two F1 fish, one with a 15 Kb deletion between exon 4 and 25 of *rpgrip1l*, that
968 we called *rpgrip1l*$^{\Delta}$ and that we submitted to ZFIN under the name *rpgrip1l* ^{bps1}and a
969 second one with a stop codon within exon 4 called *rpgrip1l* ^{ex4}*,* that is submitted to ZFIN
970 under the name *rpgrip1l* ^{bps2}*.*
971
972 Screening and genotyping
973 Injected (F0) fish were screened for germline transmission by crossing with wild type
974 fish and extracting genomic DNA from resulting embryos. For genomic DNA extraction,
975 caudal fin (juveniles/adults) or whole embryo DNA were used. Genomic DNA was
976 isolated with Proteinase K (PK) digestion in 40 of lysis buffer (100 mM Tris-HCl pH 7.5,
977 1 mM EDTA, 250 mM NaCl, 0.2% SDS, 0.1 µg/µl Proteinase K (PK)) for embryos (300
978 µl for adult fin) overnight at 37°C with agitation. PK was inactivated for 10 min at 90°C
979 and a five-fold dilution was used as template for PCR amplification. Combined
980 genotyping of wild type and mutant alleles (Supplementary Figure S1A') was
981 performed by PCR using 3 primers, a common reverse primer for both alleles :
982 Rpgrip1l_ex25_R3 (GTTGTGTCTCTGCCATATATTG), a specific forward primer for
983 the deleted allele: Rpgrip1l-ex4-del (CCCACACTGCATACGCACTC) and a specific
984 forward primer for the wild type allele : Rpgrip1l_ex25F
985 (AGTGTGCGGTACATCTCCAA) at an annealing temperature of 60°C for 35 cycles.
986 Expected size of the amplified fragment is 364 nt for the wild type allele and 544nt for
987 the mutant allele. The deleted allele presents a frameshift at position N77 leading to
988 the generation of a STOP codon after 11 aas, thus leading to a N-terminally truncated
989 protein at position 88/1256 aas.
990 For genotyping the *urp2* mutant line, caudal fins from adult fish were extracted in 300µl
991 of lysis solution and PCR was performed as above to detect exon 5 deletion using the
992 following primers: urp2-F1 (TGATTACTAGCCCTGTCCCAAC) and urp2-R1
993 (AGGTACAGTACACACGTCACAG).
994
995 ***µCT scans***

996 The samples were scanned on a Bruker micro scanner (Skyscan 1272) with a
997 resolution of 8.5 µm, a rotation step of 0.55° and a total rotation of 180°. For the
998 acquisition of adult fish (2.5 cm), a 0.25 mm aluminium filter was used, for a voltage of
999 50 kV and an intensity of 180 mA, for juvenile fish (0.9 to 1.2 cm) the filter was omitted,
1000 and a voltage of 60 kV was used with an intensity of 166 mA. Each image contained
1001 1008 x 672 pixels and was based on the average of 3 images. The 3D reconstruction
1002 by backprojection was carried out by the NRecon software and the 2D image overlays
1003 were then cleaned by the CT Analyser software. The Dataviewer software allowed all
1004 fish skeletons to be oriented in the same way taking the otoliths as landmarks. The
1005 CTvox software then allowed 3D visualizing of the samples. Morphometric analysis
1006 was performed with the CT Analyser software.
1007
1008 ***Scanning electron microscopy***
1009 3 month fish (3 controls, 5 mutants) were euthanized using lethal concentration of
1010 MS222 (0.028 mg/mL). The brains were quickly dissected in 1.22 X PBS (pH 7.4), 0.1
1011 M sodium cacodylate and fixed overnight with 2% glutaraldehyde in 0.61 X PBS (pH
1012 7.4), 0.1 M sodium cacodylate at 4°C. They were sectioned along the dorsal midline
1013 with a razor blade to expose their ventricular surfaces. Both halves were washed four
1014 times in 1.22 X PBS and post-fixed for 15 minutes in 1.22 X PBS containing 1% OsO4.
1015 Fixed samples were washed four times in ultrapure water, dehydrated with a graded
1016 series of ethanol and critical point dried (CPD 300, Leica) at 79 bar and 38 °C with
1017 liquid CO2 as the transition fluid and then depressurized slowly (0,025 bar/s). They
1018 were then mounted on aluminum mounts with conductive silver cement. Sample
1019 surfaces were coated with a 5 nm platinum layer using a sputtering device (ACE 600,
1020 Leica). Samples were observed under high vacuum conditions using a Field Emission
1021 Scanning Electron Microscope (Gemini 500, Zeiss) operating at 5 kV, with a 20 µm
1022 objective aperture diameter and a working distance around 3 mm. Secondary electrons
1023 were collected with an in-lens detector. Scan speed and line compensation integrations
1024 were adjusted during observation.
1025
1026 ***Histological sections of juvenile and immunofluorescence on sections***
1027 Juvenile and adult zebrafish were euthanized using lethal concentration of MS222
1028 (0.028 mg/mL). Pictures and size measurements were systematically taken before

1029 fixation. Fish were fixed in Zamboni fixative [35 ml PFA 4 %, 7.5 ml saturated picric
1030 acid (1.2 %), 7.5 ml 0.2M Phosphate Buffer (PB)] [55] overnight at 4°C under agitation.
1031 Fish were washed with Ethanol 70% and processed for dehydration by successive 1 h
1032 incubation in Ethanol (3 x 70% and 2 x 100%) at room temperature under agitation,
1033 then for paraffin inclusion. 14 µm sagittal paraffin sections were obtained using a Leica
1034 RM2125RT microtome. Sections were deparaffinized and antigen retrieval was
1035 performed by incubation for 7 min in boiling citrate buffer (10 mM, pH 6).
1036 Immunofluorescence staining was performed as described previously (Andreu-
1037 Cervera et al., 2019). The following primary antibodies were used: anti-RF, anti-
1038 Acetylated Tubulin, anti-Glutamylated Tubulin, anti-Arl13b, anti-LCP1, anti-AnnexinA2.
1039 Corresponding primary and secondary antibodies are described and referenced in the
1040 Resources Table.
1041
1042 ***Immunofluorescence on whole embryos***
1043 Embryos from 24 to 40 hpf were fixed 4 hr to overnight in 4% paraformaldehyde (PFA)
1044 at 4°C. For Reissner fiber staining, larvae at 48 and 72 hpf were fixed 2 hr in 4% PFA
1045 and 3% sucrose at 4°C, skin from the rostral trunk and yolk were removed. Samples
1046 from 24 to 40 hpf embryos were blocked overnight in a solution containing 0.5% Triton,
1047 1% DMSO, 10% normal goat serum and 2 mg/mL BSA. For older samples (48 to 72
1048 hpf) triton concentration was increased to 0.7%. Primary antibodies were incubated
1049 one to two nights at 4°C in a buffer containing 0.5% Triton, 1% DMSO, 1% NGS and
1050 1 mg/mL BSA. All secondary antibodies were from Molecular Probes, used at 1:400 in
1051 blocking buffer, and incubated a minimum of 2.5 hr at room temperature. The primary
1052 antibodies chosen for in toto immuno-labeling against Reissner fiber, Acetylated-
1053 tubulin, Myc, Arl13b and Gamma-tubulin as well as the corresponding secondary
1054 antibodies are referenced in the Key Resources Table. Whole mount zebrafish
1055 embryos (dorsal or lateral mounting in Vectashield Mounting Medium) were imaged on
1056 a Leica SP5 confocal microscope and Zeiss LSM910 confocal microscope, both
1057 equipped with a 63X immersion objective. Images were then processed using Fiji
1058 (Schindelin et al., 2012).
1059
1060 ***Whole-mount brain clearing***

1061 Brains were dissected from 4-5 wpf size-matched (0.9-1.2 mm length) zebrafish after
1062 in toto fixation with formaldehyde. Whole–mount tissue clearing was performed
1063 following the zPACT protocol (Affaticati et al., 2017). In brief, brains were infused for 2
1064 days in hydrogel monomer solution (4% acrylamide, 0.25% VA- 044, 1% formaldehyde
1065 and 5% DMSO in 1X PBS) at 4°C. Polymerization was carried out for 2h30 at 37°C in
1066 a desiccation chamber filled with pure nitrogen. Brains were transferred into histology
1067 cassettes and incubated in clearing solution (8% SDS and 200 mM boric acid in dH2O)
1068 at 37°C with gentle agitation for 8 days. Cleared brains were washed in 1X PBS with
1069 0.1% Tween-20 (PBT) for 3 days at room temperature and kept in 0.5% formaldehyde,
1070 0.05% sodium azide in PBT at 4°C until further processing. Brains were subsequently
1071 placed for 1h in depigmentation pre-incubation solution (0.5X SSC, 0.1% Tween-20 in
1072 dH2O) at room temperature. The solution was replaced by depigmentation solution
1073 (0.5X SSC, Triton X-100 0.5%, formamide 0.05% and H2O2 0.03% in dH2O) for 45
1074 minutes at room temperature. Depigmented brains were washed for 4h in PBT and
1075 post-fixed (2% formaldehyde and 2% DMSO in PBT) overnight at 4°C.
1076
1077 ***Cleared brain immunostaining of whole adult brains***
1078 Whole-mount immunolabeling of cleared brains was performed as described in the
1079 zPACT protocol with slight modifications. Briefly, brains were washed in PBT for one
1080 day at room temperature and blocked for 10h in 10% normal goat serum, 10% DMSO,
1081 5% PBS-glycine 1M and 0.5% Triton X-100 in PBT at room temperature. Brains were
1082 washed again in PBT for 1h prior to incubation with anti- ZO-1 antibody (ZO1-1A12,
1083 Thermofisher, 1:150) in staining solution (2% normal goat serum, 10% DMSO, 0.1%
1084 Tween-20, 0.1% Triton X-100 and 0.05% sodium azide in PBT) for 12 days at room
1085 temperature under gentle agitation. Primary antibody was renewed once after 6 days
1086 of incubation. Samples were washed three times in PBT and thereafter incubated with
1087 Alexa Fluor 488-conjugated secondary antibody (A11001, Invitrogen, 1:200) for 10
1088 days in the staining solution at room temperature under gentle agitation. Secondary
1089 antibody was renewed once after 5 days of incubation. Samples were washed three
1090 times in PBT prior to a counterstaining with DiIC18 (D282, Invitrogen, 1µM) in the
1091 staining solution for three days at room temperature with gentle agitation. Samples
1092 were washed in PBT for 3h before mounting procedure.
1093

1094 ***Mounting and confocal imaging***

1095 Samples were placed in 50% fructose-based high-refractive index solution (fbHRI, see
1096 (Affaticati et al., 2017) /50% PBT for 1h, then in 100% fbHRI. Brains were mounted in
1097 agarose-coated (1% in standard embryo medium) 60 mm Petri dish with custom
1098 imprinted niches to help orientation. Niche-fitted brains were embedded in 1% phytagel
1099 and the Petri dish filled with 100% fbHRI. fbHRI was changed three times before
1100 imaging until its refractive index matched 1.457. Images were acquired with a Leica
1101 TCS SP8 laser scanning confocal microscope equipped with a Leica HC FLUOTAR L
1102 25x/1.00 IMM motCorr objective. Brains were scanned at a resolution of
1103 1.74x1.74x1.74 µm (xyz) and tiled into 45 to 70 individual image stacks, depending on
1104 brain dimensions, subsequently stitched, using LAS X software.

1105

1106 ***Volumetric analysis of the posterior ventricles***

1107 The volumes of the posterior ventricles were segmented, reconstructed and analyzed
1108 using Amira for Life & Biomedical Sciences software (Thermo Fisher Scientific). In
1109 essence the ventricles volumes were manually segmented in Amira's segmentation
1110 editor and subsequently refined by local thresholding and simplification of the
1111 corresponding surfaces. Volumes, which were open to the environment were artificially
1112 closed with minimal surfaces by connecting the distal-most points of their surface to
1113 the contralaterally corresponding points using straight edges. Due to the biologic
1114 variability of the sample population the overall size of the specimens needed to be
1115 normalized to keep the measured volumes comparable. For this spatial normalization
1116 one of the specimens was randomly selected from the wildtype population as template
1117 (1664, grey) and the 'Registration' module in Amira was used to compute region-
1118 specific rigid registrations for the other specimens, allowing for isotropic scaling only
1119 [details in supp. mat.]. For excluding the influence of the ventricular volumes, the
1120 registration was computed on the basis of the independent reference stain (DiIC18)
1121 (details in supp. mat.). Region specific volume differences between the mutant and
1122 wildtype population were evaluated on seven subvolumes of the posterior ventricles
1123 (details in supp. mat.).

1124

1125 ***RNA extraction for transcriptome analysis and quantitative RT-PCR***

1126 Juvenile and adult zebrafish were euthanized using lethal concentration of MS222
1127 (0.28 mg/mL). Their length was measured and their fin cut-off for genotyping. For
1128 transcriptomic analysis, brain and dorsal trunk from 1 month juvenile (0.9 to 1.0 cm)
1129 zebrafish were dissected in cold PBS with forceps and lysed in QIAzol (QIAGEN) after
1130 homogenization with plunger pistons and 1ml syringes. Samples were either stored in
1131 QIAzol at -80°C or immediately processed. Extracts containing RNA were loaded onto
1132 QIAGEN-mini columns, DNAse digested and purified in the miRNAeasy QIAGEN kit
1133 (Cat 217004) protocol. Samples were stored at -80°C until use. RNA concentration and
1134 size profile were obtained on the Tapestation of ICM platform. All preparations had a
1135 RIN above 9.2. For Q-PCR from juveniles, whole fish minus internal organs were lysed
1136 in Trizol (Life technologies) using the Manufacturer protocol.
1137
1138 ***Quantitative PCR from individual juvenile or adult fish***
1139 The cDNA from the isolated RNAs was obtained following GoScript Reverse
1140 Transcription System protocol (Promega), using 3 to 4 µg of total RNA for each sample.
1141 The 20 µL RT-reaction was diluted 4-fold and 4µl was used for each amplification
1142 performed in duplicates. The primers used for qPCR were the following: urp2 (F:
1143 ACCAGAGGAAACAGCAATGGAC; R: TGAGGTTTCCATCCGTCACTAC), *urp1* (F:
1144 ACATTCTGGCTGTGGTTTGTTC; R: CTCTTTTGCACCTCTCTGAAGC), *urp* (F:
1145 GCGGAAAAATGTCATGCCTCTTC; R: TTGAGCTCCTTTTGAAGCTCCTG), *uts2a*
1146 (F: CACTGCTCAACAGAGACAGTATCA; R: CCAAAAGACCACTGGGAGGAAC),
1147 *uts2b* (F: TACCCGTCTCTCATCAGTGGAG; R: TTTTCCAGCAAGGCCTCTTTTAC)
1148 where all of them are from Gaillard et al. 2023, *rpgrip1l* (F:
1149 CAGACACCTGCTGGAGTTACA; R: TCCTGACTCACATCAAACGCA), *irg1l* (F:
1150 TCCCTAAGAGGTTCCATCCTCC; R: AAGATGCAGCGATGGCCAAA), *stat3* (F:
1151 CAGGACTGGGCGTATGCG; R: GAAGCGGCTGTACTGCTGAT), *c4b* (F:
1152 GGGTGTTCTTATGGCGGTGG and R: GCGCACAACAAGCTTTTCTCATC) *lsm12b*
1153 (F: GAGACTCCTCCTCCTCTAGCAT and R: GATTGCATAGGCTTGGGACAAC).
1154 The Q-PCR were performed using the StepOne real-time PCR system and following
1155 its standard amplification protocol (Thermo Scientific). Relative gene expression levels
1156 were quantified using the comparative CT method ($2^{-\Delta\Delta CT}$ method or $2^{-\Delta CT}$) on the basis
1157 of CT values for target genes and *lsm12b* as internal control.
1158

1159 ***RNA-sequencing and analysis***

1160 RNA-seq libraries were constructed by the ICM Platform (PARIS) from 100 ng of total
1161 RNA using the KAPA mRNA Hyperprep kit (Roche) that allows to obtain stranded
1162 polyA libraries, and their quality controlled on Agilent Tape station. The sequencing
1163 was performed on a NovaSeq 6000 Illumina for both strands. Sequences were aligned
1164 against the GRCz11 version of zebrafish genome using **RNA Star function** in "Galaxy"
1165 environment. The 12 Brain libraries reached between 22 to 26 Millions of assigned
1166 reads, and the trunk libraries between 26 to 35 Millions of assigned reads. Expression
1167 level for each gene was determined using **Feature counts function** from RNA Star
1168 BAM files. **DESeq2 function** was used to calculate the log2 Fold change and adjusted
1169 P values from the Wald test for each gene comparing the 7 mutants raw count
1170 collection to the 5 controls raw counts collection. Volcano plots were generated using
1171 the Log2 fold change and P adj. value of each Gene ID from the DESeq2 table. A
1172 threshold of 5.10 E-2 was chosen for the Padj. values and a log2 fold change > to
1173 +0.75 or < to -0.75 to select significantly up or down-regulated regulated genes. Both
1174 gene lists were used as input to search for enriched GO terms and KEGGs pathways
1175 using Metascape software (Zhou et al., 2019) as well as to compare up-regulated
1176 genes in the dorsal trunk versus the brain using Galaxy.

1177

1178 **Quantitative proteomics**

1179 *Sample preparation:* Adult zebrafish were euthanized using lethal concentration of
1180 MS222 (0.28 mg/mL). For proteomic analysis, brain from 3 months zebrafish were
1181 dissected in cold PBS with forceps and immediately flash frozen in liquid nitrogen and
1182 stored at -80°C. Zebrafish brain samples were lysed in RIPA buffer (Sigma) with 1/100
1183 antiprotease and sonicated for 5 minutes. After a 660 nm protein assay (Thermo),
1184 samples were digested using a Single Pot Solid Phase enhanced Sample Preparation
1185 (SP3) protocol (Hughes et al., 2014). In brief, 40 µg of each protein extract was reduced
1186 with 12mM dithiothreitol (DTT) and alkylated using 40 mM iodoacetamic acid (IAM). A
1187 mixture of hydrophilic and hydrophobic magnetic beads was used to clean-up the
1188 proteins at a ratio of 20:1 beads:proteins (Sera-Mag Speed beads, Fisher Scientific).
1189 After addition of ACN to a final concentration of 50%, the beads were allowed to bind
1190 to the proteins for 18 minutes. Protein-bead mixtures were washed twice with 80%
1191 EtOH and once with 100% ACN. The protein-bead complexes were digested with a

1192 mixture of trypsin:LysC (Promega) at a 1:20 ratio overnight at 37°C. Extracted peptides
1193 were cleaned-up using automated C18 solid phase extraction on the Bravo AssayMAP
1194 platform (Agilent Technologies).
1195
1196 *NanoLC-MS-MS analysis*
1197 The peptide extracts were analysed on a nanoLC-TimsTof Pro coupling (Bruker
1198 Daltonics). The peptides (200ng) were separated on an IonOpticks column (25cm X
1199 75µm 1.6µm C18 resin) using a gradient of 2-37% B (2%ACN, 0.1%FA) in 100 minutes
1200 at a flow rate of 0.3 µl/min. The dual TIMS had a ramp time and accumulation time of
1201 166 ms resulting in a total cycle time of 1.89s. Data was acquired in Data Dependent
1202 Acquisition-Parallel Accumulation Serial Fragmentation (DDA-PASEF) mode with 10
1203 PASEF scans in a mass range from 100 m/z to 1700 m/z. The ion mobility scan range
1204 was fixed from 0.7-1.25 Vs/cm^2. All samples were injected using a randomized injection
1205 sequence. To minimize carry-over, one solvent blank injection was performed after
1206 each sample.
1207
1208 *Data interpretation*
1209 Raw files were converted to .mgf peaklists using DataAnalysis (version 5.3, Bruker
1210 Daltonics) and were submitted to Mascot database searches (version 2.5.1,
1211 MatrixScience, London, UK) against a *Danio rerio* protein sequence database
1212 downloaded from UniProtKB-SwissProt (2022_05_18, 61 732 entries, taxonomy ID:
1213 7955), to which common contaminants and decoy sequences were added. Spectra
1214 were searched with a mass tolerance of 15 ppm in MS mode and 0.05 Da in MS/MS
1215 mode. One trypsin missed cleavage was tolerated. Carbamidomethylation of cysteine
1216 residues was set as a fixed modification. Oxidation of methionine residues and
1217 acetylation of proteins' n-termini were set as variable modifications. Identification
1218 results were imported into the Proline software (version 2.1.2,
1219 http://proline.profiproteomics.fr) (Bouyssié et al., 2020) for validation. Peptide
1220 Spectrum Matches (PSM) with pretty ranks equal to one were retained. False
1221 Discovery Rate (FDR) was then optimized to be below 1% at PSM level using Mascot
1222 Adjusted E-value and below 1% at protein level using Mascot Mudpit score. For label
1223 free quantification, peptide abundances were extracted without cross assignment

1224 between the samples. Protein abundances were computed using the sum of the unique
1225 peptide abundances normalized at the peptide level using the median.
1226 To be considered, proteins must be identified in at least four out of the five replicates
1227 in at least one condition. Imputation of the missing values and differential data analysis
1228 were performed using the open-source ProStaR software (Wieczorek et al., 2017).
1229 Imputation of missing values was done using the approximation of the lower limit of
1230 quantification by the 2.5% lower quantile of each replicate intensity distribution ("det
1231 quantile"). A Limma moderated *t*-test was applied on the dataset to perform differential
1232 analysis. The adaptive Benjamini-Hochberg procedure was applied to adjust the p-
1233 values and FDR. The mass spectrometry proteomics data have been deposited to the
1234 ProteomeXchange Consortium via the PRIDE partner repository (Perez-Riverol et al.,
1235 2022), with the dataset identifier PXD042283.
1236
1237 ***Embryos drug treatment***
1238 27 hpf embryos from *dnaaf1*$^{tm317b/+}$ incross were dechorionated manually. N-acetyl
1239 cysteine ethyl ester (NACET) (BIOLLA Chemicals #59587-09-6) was prepared
1240 extemporaneously at the final concentration of 3 mM in pure water (pH: 7.2;
1241 conductivity 650 µS). Embryos were treated between 27 hpf to 60 hpf and embryos
1242 were anesthetized before being imaged laterally.
1243
1244 ***Juvenile drug treatment and preparation of treated samples***
1245 Two hundred larvae were housed off-system in 1.8 liter tanks with 20 fish per tank,
1246 being fed twice a day throughout the experiment. 100 were treated with NACET
1247 (BIOLLA Chemicals #59587-09-6), which was prepared extemporaneously at 1.5 mM
1248 (286.5mg/L) in fish water (pH 7.2, Conductivity 650 µS) which was changed once per
1249 day. Fish were treated from 30 dpf to 84 dpf and monitored for curvature onset once
1250 per week. At 85 dpf, fish were euthanized, imaged to measure the curvature index.
1251 Half of the fish were fixed for histology analysis in zamboni fixative [35 ml PFA 4 %, 15
1252 ml saturated picric acid (1.2 %)] overnight at 4°C under agitation, while the other half
1253 was processed for RT-qPCR analysis. To prepare dorsal trunk RNA, internal organs
1254 were removed in cold PBS 1X, and the remaining tissue was cut in small pieces before
1255 lysis in QIAzol (QIAGEN). Homogenization was achieved using plunger pistons and
1256 passages through 1ml syringes.

1257

1258 ***Transgenesis***

1259 The *Tol2 -5.2foxj1a:5xmyc-RPGRIP1L* plasmid was produced using the Gateway
1260 system by combining four plasmids. P5E-foxj1a enhancer was kindly donated by [3].
1261 5xmyc-RPGRIP1L cDNA was amplified from the plasmid pCS2-5xmyc-RPGRIP1L
1262 (Mahuzier et al., 2012) using CloneAmp HiFi PCR Premix (Takara # 639298) using
1263 primers : forward 5'-
1264 GGGGACAAGTTTGTACAAAAAGCAGGCTGCAGGATCCCATCGATTTAAAGCT-3'
1265 and reverse 5'
1266 GGGGACCACTTTGTACAAGAAAGCTGGGTCTCCGAGCTCGGTTCAAGCCTCCA
1267 AGTCATCTCTGT-3. The PCR product was gel purified using QIAEX II gel extraction
1268 kit (QIAGEN, #20021) . BP recombination (Invitrogren "Gateway BP Clonase II
1269 Enzyme Mix" #11789-020) was performed into pDONR221 #218 to generate pMe-
1270 5xmyc-RPGRIP1L. The 3' entry polyadenylation signal plasmid was the one described
1271 in [61]. The 3 plasmids were shuttled into the backbone containing the cmcl2:GFP
1272 selection cassette (Kwan et al., 2007) using the LR recombination (Invitrogen
1273 "Gateway LR Clonase II Plus Enzyme Mix" #12538-120). *rpgrip1l*$^{+/-}$ X AB embryos
1274 outcrosses were injected at the one cell stage with 1nl of a mix containing 20 ng/µl
1275 plasmid and 25 ng/µl Tol2 transposase RNA and screened at 48 hpf for GFP
1276 expression in the heart. Some F0 founders produced F1 zebrafish carrying one copy
1277 of the transgene that were further checked for RPGRIP1L specific expression in *foxj1a*
1278 territory, using Myc labelling at the base of FP cilia in 2,5 dpf embryos.

1279 The Tol2-1.7kb col2a1a:5xMyc-RPGRIP1L plasmid was produced using the Gateway
1280 System by combining four plasmids. Col2a1a enhancer was amplified from the plasmid
1281 -1.7kbcol2a1a:EGFP-CAAX (Dale and Topczewski, 2011) using CloneAmp HiFi
1282 premix (Takara #639298) with the primers: forward 5'-GGG GAC AAC TTT GTA TAG
1283 AAA AGT TGG CCC TCT GAC ACC TGA TGC CAA TTG C-3' and reverse 5'-GGG
1284 GAC TGC TTT TTT GTA CAA ACT TGC TTG CAG GTC CTA AGG GGT GAA AGT
1285 CG-. The PCR product was gel purified and BP recombination was performed into
1286 pDONR_P4-P1R-#219. The middle entry plasmid and the 3' plasmid were the same
1287 as those used to generate the Tol-5.2foxj1a: 5xmyc-RPGRIP1L plasmid. F1 transgenic
1288 were first selected for GFP expression in the heart and then on Myc labelling within
1289 notochordal cells at 2,5 dpf within their embryonic progeny.

1290

1291 ***Skeletal preparations, Alizarin staining and imaging***

1292 Animals were euthanized using a lethal concentration of MS222 (0.28 mg/mL), skin
1293 was removed and fixation was performed with 4% paraformaldehyde overnight at 4°C.
1294 After evisceration, samples were incubated in borax 5%, rinsed several times in 1%
1295 KOH and incubated in solution composed with Alizarin 0.01% (Sigma, A5533) and
1296 KOH 1% during 2 days. Fish were rinsed several times in KOH 1% and incubated in
1297 trypsin 1% and borax 2% for 2 days until cleared. Samples were rinsed several times
1298 in distilled water and transferred in glycerol 80% (in KOH 1%) using progressive
1299 dilutions. Samples were kept in glycerol 80% until imaging.

1300

1301 ***Cobb angles measurements***

1302 To quantitatively evaluate the severity of spine curvature in *rpgrip1l*$^{+/-}$; *urp2*$^{+/-}$
1303 incrosses, we used the zebrafish skeletal preparations stained with Alizarin. We drew
1304 parallel lines to the top and bottom most displaced vertebrae on lateral and dorsal
1305 views. The Cobb angle was then measured as the angle of intersection between lines
1306 drawn perpendicular to the original 2 lines. This was conducted using FIJI software.
1307 For each fish, the total Cobb angle was calculated by summing all Cobb angles.

1308

1309 ***Curvature index measurements***

1310 We implemented a novel procedure to quantify curvatures on both axes by drawing a
1311 line along the body of the fish as shown in Figure supplementary 4I and curvature was
1312 calculated in MATLAB (code available on demand). We decomposed the line in a
1313 series of equidistant points and we measured the curvature at each of these points
1314 using the LineCurvature2D function. We then added the absolute values of these
1315 measures, which are expressed as an angle (in radian) per unit of length. The higher
1316 the sum is for a given line, the more this line is curvated. We verified the accurancy of
1317 this metric by comparing it with the visual assessment of curvatures by 3 independent
1318 observers. For *rpgrip1l*$^{+/-}$; *urp2*$^{+/-}$ incross and NACET experiment, a line following the
1319 body deformation was drawn from the mouth to the base of the tail following the midline
1320 of the fish in lateral position and another one along the dorsal axis. Curvature index of
1321 both curves were summed for each fish. Curvature analysis was performed blinded to
1322 fish genotype. *rpgri1l*$^{+/+}$ or *rpgrip1l*$^{+/-}$ siblings were used as controls.

1323

1324 ***Data acquisition for body-curvature analysis at embryonic stage***

1325 Zebrafish embryos were anesthetized and imaged laterally with the head pointing to
1326 the left. The angle between the line connecting the center of the eye to the center of
1327 the yolk and the line connecting the center of the yolk to the tip of the tail was measured
1328 to evaluate the body curvature of the embryos. For quantitative analysis, the angles of
1329 each embryo were put in the same concentric circles represented with a Roseplot, with
1330 0° pointing to the right and 90° pointing to the top. Each triangle represents a 30°
1331 quadrant, and its height indicates the number of embryos within the same quadrant.

1332

1333 ***Quantification, statistical analysis and figure preparation***

1334 For all experiments the number of samples analyzed is indicated in the text and/or
1335 visible in the figures. Statistical analysis was performed using the Prism software. ****:
1336 P value < 0.0001; ***: P value < 0.001; **: P value < 0.01; *: P value < 0.05. Graph
1337 were made using Prism and Matlab and figures were assembled using Photoshop
1338 software.

1339

1340 **REAGENT AND RESOURCE TABLE**

Reagent type or resource	Designation	Source or reference	Identifiers	Additional Infos
Antibody (antiserum)	Rabbit polyclonal IgG anti-bovine Reissner Fiber	Didier et al 1995	Courtesy of Dr. S.Gobron	1:200
Antibody	Mouse monoclonal	Thermofisher	#33-9100	1:150

	IgG1k anti ZO1 -1A12			
Antibody	Mouse monoclonal IgG2b anti-acetylated-tubulin (clone 6-11B-1)	Sigma-Aldrich	#T 6793 RRID: AB_477585	1:400
Antibody	Mouse monoclonal IgG1 anti glutamylated Tubulin	Adipogen	#AG-20B-0020-C100	1:500
Antibody	Rabbit polyclonal anti-Arl13b	Proteintech	#17711-1-AP	1:200
Antibody	Mouse monoclonal IgG1 anti-GFAP	Sigma	#G3893	1:400
Antibody	Chicken monoclonal IgY anti-GFP	AVES lab	#GFP-1020	1:200
Antibody	Mouse monoclonal IgG2a anti-myc (clone 9b11)	Cell signaling	#2276	1:200

Antibody	Rabbit polyclonal anti-LCP1	GeneTex	#GTX124420	1:200
Antibody	Mouse monoclonal IgG1 anti-gamma-tubulin	Sigma	#T6557	1:500
Antibody	Mouse polyclonal anti-annexin A2	Proteintech	#11256-1-AP	1:200
Antibody	Goat anti-mouse IgG1 Alexa633	Molecular probes	# A-21126 RRID:AB_2535768	1:400
Antibody	Goat anti-mouse IgG1 Alexa568	Molecular Probes	# A-21124 RRID: AB_2535766	1:400
Antibody	Goat anti-mouse IgG2a Alexa568	Molecular probes	# A-21134 RRID:AB_2535773	1:400
Antibody	Goat anti-mouse IgG2a Alexa488	Molecular probes	# A-21131 RRID:AB_141618	1:400
Antibody	Goat anti-mouse IgG2b Alexa633	Molecular probes	# A-21146 RRID:AB_2535782	1:400

Antibody	Goat anti-mouse IgG2b Alexa568	Molecular probes	# A-21144 RRID: AB_2535780	1:400
Antibody	Goat anti-rabbit IgG Alexa568	Molecular probes	# A-11011 RRID:AB_143157	1:400
Antibody	Goat anti-rabbit IgG Alexa488	Molecular probes	# A-11008 RRID: AB_143165	1:400
Antibody	FITC donkey Anti-Chicken IgY	Jackson ImmunoResearch	# 703-096-155	1:200
Chemical	Vectashield	Vector Laboratories	H-1000	
Strain (Danio rerio)	zebrafish wild-type AB or (TL x AB) hybrid strains	N/A	N/A	
Strain (Danio rerio)	Zebrafish *rpgrip1l*$^{\Delta}$ mutant strain	This manuscript, Zfin:*rpgrip1l* ^{bps1}		
Strain (Danio rerio)	Zebrafish *rpgrip1l*^{ex4} mutant strain	This manuscript, Zfin:*rpgrip1l* ^{bps2}		
Strain (Danio rerio)	Zebrafish *urp2*$^{+/-}$	(Gaillard et al., 2023)	ZDB-ALT-230207-5	

Strain (Danio rerio)	Zebrafish *dnaaf1*$^{tm317b/+}$	(van Rooijen et al., 2008)		
Strain (Danio rerio)	Zebrafish Scospondin-GFP^{ut24}	(Troutwine et al., 2020)		
Recomb. DNA	Foxj1 promoter-enhancer sequence	(Dale and Topczewski, 2011)		
Software	LASX	Leica		
Software	Amira for Life & Biomedical Sciences	Thermo Fisher Scientific		
Software	CRISPOR	(Haeussler et al., 2016)	http://crispor.tefor.net/	
Software	Fiji/ImageJ	(Schindelin et al., 2012)	https://imagej.net/Fiji/Downloads	
Software	PRISM	GraphPad	https://www.graphpad.com/	
Software	Metascape		https://metascape.org/gp/index.html#/main/step1	
Software	Matlab	The Mathworks, Inc.	https://fr.mathworks.com/products/matlab.html	
Software	NRecon reconstruction software	Micro Photonics Inc.		

Software	CTvox	Bruker		
Software	CT Analysis	Bruker		
Other				
Refractometer	Roth Sochiel EURL	DR 301-95		
Confocal microscope	Leica	SP5		
Confocal microscope	Zeiss	LSM 980 Inverted		
Confocal microscope	Zeiss	LSM 710		
Macroscope	Zeiss	AXIOZOOM V16		
Micro-scanner	Bruker	Skyscan 1272		
Microtome	Leica	RM2125RT		
Q-PCR apparatus	Applied Biosystems	Step One plus		

1349 **FIGURE LEGENDS**

1350

1351 **Figure 1: *rpgrip1l*$^{-/-}$ juvenile fish develop scoliosis, which is rescued by**
1352 **RPGRIP1L expression in *foxj1a*-positive cells.**

1353 **(A)** Representative *rpgrip1l*$^{-/-}$ fish at 5 days post-fertilization (dpf) (4 mm body length,
1354 larvae), 5 weeks pf (wpf) (1.2 cm body length, juveniles) and 12 wpf (2.5 cm body
1355 length, adults), showing absence of morphological defects in embryos, onset of spine
1356 curvature (tail-up) in juveniles and scoliosis in adults. (**B-C)** Graph showing the time
1357 course of scoliosis appearance **(B)** in *rpgrip1l*$^{-/+}$ incrosses (total 4 clutches, 252 fish)
1358 and scoliosis penetrance **(C)** in adults. (**D-E**) Micro-computed tomography (µCT) scans
1359 of control siblings (D) and *rpgrip1l*$^{-/-}$ (E) adult fish. 4 fish were analyzed for each
1360 condition. (**F-G)** Dorsal and lateral superimposed µCT views of the spines of one
1361 control (yellow) and two *rpgrip1l*$^{-/-}$ (pink, cyan) adult fish illustrating the 3D spine
1362 curvatures in mutants. **(H)** Schematic representation of the two rescue constructs. **(I)**
1363 Table presenting the number and phenotype of *rpgrip1l*$^{-/-}$ fish generated for both rescue
1364 experiments by stable transgenesis ***(*J)** Graph representing scoliosis penetrance in
1365 transgenic and non-transgenic *rpgrip1l*$^{-/-}$ siblings.

1366

1367 **Figure 2 Altered ciliogenesis at trunk and subcommissural organ (SCO) levels.**

1368 (**A-C'''**) Immunostaining of trunk sagittal sections at the level of the spinal cord central
1369 canal in *rpgrip1l*$^{+/+}$ (A-A'''; n=5), straight *rpgrip1l*$^{-/-}$ (B-B'''; n=4) and scoliotic *rpgrip1l*$^{-/-}$
1370 fish (C-C'''; n=6)) at 8 weeks (N=2 independent experiments). Cilia were
1371 immunostained with Arl13b (cyan, A'', B'', C'') and glutamylated-tubulin (magenta, A''',
1372 B''', C'''). Panels A-C' are merged images with DAPI. Panels A', B' and C' show higher
1373 magnification of the squared regions in A, B and C, respectively. Scale bars: 10 µm in
1374 A, 5 µm in A'. **(D)** Violin plot showing the distribution of cilia length along the central
1375 canal of *rpgrip1l*$^{+/+}$ (n=300 cilia from 5 fish), straight *rpgrip1l*$^{-/-}$ (n=267 from 4 fish) and
1376 scoliotic *rpgrip1l*$^{-/-}$ (n=414 from 6 fish) juvenile fish (N=2). **(E)** Violin plot showing the
1377 distribution of cilia density along the central canal of juvenile *rpgrip1l*$^{+/+}$ (n=5), straight
1378 *rpgrip1l*$^{-/-}$ (n=4) and scoliotic *rpgrip1l*$^{-/-}$ fish (n=6, N=2). Density is the average number
1379 of ventral and dorsal cilia lining the CC over a length of 100 µm from 3 to 5 sections for
1380 each fish. Each dot represents the mean cilia length (D) or cilia density (E) of 4-8

1381 sections analyzed at different antero-posterior levels. Statistical analysis was
1382 performed using Tukey's multiple comparisons test where * means P-value < 0.05, and
1383 ** means P-value < 0.01. **(F)** Violin plot showing the distribution of width of the central
1384 canal (nuclear-free region) (in µm) of juvenile *rpgrip1l*$^{+/+}$ (n=5), straight *rpgrip1l*$^{-/-}$ (n=4)
1385 and scoliotic *rpgrip1l*$^{-/-}$ fish (n=6, N=2). Each dot represents the mean of 3
1386 measurements made at different AP levels. Statistical analysis was performed using
1387 Tukey's multiple comparisons test where ns means non-significant, * means P-value <
1388 0.05. **(G-L)** Immunostaining of cilia on transverse sections of the brain at SCO level
1389 using glutamylated-tubulin and acetylated-tubulin antibodies (both in white), in
1390 *rpgrip1l*$^{+/+}$ (n=6) (G, G', H), straight *rpgrip1l*$^{-/-}$ (n=3) (I, I', J) and scoliotic *rpgrip1l*$^{-/-}$ (n=7)
1391 (K, K', L) 8 wpf fish (N=2). Nuclei are stained with DAPI (blue). G', I' and K' are higher
1392 magnifications of squared regions in G, I and K, respectively. In H, J and L the bottom-
1393 right inset represents a higher magnification of the squared region. Scale bars in G and
1394 G': 10 µm.
1395

1396 **Figure 3: *rpgrip1* $^{-/-}$ juveniles show ventricular dilations and loss of the Reissner**
1397 **Fiber at scoliosis onset.**

1398 (A) Reconstruction of the RhV at the level of posterior midbrain and hindbrain in a
1399 transparised 5 wpf control zebrafish brain, stained with ZO1 antibody (ventricular
1400 surface) and DiI (global brain shape). Several brain regions are annotated on the
1401 reconstruction where Tel means telencephalon, ChP forebrain choroid plexus, SCO
1402 subcommissural organ, TeO optic tectum, CCe corpus cerebelli, CC crista cerebellaris
1403 and Rh rhombencephalon. **(B-D)** Cyan circles represent the ROIs measured in F. The
1404 orange line in D indicates the level of optical sections in E. **(E)** Optical transverse
1405 sections showing the caudal part of reconstructed ventricles of a control and two
1406 *rpgrip1l*$^{-/-}$ fish, one straight and two tail-up. **(F)** Graphs of the ventricle volume at the
1407 onset of scoliosis in 3 control and 4 *rpgrip1l*$^{-/-}$ (one straight and three tail-up) fish. The
1408 green dot corresponds to the straight mutant fish. Each dot represents a fish. Statistical
1409 analysis was performed using unpaired t-test where ns means non-significant, and *
1410 means P-value < 0.05. **(G)** Graph of the surface of the optical sections as illustrated in
1411 E. The green dot corresponds to a straight mutant fish. Each dot represents a fish.
1412 Statistical analysis was performed using unpaired t-test where ns means non-
1413 significant, and * means P-value < 0.05. **(H)** Schematic representation of a portion of

1414 the spinal cord central canal in a lateral view of the fish trunk, showing the Reissner
1415 Fiber (RF), and of the SCO in a transverse view of the brain at the level of diencephalic
1416 Ventricle (DiV). **(I-Q)** Visualization of the GFP fluorescence in the *sspo-GFP*$^{uts24/+}$
1417 transgenic line (fire LUT) in sagittal sections of the trunk (I-K) (N=3) and transverse
1418 sections of the brain at the level of the SCO (N=2) (L-Q) in juvenile fish. The
1419 corresponding fish are 8 wpf *rpgrip1l*$^{+/+}$ (I, L, O) (n=10); straight *rpgrip1l*$^{-/-}$ (J, M, P)
1420 (n=9) and scoliotic *rpgrip1l*$^{-/-}$ (K, N, Q) (n=8). L-N and O-Q show sections at anterior
1421 and posterior SCO levels, respectively. Scale bars: 5 µm in I-K, 10 µm in L-Q.
1422

1423 **Figure 4: Upregulation of *urp1/2* expression does not contribute to axis**
1424 **curvature of *rpgrip1l*$^{-/-}$ fish**.

1425 **(A)** Quantitative reverse transcription polymerase chain reaction (qRT-PCR) assaying
1426 *urp2* expression level in *rpgrip1l*$^{-/-}$ and *rpgrip1l*$^{+/+}$ (WT) siblings. Each dot represents
1427 the value obtained for one fish. Green and purple dots represent straight and scoliotic
1428 *rpgrip1l*$^{-/-}$ fish, respectively. qRT-PCR analysis was performed at 5 wpf (juvenile stage,
1429 5 controls and 7 *rpgrip1l*$^{-/-}$) and 12 wpf (adult stage, 5 controls and 9 *rpgrip1l*$^{-/-}$). *urp2*
1430 expression levels are increased by approximately 3.5-fold in *rpgrip1l*$^{-/-}$ at both stages.
1431 Statistical analysis was performed using unpaired t-test where **P < 0.01. Error bars
1432 represent s.d. **(B)** Quantification of body axis curvature from dorsal and lateral views
1433 in 4 mpf fish issued from [*rpgrip1l*$^{+/-}$, *urp2*$^{+/-}$] incrosses. Each point represents the value
1434 measured for one fish. Statistical analysis was performed using Tukey's multiple
1435 comparisons test where **** P < 0,0001 with error bars represent s.d. n=9 [*rpgrip1l*$^{+/+}$*;*
1436 *urp2*$^{+/+}$], 7 [*rpgrip1l*$^{+/+}$*; urp2*$^{-/-}$], 27 [*rpgrip1l*$^{-/-}$*; urp2*$^{+/+}$], 48 [*rpgrip1l*$^{-/-}$*; urp2*$^{+/-}$] and 27
1437 [*rpgrip1l*$^{-/-}$*; urp2*$^{-/-}$] fish. **(C)** Representative [*rpgrip1l*$^{-/-}$*; urp2*$^{+/+}$] and sibling [*rpgrip1l*$^{-/-}$*;*
1438 *urp2*$^{-/-}$] fish on lateral and dorsal views at 12 wpf. Scale bar 5mm. **(D, E)** Expression
1439 levels of *urp2* (D) and *urp1* (E) in adult fish (12 wpf). Each dot represents the value for
1440 one fish. Green and purple dots represent straight and scoliotic *rpgrip1l*$^{-/-}$ fish,
1441 respectively (n=5 [*rpgrip1l*$^{+/+}$*; urp2*$^{+/+}$], 9 [*rpgrip1l*$^{+/+}$*; urp2*$^{-/-}$], 11 [*rpgrip1l*$^{-/-}$*; urp2*$^{+/-}$] and
1442 10 [*rpgrip1l*$^{-/-}$*; urp2*$^{-/-}$]). Each gene expression level is compared to the *lsm12b*
1443 housekeeping gene. Statistical analysis was performed using Tukey's multiple
1444 comparisons test where ns means non-significant and ** P < 0.01, **** P < 0.0001.
1445 Error bars represent s.d.
1446

1447 **Figure 5: Comparative transcriptome and proteome analysis of control and**
1448 ***rpgrip1l*$^{-/-}$ fish.**

1449 **(A-B)** Volcano-plots showing differentially regulated genes in the transcriptomes of the
1450 brain (A) and dorsal trunk (B) comparing 5 controls (2 wt, 3 *rpgrip1l*$^{-/+}$) and 7 *rpgrip1l*$^{-/-}$
1451 (6 tail-up and 1 straight) fish at 5 wpf (0.9 cm body length). Each dot corresponds to
1452 one gene. A gene was considered deregulated if its associated P-adj. value was
1453 inferior to 0,05. Red and blue dots represent up-regulated (Log2FC > 0.75), and down-
1454 regulated (Log2FC < -0.75) genes, respectively. The names of the top 25 most
1455 deregulated genes are boxed. **(C)** GO term analysis of biological processes in the brain
1456 samples using Metascape. **(D)** Venn diagram of the upregulated genes in brain and
1457 trunk samples, showing many common genes between the two regions. **(E)** Selected
1458 genes of interest upregulated in the trunk and/or brain of *rpgrip1l*$^{-/-}$ fish. The four genes
1459 in red were also found upregulated in the proteome of adult *rpgrip1l*$^{-/-}$ fish. **(F)** Volcano-
1460 plot showing differentially expressed proteins in the brain of 5 *rpgrip1l*$^{+/+}$ fish versus 5
1461 *rpgrip1l*$^{-/-}$ adult scoliotic fish (3 months pf). Each dot corresponds to one protein. A
1462 protein was considered differentially expressed if its associated P-adj. value was
1463 inferior to 0.05. Red and blue dots represent proteins enriched (Log2FC > 0.75) or
1464 depleted (Log2FC < -0.75) in mutant brains, respectively. The names of the top 25
1465 most differentially expressed proteins are boxed.
1466

1467 **Figure 6: Anxa2 and GFAP upregulation and increased number of LCP1-positive**
1468 **cells around CNS ventricles of *rpgrip1l*$^{-/-}$ juvenile fish at scoliosis onset.**

1469 **(A-D')** Immunostaining for GFAP (A, B, C, D) and Anxa2 (A', B', C', D') on adult brain
1470 transverse sections at DiV (A-B') and RhV (cerebellar) (C-D') levels in controls (A, A',
1471 C, C') (n=3) and *rpgrip1l*$^{-/-}$ scoliotic (B, B', D, D') (n=4) fish. In A-D, nuclei are stained
1472 with DAPI (blue). White stars indicate the SCO, white triangles point to the ventral RhV
1473 region. Open arrows point to a long cellular process co-labelled by Anxa2 and GFAP.
1474 **(E-L)** Immunostaining for GFAP (magenta) on transverse sections of the brain at SCO
1475 (E-H) and RhV (I-L) levels in controls (E, I) (n=4), straight *rpgrip1l*$^{-/-}$ (F, G, J, K) (n=4)
1476 and scoliotic *rpgrip1l*$^{-/-}$ (H, L) (n=3) juvenile (8 wpf) fish. Nuclei are stained with DAPI
1477 (white). Scale bar: 125µM for A-D', 20 µm for E-H and 100 µm for I-L. **(M)** Graph
1478 representing the percentage of GFAP-positive cells among the total number of SCO
1479 cells in control (n=4), straight *rpgrip1l*$^{-/-}$ (n=4), and scoliotic *rpgrip1l*$^{-/-}$ (n=3) fish at

1480 scoliosis onset (N=1). Each dot represents the mean ratio of GFAP-positive over
1481 negative cells in 3-6 sections per fish. Green dots correspond to fish with no or very
1482 low percentage of GFAP+ cells, red dots to fish with a high percentage of GFAP+ cells.
1483 Statistical analysis was performed with Tukey's multiple comparisons test where ns
1484 means non-significant, ** means P-value < 0.01 and *** P-value < 0.001. Error bars
1485 represent s.d. “str”: straight; “sco”: scoliotic. **(N-Q’)** Immunostaining for LCP1+
1486 microglia/macrophages (magenta) on brain transverse sections at SCO levels in a
1487 rectangle of 100 µm x 60 µm located under the posterior commissure in controls (n=4)
1488 (N, N’), straight *rpgrip1l*$^{-/-}$ (n=4) (O-P’) and *rpgrip1l*$^{-/-}$ at scoliosis onset (n=3) (Q, Q’) 8
1489 wpf fish (N=1). Nuclei are stained with DAPI (white). Scale bar: 20 µm. **(R)**
1490 Quantification of LCP1+ cell density around the SCO in controls (n=4), straight *rpgrip1l*$^{-}$
1491 $^{/-}$ (n=4) and scoliotic *rpgrip1l*$^{-/-}$ (n=3) at 8 wpf. 23 sections were counted for control, 21
1492 sections for *rpgrip1l*$^{-/-}$ straight and 18 sections for *rpgrip1l*$^{-/-}$ scoliotic fish. Each dot
1493 represents the mean value for one fish. Green dots correspond to the fish without any
1494 GFAP+ SCO cells, red dots correspond to the fish with GFAP+ SCO cells (SCO cells
1495 are defined as the dorsal cells located underneath the posterior commissure and above
1496 the diencephalic ventricle). Note that straight *rpgrip1l*$^{-/-}$ fish with GFAP+ SCO cells
1497 present a higher number of LCP1+ cells. Statistical analysis was performed with
1498 Tukey's multiple comparisons test where ns means non-significant. Error bars
1499 represent s.e.m. “str”: straight “sco”: scoliotic.
1500

1501 **Figure 7: NACET treatment reduces scoliosis penetrance and severity in**
1502 ***rpgrip1l*$^{-/-}$ and decreases astrogliosis and LCP1+ cell number at SCO level.**

1503 **(A)** Kinetics of scoliosis development in *rpgrip1l*$^{+/-}$ incrosses in the presence (n=150
1504 fish) or absence (n=174 fish) of NACET treatment (1.5 mM) from 4 to 12 weeks (N=1).
1505 “str”: straight; “sco”: scoliotic. **(B)** Quantification of body axis curvature from dorsal and
1506 lateral views at 13 wpf, at the end of the NACET treatment. Each dot corresponds to
1507 one fish. Among the 174 fish raised in untreated condition, we measured 18 controls
1508 (*rpgrip1l*$^{\pm/-}$) and 33 *rpgrip1l*$^{-/-}$, and upon NACET treatment, 16 controls (*rpgrip1l*$^{\pm/+}$) and
1509 23 *rpgrip1l*$^{-/-}$. *rpgrip1l*$^{\pm/-}$ represents a pool of *rpgrip1l*$^{+/+}$ and *rpgrip1l*$^{+/-}$. Error bars
1510 represent s.d. **(C)** Representative pictures of *rpgrip1l*$^{-/-}$ fish with their curvature index
1511 without or after NACET treatment, at 13 wpf. Scale bar is 0,5 cm. Left panels
1512 correspond to an untreated *rpgrip1l*$^{-/-}$ scoliotic fish on lateral (upper) and dorsal (lower)

1513 views. Middle panels represent treated *rpgrip1l*$^{-/-,}$ with a lower curvature index than
1514 scoliotic fish on lateral (upper) and dorsal (lower) views and right panels are pictures
1515 of rescued straight *rpgrip1l*$^{-/-}$ fish on lateral (upper) and dorsal (lower) views. **(D)** Graph
1516 representing the number of LCP1+ cells in wt (n=3), untreated *rpgrip1l*$^{-/-}$ (n=3) and
1517 NACET-treated *rgprip1l*$^{-/-}$ (n=3) fish in the SCO region (N=1). **(E)** Immunostaining for
1518 GFAP (green), Acetylated tubulin (white) and LCP1 (red) on adult brain transverse
1519 sections at SCO level in untreated (upper panels) and NACET-treated (lower panels)
1520 fish. Nuclei are stained with DAPI (blue). No GFAP staining was present in controls
1521 (n=3) (upper left), while untreated mutants displayed strong GFAP labeling (upper
1522 right) (n=3). NACET treatment totally suppressed gliosis in a straight *rpgrip1l*$^{-/-}$ fish
1523 (lower right panel) (n=1) and diminished the intensity of GFAP labeling in slightly tail-
1524 up *rpgrip1l*$^{-/-}$ (n=2). Scale bar: 12,5 µm. **(F)** Graph presenting the percentage of GFAP-
1525 positive cells among the total number of SCO secretory cells compared between
1526 controls (n=3), untreated *rpgrip1l*$^{-/-}$ (n=3), and NACET treated *rpgrip1l*$^{-/-}$ adult fish (n=3)
1527 (N=1). Each dot represents the mean of % of GFAP-positive cells present in 3-6
1528 sections per fish. Statistical analysis was performed using Tukey's multiple
1529 comparisons test where * means P-value <0.05 and **** means P-value < 0.0001.
1530

1531 **Figure 8: Altered ciliogenesis, GFAP upregulation and increased number of**
1532 **LCP1-positive cells around ventricles of *cep290* $^{-/-}$ juvenile fish at 4 wpf.**

1533 **(A-F')** Immunostaining of the cilia marker glutamylated tubulin (white) on 4 wpf brain
1534 transverse sections at 3 antero-posterior SCO levels in 4 wpf control (A-C', n=3) and
1535 *cep290*$^{-/-}$ scoliotic (D-F', n=3) fish. Nuclei are stained with DAPI (blue). White stars
1536 indicate the diencephalic ventricle (DiV), above which lies the SCO. White rectangles
1537 in C and F delineate the close-up on cilia (C', F'). Scale bar: 10 µm for A-F, 2,5 µm for
1538 C'-F'. **(G-L)** Immunostaining for Acetylated Tubulin (G, J), GFAP (H, K) and LCP1 (I,
1539 L) on transverse sections of the brain at SCO level in controls (G-I) (n=3), and *cep290*$^{-}$
1540 $^{/-}$ (J-L) (n=3) juvenile (4 wpf) fish. In G and J, nuclei are stained with DAPI (blue). Scale
1541 bar: identical to A-F. **(M)** Graph representing the percentage of GFAP-positive cells
1542 among the total number of SCO secretory cells in control (n=3) and scoliotic *cep290* $^{-/-}$
1543 (n=3) fish at scoliosis onset (N=1). Each dot represents the mean ratio of GFAP-
1544 positive over total SCO secretory cells in 5-7 sections per fish. **(N)** Quantification of
1545 LCP1+ cell density around the SCO in controls (n=3) and curved *cep290*$^{-/-}$ (n=3) fish

1546 at 4 wpf. 16 sections were counted for control, 18 sections for *cep290*$^{-/-}$ scoliotic fish.
1547 Each dot represents the mean value for one fish. Statistical analysis was performed
1548 with unpaired T test where * means P-value < 0.05. Error bars represent s.d. **(O-V)**
1549 Immunostaining for GFAP (white) on brain transverse sections at cerebellum levels (P,
1550 R) and anterior hindbrain level (T, V) in control (P, T) (n=3), and *cep290*$^{-/-}$ (R, V) (n=3)
1551 fish. Corresponding nuclear staining (DAPI in white) is shown above (O, Q, S, U). Scale
1552 bar: 125 µm.
1553

SUPPLEMENTARY FIGURE LEGENDS

Supplementary figure S1: Production and characterization of the *rpgrip1*$^{\Delta}$ and *rpgrip1l*^{ex4} fish lines.

(A) Schematic exon-intron structure of the *Danio rerio rpgrip1l* gene. Two alleles were produced by CRISPR/cas9-mediated genome engineering, *rpgrip1l*^{ex4}*(rpgrip1l*^{bps2} *in ZFIN)* with a nonsense mutation in exon 4 and *rpgrip1l*$^{\Delta 4\text{-}25}$ (*(rpgrip1l*^{bps1} *in ZFIN)* also called *rpgrip1l*$^{\Delta}$ or *rpgrip1l*$^{-}$) with a large deletion between exons 4 and 25, encompassing most of the protein coding sequence. Both alleles had identical embryonic phenotype (panel B and data not shown). (A') Electrophoresis gel showing the migration profile of amplicons for each genotype, *rpgrip1l*$^{\Delta/\Delta}$, *rpgrip1l*$^{\Delta/+}$, *rpgrip1*$^{+l/+}$ produced by triplex PCR (B) Absence of laterality defects and kidney cysts in *rpgrip1l*$^{\Delta/\Delta}$ and *rpgrip1l*$^{ex4/ex4}$ embryos. **(C)** Immunostaining on whole 30 hpf control (left panels) and *rpgrip1l*$^{-/-}$ (right panels) embryos to visualize the RF (anti-RF antibody, middle panels) and cilia (acetylated tubulin antibody, lower panels) in the caudal region. Nuclei (upper panels) are stained with DAPI. The RF is present in the central canal of *rpgrip1l*$^{-/-}$ embryos, as well as cilia in the whole neural tube width. Scale bar: 6 µm for upper panels; 15 µm for lower panels. **(D-E)** Absence of retinal morphological defects in 5 dpf *rpgrip1l*$^{-/-}$ larvae. Retinal sections of control (D) and *rpgrip1l*$^{-/-}$ (E) larvae were immunostained with Zpr3 (red) to label the external segment of photoreceptors and Acetylated Tubulin (Ac Tub) (green) to label axonemes. D' and E' are insets in D and E focusing on the photoreceptor layer. Scale bar: 50 µm. (**F-H'''**) Scanning electron microscopy of brain ventricles in control (F-F''), straight (str.) *rpgrip1l*$^{-/-}$ (G-G'') and scoliotic (sco.) *rpgrip1l*$^{-/-}$ (H-H''') adult (3 months) fish. Ependymal multiciliated cells of the rhombencephalic ventricle (RhV) are almost totally absent in *rpgrip1l*$^{-/-}$ scoliotic fish (I-I'), while they are present in straight r*pgrip1l*$^{-/-}$(H-H') and controls (G-G''). Cilia of hindbrain mono-ciliated cells in *rpgrip1l*$^{-/-}$ (F'', G'') and controls (G''). Scale bars: 10 µm for F-I, 2 µm for F'-H', 1 µm for F'', G'', H"" and H'''.

1585 **Supplementary figure S2: Presence of scospondin aggregates and**
1586 **heterogenous ciliary defects in the fChP of *rpgrip1l*$^{-/-}$ juvenile fish.**

1587 **(A-D)** Immunostaining on transverse sections of the SCO, at anterior level (A, A', B,
1588 B') or posterior level (C, D) in *rpgrip1l*$^{+/+}$ (n=3) and tail-up *rpgrip1l*$^{-/-}$ (n=3), transgenic
1589 for Sspo-GFP (N=2). Sspo-GFP forms small cytoplasmic aggregates within SCO cells
1590 of both genotypes (* in A' and B'), under the primary cilia extending towards the DiV,
1591 and accumulates at the apical surface of tail-up *rpgrip1l*$^{-/-}$, creating a double positive
1592 area for cilia and Sspo-GFP staining (yellow in B'). Multiciliated cells lateral to the
1593 posterior SCO (mcc) are negative for Sspo-GFP staining in controls (C) and absent in
1594 tail-up *rpgrip1l*$^{-/-}$ (D). **(E-J)** GFP immunostaining on transverse section of the fChP (E-
1595 G) or at the level of the optic tectum (H-J) in *rpgrip1l*$^{+/+}$ (E, H, n=7), straight *rpgrip1l*$^{-/-}$
1596 (F, I, n=4) and scoliotic *rpgrip1l*$^{-/-}$ (G, J, n=5) 8 wpf fish transgenic for *sspo-GFP* (N=2).
1597 Scoliotic *rpgrip1l*$^{-/-}$ fish present with filamentous material and aggregates within the
1598 ventricles (G, J) while a small RF fragment is present within the ventricle of controls
1599 (H) and straight mutants (I) at optic tectum level. * indicates aggregates. **(K-O'')**
1600 Representative maximum intensity Z-stack projections of confocal transverse brain
1601 section at the level of the fChP in *rpgrip1l*$^{+/+}$ (K-K'') (n=7), straight *rpgrip1l*$^{-/-}$ (L-M'')
1602 (n=4) and scoliotic *rpgrip1l*$^{-/-}$ (N-O'') (n=5) 8 wpf fish (N=2). Cilia are stained with
1603 glutamylated-tubulin and acetylated-tubulin antibodies (both in white) and nuclei are
1604 stained with DAPI (blue). Sections shown are at the level of the habenular nuclei. At
1605 this level, monocilia in the dorsal midline region (K') and multicilia on lateral sides (K'')
1606 (n=7/7) are present in controls. Straight *rpgrip1l*$^{-/-}$ exhibited either normal (L', L'')
1607 (n=2/4) or abnormal and sparser (M', M'') (n=2/4) monocilia and multicilia. Similarly,
1608 scoliotic *rpgrip1l*$^{-/-}$ presented either normal monocilia and multicilia (N', N'') (n=3/5) or
1609 long monocilia (O') and decreased cilia density of multi-ciliated tufts (O'') (n=2/5). Scale
1610 bars: 20 µm.
1611

1612 **Supplementary figure S3: Genetic invalidation of *urp2* in *rpgrip1l*$^{-/-}$ fish does not**
1613 **have any beneficial effect on scoliosis penetrance or severity.**

1614 (A-E) Absence of compensatory upregulation of *urp* family members in *urp2*$^{-/-}$ fish.
1615 Expression levels of *urp2* (A), *urp1* (B), *urp* (C), *uts2a* (D) and *uts2b* (E) in zebrafish in
1616 13 wpf adults. Each dot represents the value measured for one fish; green and purple
1617 dots represent straight and curved fish, respectively. n = 5 [*rpgrip1l*$^{+/+}$*; urp2*$^{+/+}$], 9

1618 [*rpgrip1l*$^{+/+}$*; urp2*$^{-/-}$], 11 [*rpgrip1l*$^{-/-}$*; urp2*$^{+/-}$] and 10 [*rpgrip1l*$^{-/-}$*; urp2*$^{-/-}$]. Expression levels
1619 for each gene are compared to the *lsm12b* housekeeping gene. Statistical analysis
1620 was performed using the Tukey test where ns means not significant, ** P < 0.01, ****
1621 P < 0.0001. Error bars represent s.d. None of the *uts2* family members is significantly
1622 upregulated in [*rpgrip1l*$^{-/-}$; *urp2*$^{-/-}$] fish compared to *rpgrip1l*$^{-/-}$, suggesting an absence
1623 of compensation. **(F-G)** Quantification of body axis curvature on dorsal and lateral
1624 positions at 2 (F) and 4 (G) mpf. Each dot represents the curvature index of one fish.
1625 Statistical analysis was done using Tukey's multiple comparisons test where ****P <
1626 0.0001, with error bars representing s.d. At 2 mpf, n=30 [*rpgrip1l*$^{+/+}$*; urp2*$^{+/+}$], 26
1627 [*rpgrip1l*$^{+/+}$*; urp2*$^{-/-}$], 27 [*rpgrip1l*$^{-/-}$*; urp2*$^{+/+}$], 55 [*rpgrip1l*$^{-/-}$*; urp2*$^{+/-}$] and 32 [*rpgrip1l*$^{-/-}$*; urp2*$^{-}$
1628 $^{/-}$]. At 4 mpf, n=9 [*rpgrip1l*$^{+/+}$*; urp2*$^{+/+}$], 7 [*rpgrip1l*$^{+/+}$*; urp2*$^{-/-}$], 27 [*rpgrip1l*$^{-/-}$*; urp2*$^{+/+}$], 48
1629 [*rpgrip1l*$^{-/-}$*; urp2*$^{+/-}$] and 27 [*rpgrip1l*$^{-/-}$*; urp2*$^{-/-}$]. **(H)** Rose plots representing combined
1630 Cobb angle measurements at 4 mpf of [*rpgrip1l*$^{+/+}$*; urp2*$^{+/+}$] (n=7) in green, [*rpgrip1l*$^{+/+}$*;*
1631 *urp2*$^{-/-}$] (n=6) in blue, [*rpgrip1l*$^{-/-}$*; urp2*$^{+/+}$] (n=10) in pink and [*rpgrip1l*$^{-/-}$*; urp2*$^{-/-}$] (n=7) in
1632 yellow. Cobb angle measurements were performed on Alizarin red fish skeletons. One
1633 example of Alizarin red skeletons for each genotype is presented below its
1634 corresponding rose-plot. **(I)** Illustration of combined curvature index measurement from
1635 traced lines on lateral (left) and dorsal (right) views of fish. The curvature index of both
1636 traced lines was measured using a modified MATLAB program (LineCurvature2D
1637 function) which provided a measurement in radian/length in pixels. Scale bar: 5 mm.
1638

1639 **Supplementary Figure S4: Complementary comparative transcriptome and**
1640 **proteomic analysis of *rpgrip1l*$^{-/-}$ versus control fish.**

1641 **(A, B)** GO term analysis of biological processes enriched in *rpgrip1l*$^{-/-}$ for genes
1642 upregulated in the trunk transcriptome data (A) or enriched in *rpgrip1l*$^{-/-}$ for proteins in
1643 the brain adult proteome data (B) using Metascape. **(C)** List of the top 25 most
1644 enriched proteins in the *rpgrip1l*$^{-/-}$ vs control brain proteome. **(D)** List of selected genes
1645 upregulated in the zebrafish *rpgrip1l* trunk transcriptome and found in different reactive
1646 astrogliosis models in single cell transcriptome studies (Matusova et al, 2023).
1647

1648 **Supplementary figure S5: Increased GFAP and Annexin 2 staining and LCP1+**
1649 **cell density in different brain regions.**

1650 **(A-F')** Immunostaining of Annexin A2 (Anxa2) (A-F) and GFAP (A'- F') on transverse
1651 brain sections at habenula (A, A', D, D'), tectum (B, B', E, E') and hindbrain (C, C', F,
1652 F') levels in controls (A-C') and scoliotic *rpgrip1l*$^{-/-}$ (D-F') fish. Nuclei are stained with
1653 DAPI (blue). Scoliotic *rpgrip1l*$^{-/-}$ fish upregulate Annexin A2 and GFAP in overlapping
1654 territories. Scale bar: 20 µm. **(G)** Quantification of LCP1+ cell density in the optic
1655 tectum region of *rpgrip1l*$^{+/+}$ (n=4), straight *rpgrip1l*$^{-/-}$ (n=4) and scoliotic *rpgrip1l*$^{-/-}$ (n=3)
1656 8 wpf fish. Each dot represents a fish. 15-20 sections were counted for each brain
1657 level. Straight *rpgrip1l*$^{-/-}$ fish sections displayed around twice more Lcp1+ cells at
1658 tectum level than controls, while scoliotic *rpgrip1l*$^{-/-}$ fish had a slightly increased LCP1+
1659 cell density compared to controls. Statistical analysis was performed using Tukey's
1660 multiple comparisons test where ns means non significative and * Pvalue < 0.05, **
1661 Pvalue < 0.01 with error bars representing s.d. **(H-J')** Immunostaining of LCP1+
1662 immune cells on transverse sections of the optic tectum region of *rpgrip1l*$^{+/+}$ (H, H')
1663 (n=4), straight *rpgrip1l*$^{-/-}$ (I, I') (n=4) and scoliotic *rpgrip1l*$^{-/-}$ (J, J') (n=3) 8 wpf fish.
1664 Immune cells are labelled with the LCP1 antibody (magenta) and nuclei with DAPI
1665 (blue). H', I' and J' are higher magnifications of the squared regions in H, I and J,
1666 respectively. Scale bars: 100 µm for H, I, J; 30 µm for H', I', J'. str: straight, sco:
1667 scoliotic. **(K)** Quantification of LCP1+ cell density in the cerebellum region of 8 wpf fish
1668 (N=1). The analysis compared straight *rpgrip1l*$^{-/-}$ (n=4) and scoliotic *rpgrip1l*$^{-/-}$ (n=3) fish
1669 to *rpgrip1l*$^{+/+}$ siblings (n=4). No significant difference was found between genotypes.
1670 Statistical analysis was performed using Tukey's multiple comparisons test where ns
1671 means not significant. Error bars represent s.d. "str" means straight and "sco" means
1672 scoliotic.
1673
1674 **Supplementary figure S6: Biological assay of NACET activity on *dnaaf1*$^{-/-}$**
1675 **embryos and expression level of three immune markers at adult stage. (A)** Theta
1676 angle (θ) measurement between the eye, the caudal end of the yolk extension and the
1677 tail extremity, corresponding to the embryo curvature index. **(B)** Lateral views of 60
1678 hpf representative embryos showing axial curvature phenotypes. In untreated
1679 conditions, *dnaaf1*$^{-/-}$ embryos show a characteristic curly tail-down (CTD) phenotype,
1680 whereas *dnaaf1*$^{+/+}$ siblings have a straight axis. Treatment at 27 hpf with 3 mM NACET
1681 suppresses the CTD phenotype of *dnaaf1*$^{-/-}$ embryos and does not affect axis
1682 straightness of *dnaaf1*$^{+/+}$ siblings. Embryos were measured around 2.5 to 3 mm. **(C-F)**

1683 Rose plots representing the (360 – θ) angle of *dnaaf1*$^{+/+}$ and *dnaaf1*$^{-/-}$ in untreated and
1684 3 mM NACET-treated conditions. Embryos were treated from 27hpf to 2.5 dpf and θ
1685 angles were measured at the end of the treatment. Untreated *dnaaf1*$^{+/+}$ are
1686 represented in (C – dark green), and treated ones are in (D – light green). Untreated
1687 *dnaaf1*$^{-/-}$ are in (E – blue) and treated ones are in (F – red). NACET treatment is able
1688 to rescue curly tail down phenotype in *dnaaf1*$^{-/-}$ embryos without affecting the controls.

A

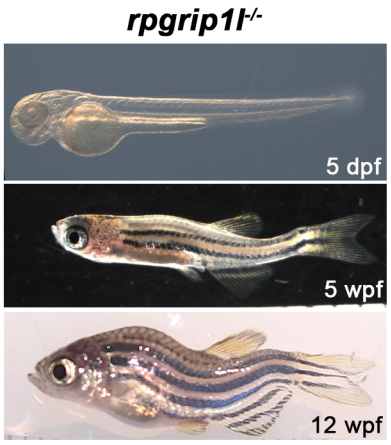

B

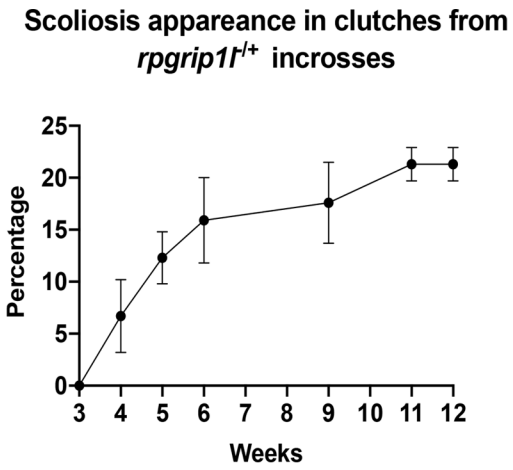

C

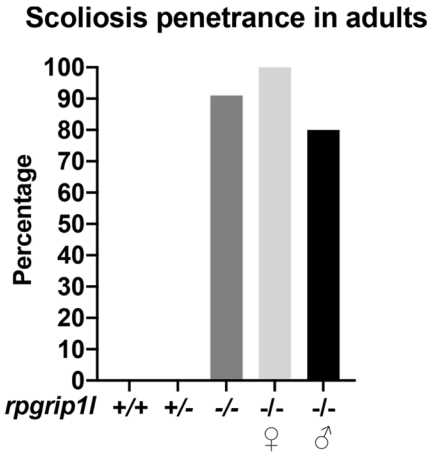

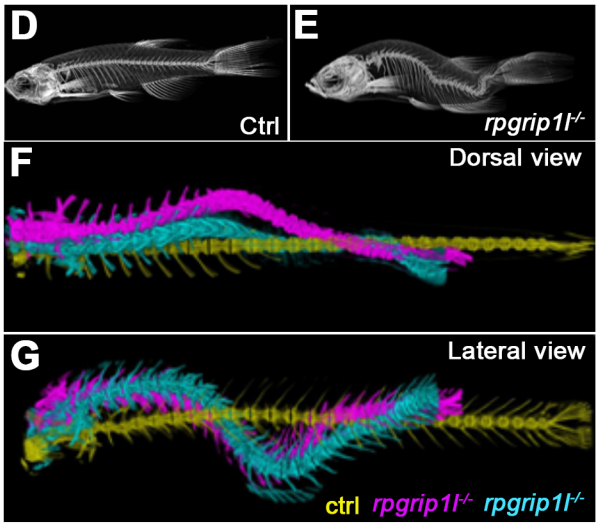

H

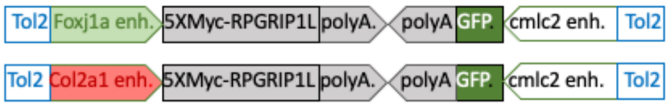

I

Genotype	*rpgrip1l*$^{-/-}$	*rpgrip1l*$^{-/-}$; Tg *Foxj1a* :RPGRIP1L	*rpgrip1l*$^{-/-}$	*rpgrip1l*$^{-/-}$; Tg *Col2a1* :RPGRIP1L
Adult Scoliotic fish (n)	72/74	0/63	28/29	28/29
Clutch (N)	N=2	N=2	N=1	N=1

J

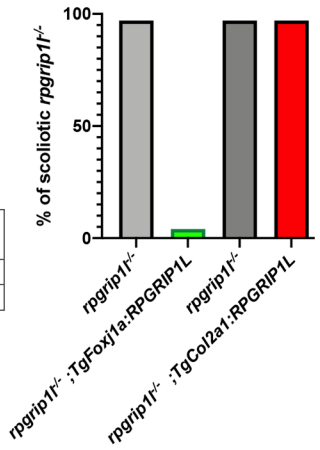

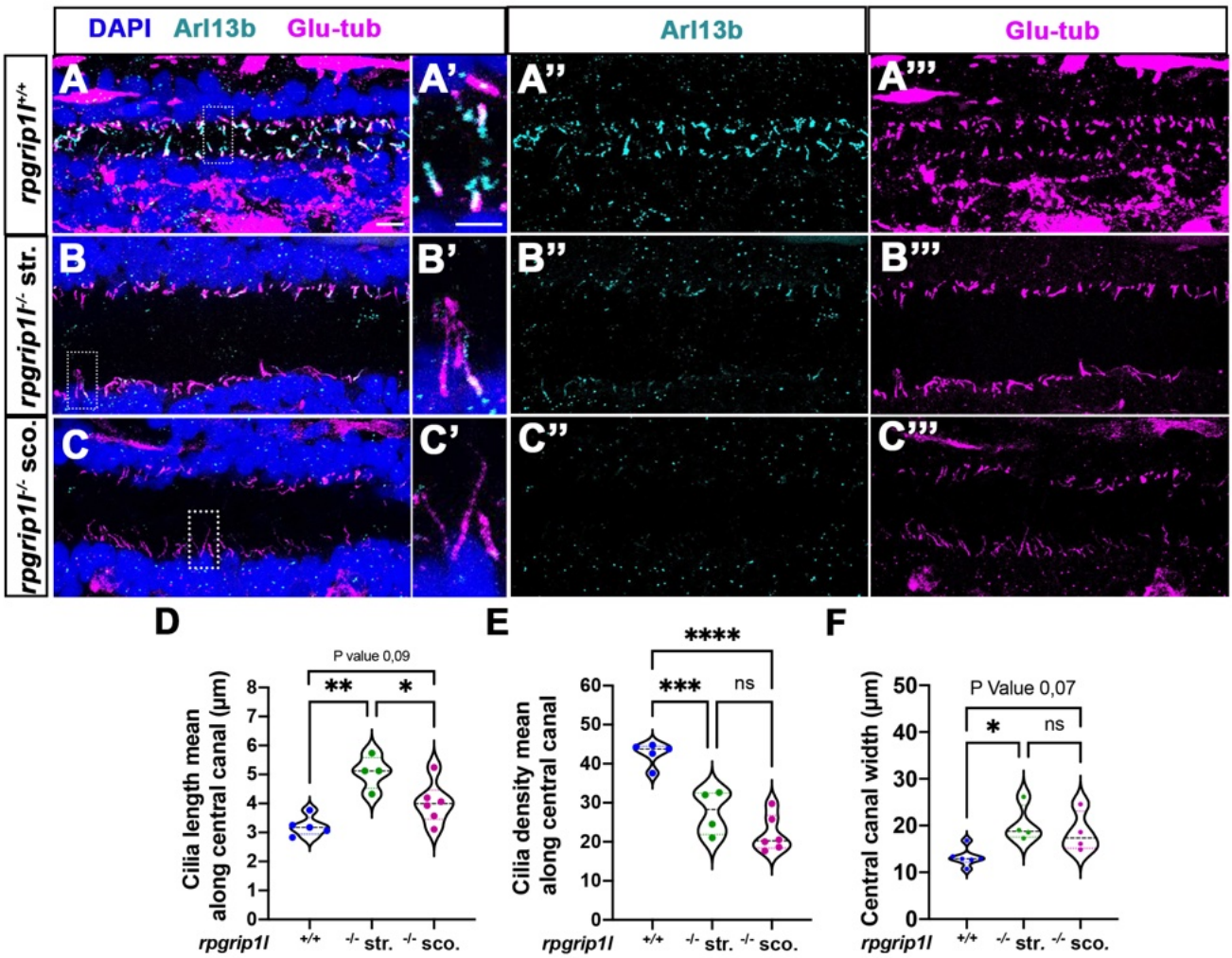
DAPI Arl13b Glu-tub
Arl13b
Glu-tub
rpgrip1l+/+
rpgrip1l-/- str.
rpgrip1l-/- sco.
A
A'
A''
A'''
B
B'
B''
B'''
C
C'
C''
C'''
D
E
F
P value 0,09
Cilia length mean along central canal (µm)
Cilia density mean along central canal
Central canal width (µm)
P Value 0,07
rpgrip1l +/+ -/- str. -/- sco.

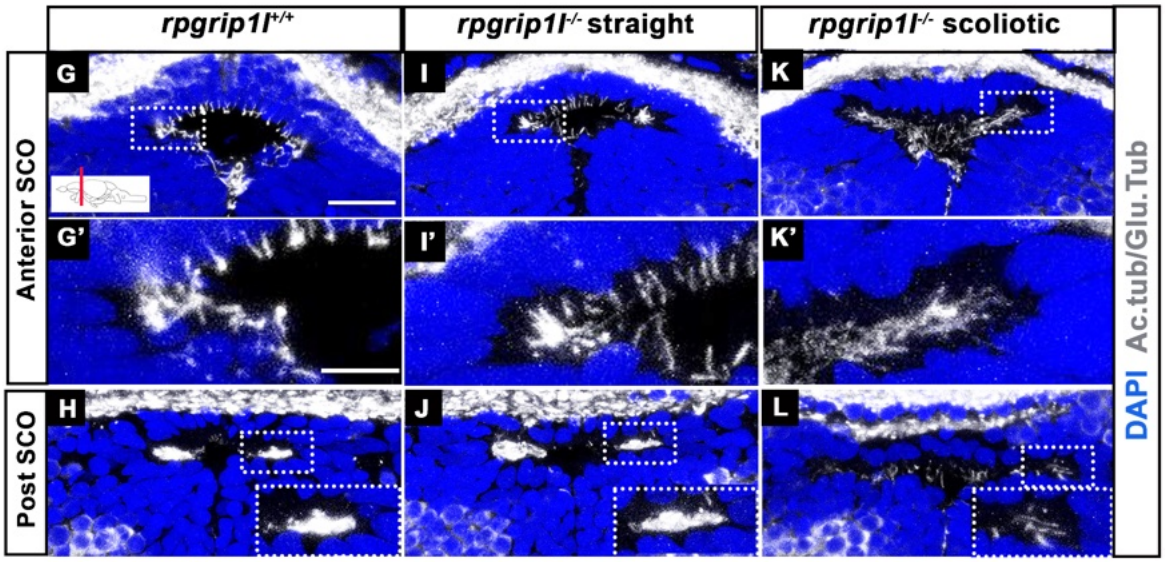
rpgrip1l+/+
rpgrip1l-/- straight
rpgrip1l-/- scoliotic
Anterior SCO
Post SCO
G
G'
H
I
I'
J
K
K'
L
DAPI Ac.tub/Glu.Tub

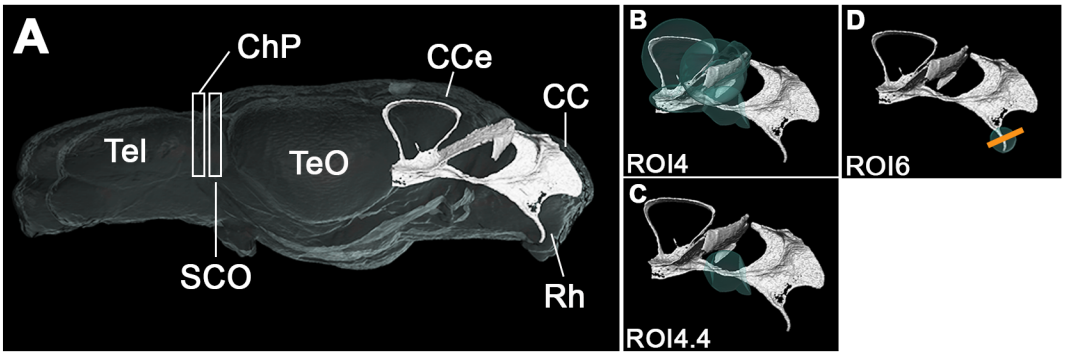
A
ChP
CCe
CC
Tel
TeO
SCO
Rh
B
ROI4
D
ROI6
C
ROI4.4

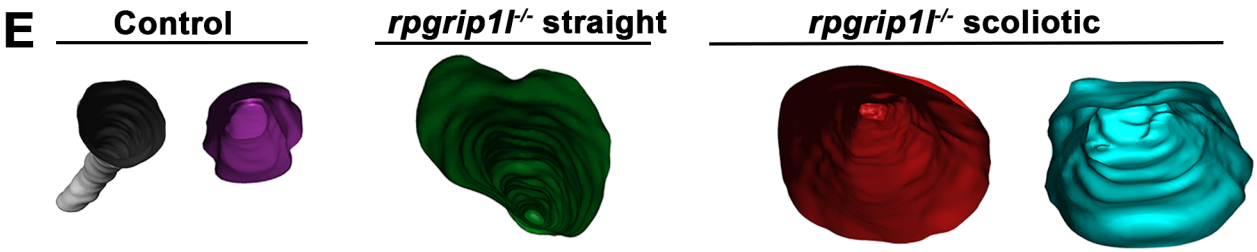
E
Control
rpgrip1l-/- straight
rpgrip1l-/- scoliotic

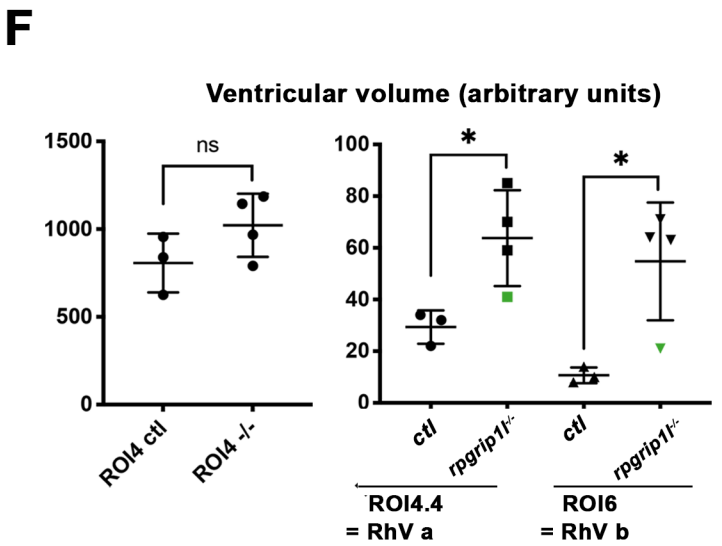
F
Ventricular volume (arbitrary units)
1500
1000
500
0
ns
ROI4 ctl
ROI4 -/-
100
80
60
40
20
0
*
*
ctl
rpgrip1l-/-
ctl
rpgrip1l-/-
ROI4.4
= RhV a
ROI6
= RhV b

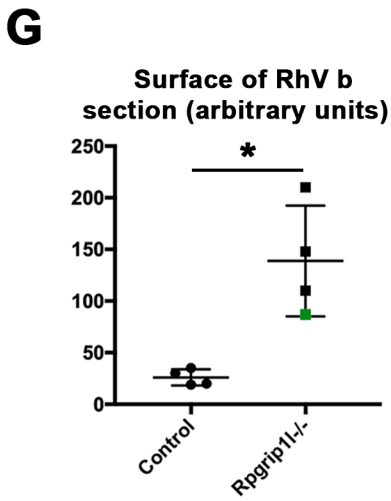
G
Surface of RhV b
section (arbitrary units)
250
200
150
100
50
0
*
Control
Rpgrip1l-/-

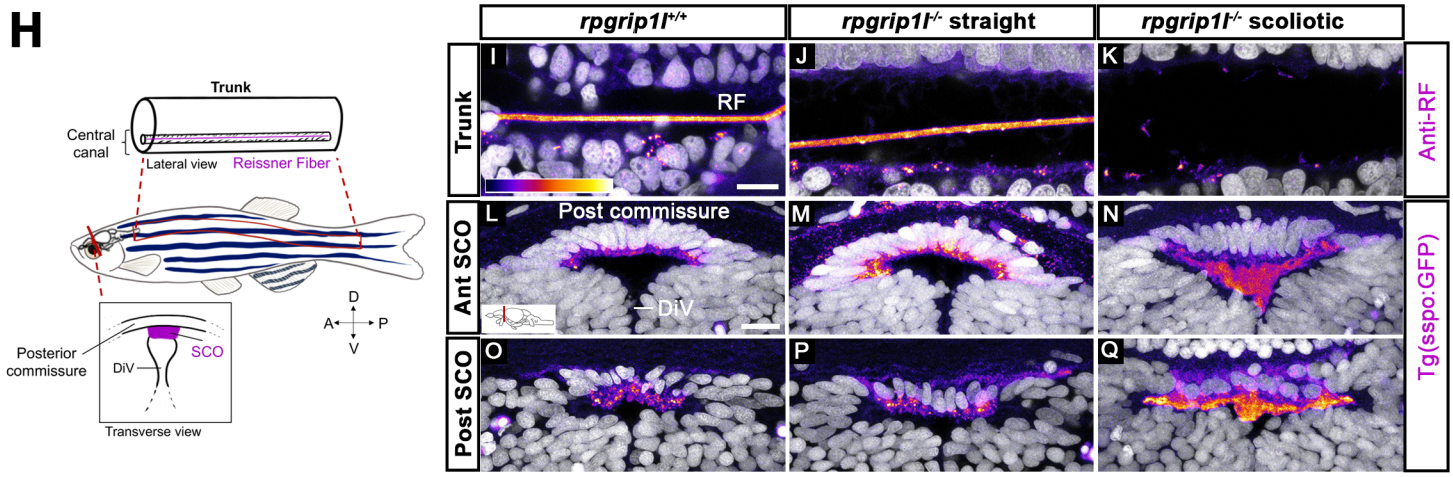
H
Trunk
Central canal
Lateral view
Reissner Fiber
Posterior commissure
DiV
SCO
Transverse view
D
A
P
V
rpgrip1l+/+
rpgrip1l-/- straight
rpgrip1l-/- scoliotic
Trunk
Ant SCO
Post SCO
I
J
K
L
M
N
O
P
Q
RF
Post commissure
DiV
Anti-RF
Tg(sspo:GFP)

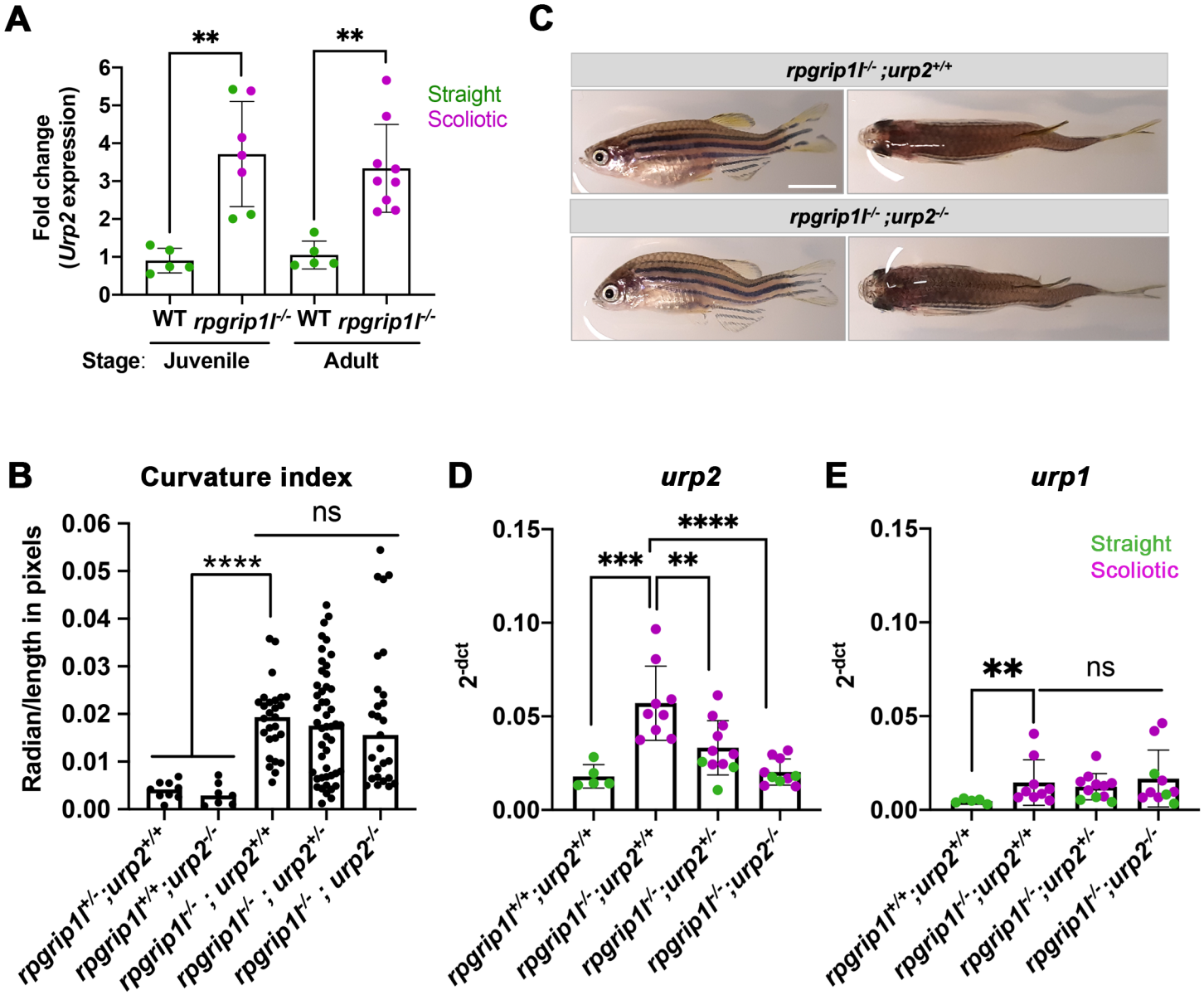
A
Fold change
(Urp2 expression)
**
**
Straight
Scoliotic
WT
rpgrip1l-/-
WT
rpgrip1l-/-
Stage: Juvenile
Adult
C
rpgrip1l-/- ;urp2+/+
rpgrip1l-/- ;urp2-/-
B
Curvature index
Radian/length in pixels
ns
****
rpgrip1l+/- ;urp2+/+
rpgrip1l+/+ ;urp2-/-
rpgrip1l-/- ; urp2+/+
rpgrip1l-/- ; urp2+/-
rpgrip1l-/- ; urp2-/-
D
urp2
2-dct
****
***
**
E
urp1
2-dct
Straight
Scoliotic
**
ns

A Brain

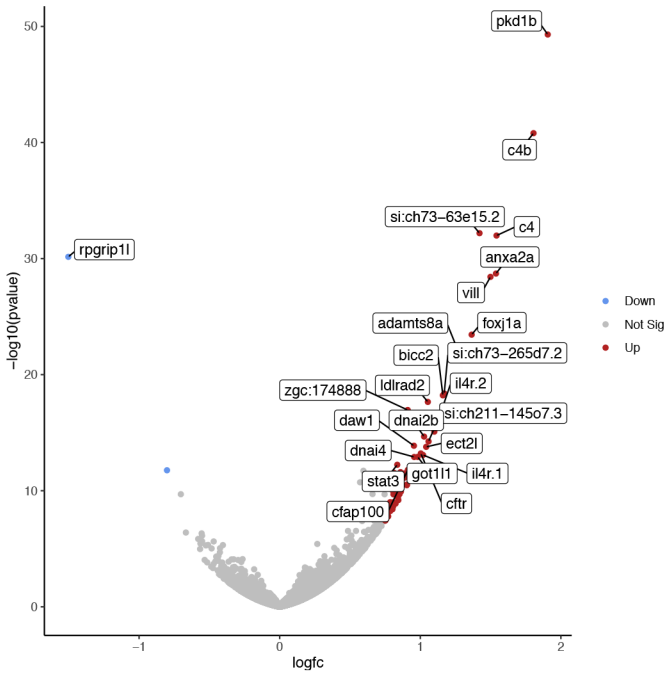

B Dorsal trunk

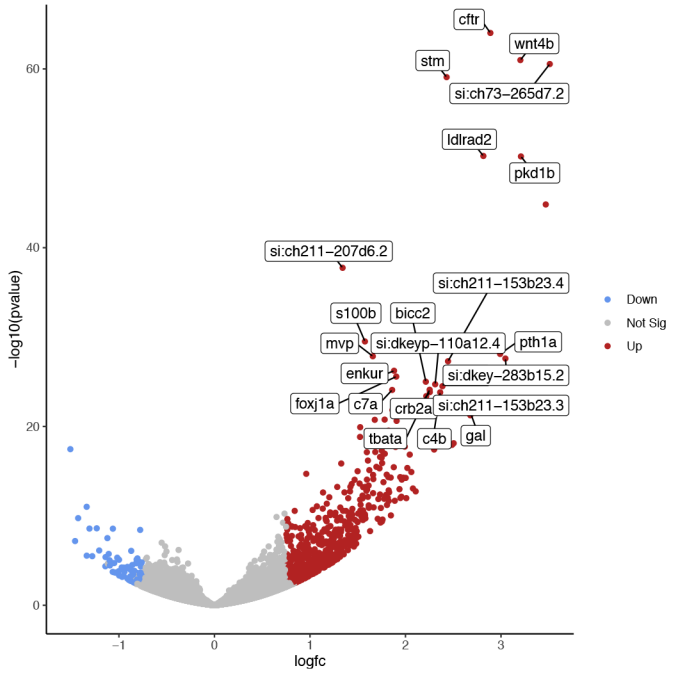

C

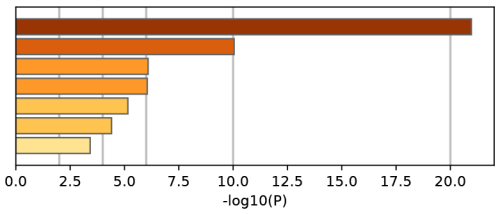

GO:0035082: axoneme assembly
GO:0001539: cilium or flagellum-dependent cell motility
GO:0002460: adaptive immune response
GO:0003351: epithelial cilium movement involved in extracellular fluid movement
GO:0007276: gamete generation
R-HSA-6785807: Interleukin-4 and Interleukin-13 signaling
GO:0045921: positive regulation of exocytosis

D Up-regulated genes

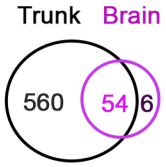

E

Process/Pathway	Gene	Trunk.LogFC	Trunk P adj.	Brain.LogFC	Brain P adj.
Foxj1a and	*tbata*	2,25	8,82E-22	0,84	1,80E-07
Its targets	*foxj1a*	1,90	3,77E-23	1,36	9,67E-21
	enkur	1,88	8,98E-24	0,76	2,13E-06
	stpg1	1,80	1,10E-09	0,69	3,00E-05
	ccdc65	1,73	8,65E-11	0,74	1,25E-05
Regulators of	*pkd1b*	3,20	2,21E-47	1,90	1,08E-45
axis curvature	*urp1*	1,92	1,32E-16	-	-
	urp2	0,96	1,22E-03	0,87	5,44E-09
	sspo	1,18	4,16E-05	-	-
Immune	*irg1l*	2,45	1,20E-16	-	-
Response	*il11a*	2,23	3,09E-16	0,67	1,21E-05
	c4	1,97	1,50E-12	1,54	5,63E-29
	anxa2a	1,52	8,15E-17	1,53	7,04E-26
	mmp9	1,00	3,94E-04	0,46	4,02E-02
	c7a	1,86	8,82E-22	0,80	9,38E-07
	stat3	0,76	3,63E-07	0,80	5,23E-10

F Brain proteome

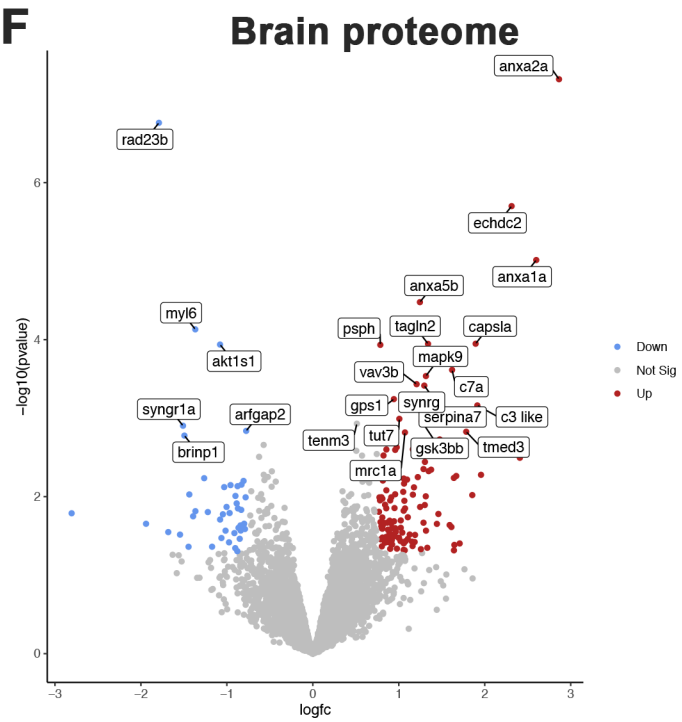

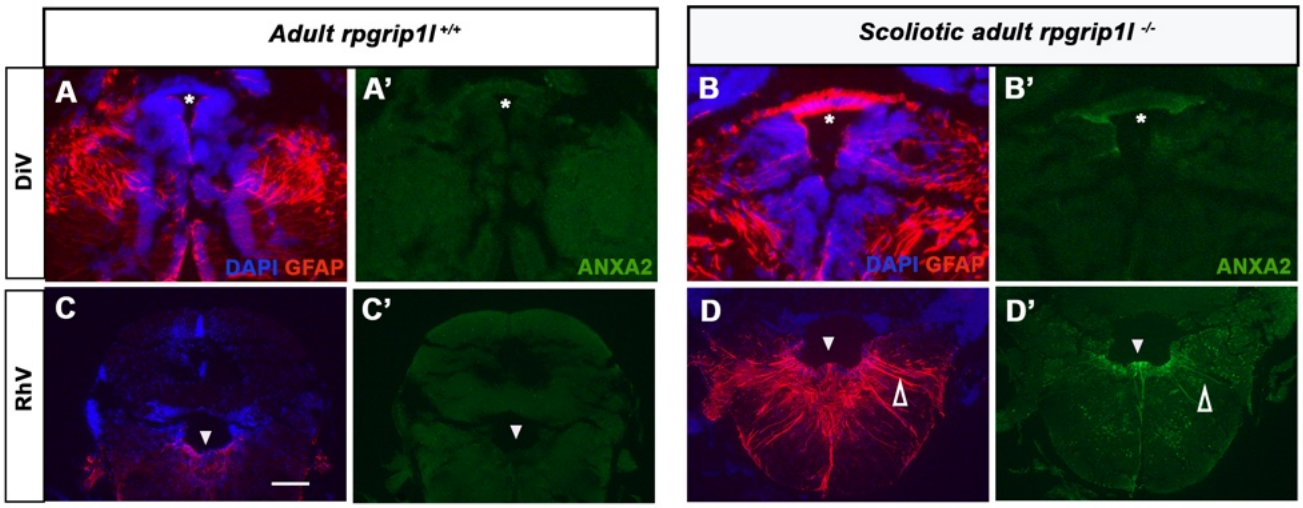
Adult rpgrip1l +/+
Scoliotic adult rpgrip1l -/-
DiV
RhV
A
A'
B
B'
C
C'
D
D'
DAPI GFAP
ANXA2

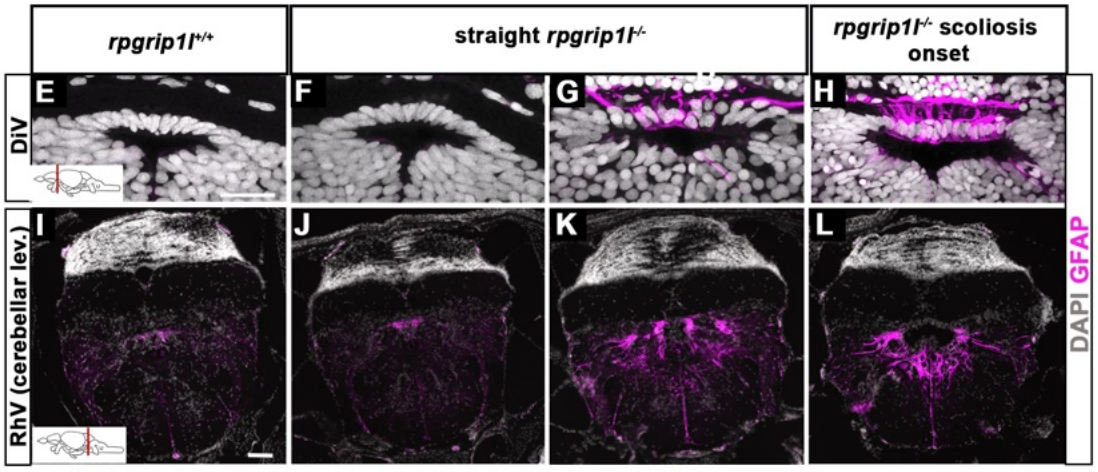
rpgrip1l+/+
straight rpgrip1l-/-
rpgrip1l-/- scoliosis onset
DiV
RhV (cerebellar lev.)
E
F
G
H
I
J
K
L
DAPI GFAP

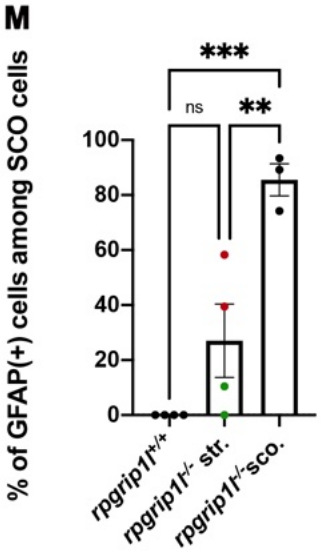
M
% of GFAP(+) cells among SCO cells
***
ns
**
100
80
60
40
20
0
rpgrip1l+/+
rpgrip1l-/- str.
rpgrip1l-/-sco.

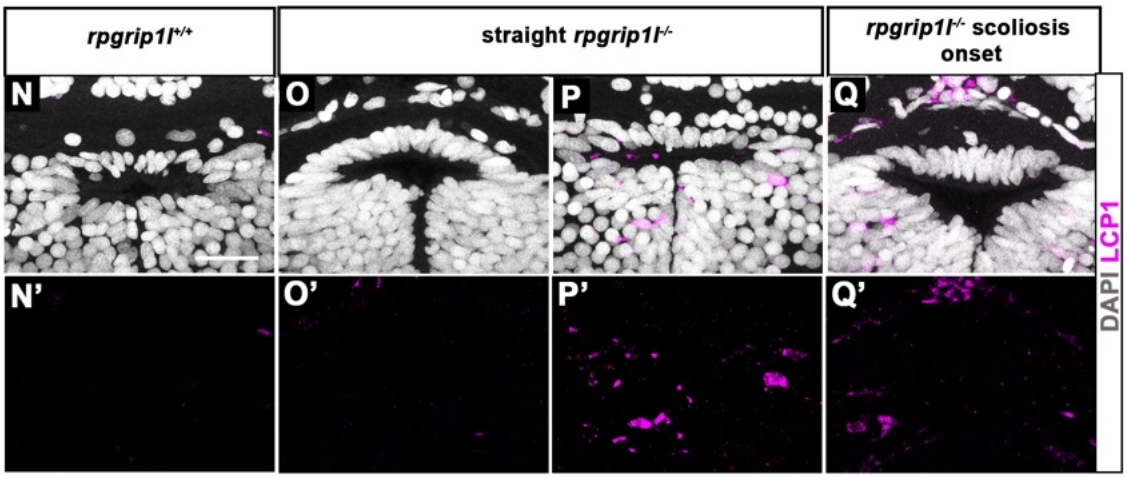
rpgrip1l+/+
straight rpgrip1l-/-
rpgrip1l-/- scoliosis onset
N
O
P
Q
N'
O'
P'
Q'
DAPI LCP1

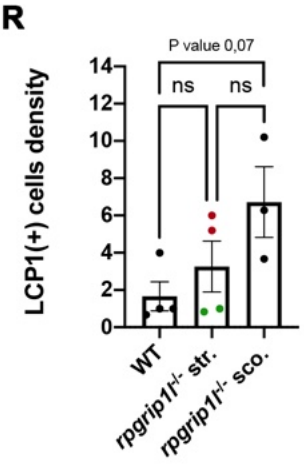
R
P value 0,07
ns
ns
LCP1(+) cells density
14
12
10
8
6
4
2
0
WT
rpgrip1l-/- str.
rpgrip1l-/- sco.

A Scoliosis penetrance in *rpgrip1l*$^{+/-}$ incross

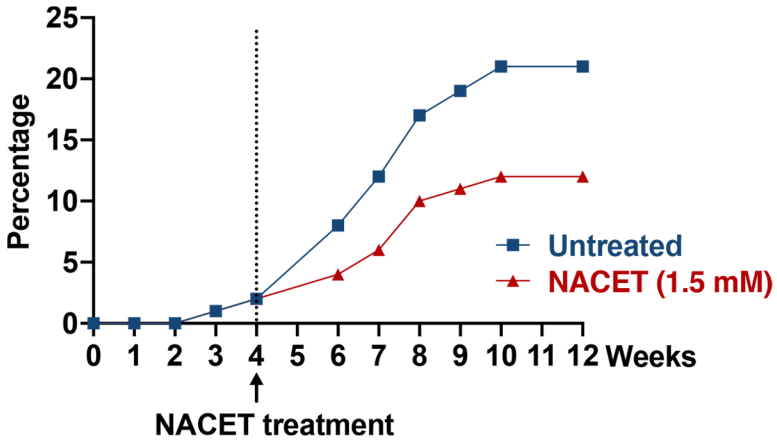

B Curvature index

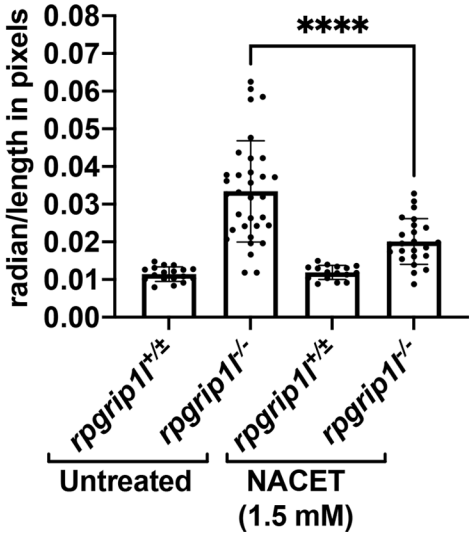

C Scoliotic phenotype and associated curvature index of *rpgrip1l*$^{-/-}$ adults

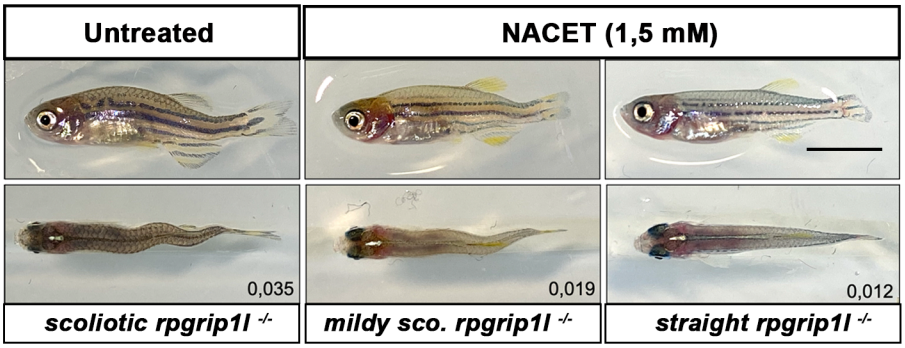

D Lcp1 cells in SCO region

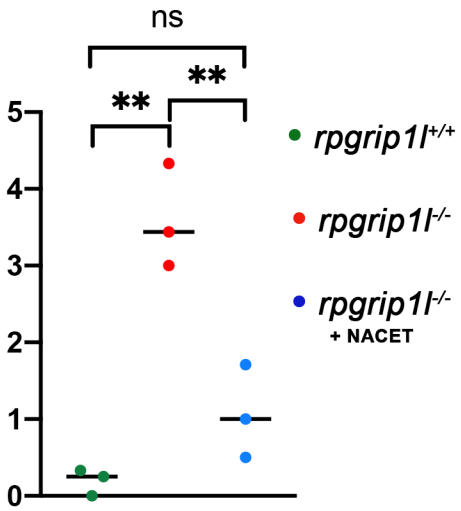

E

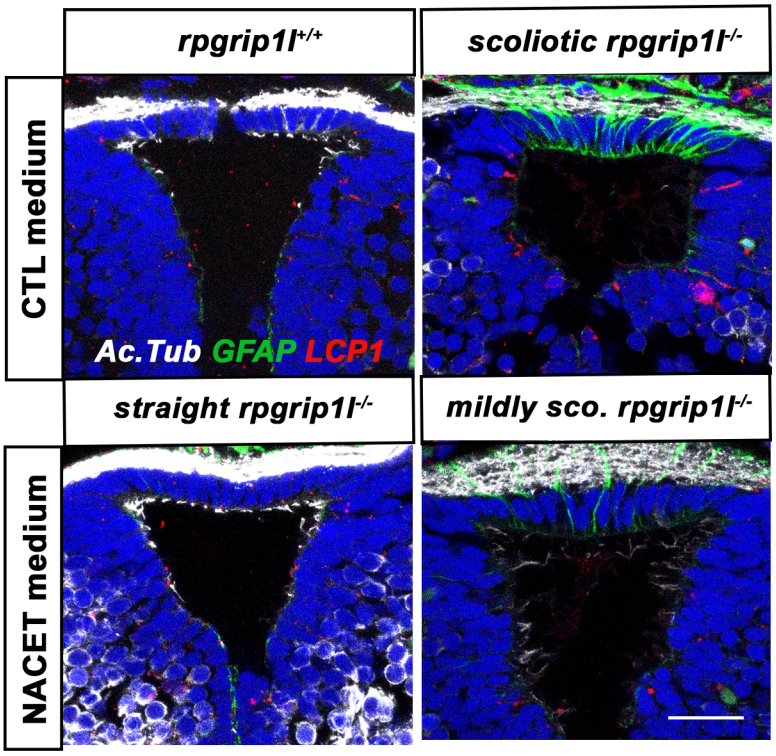

F % of GFAP(+) cells within the SCO

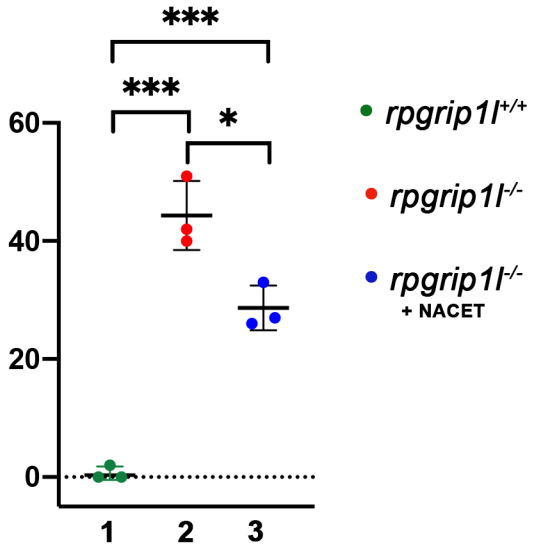

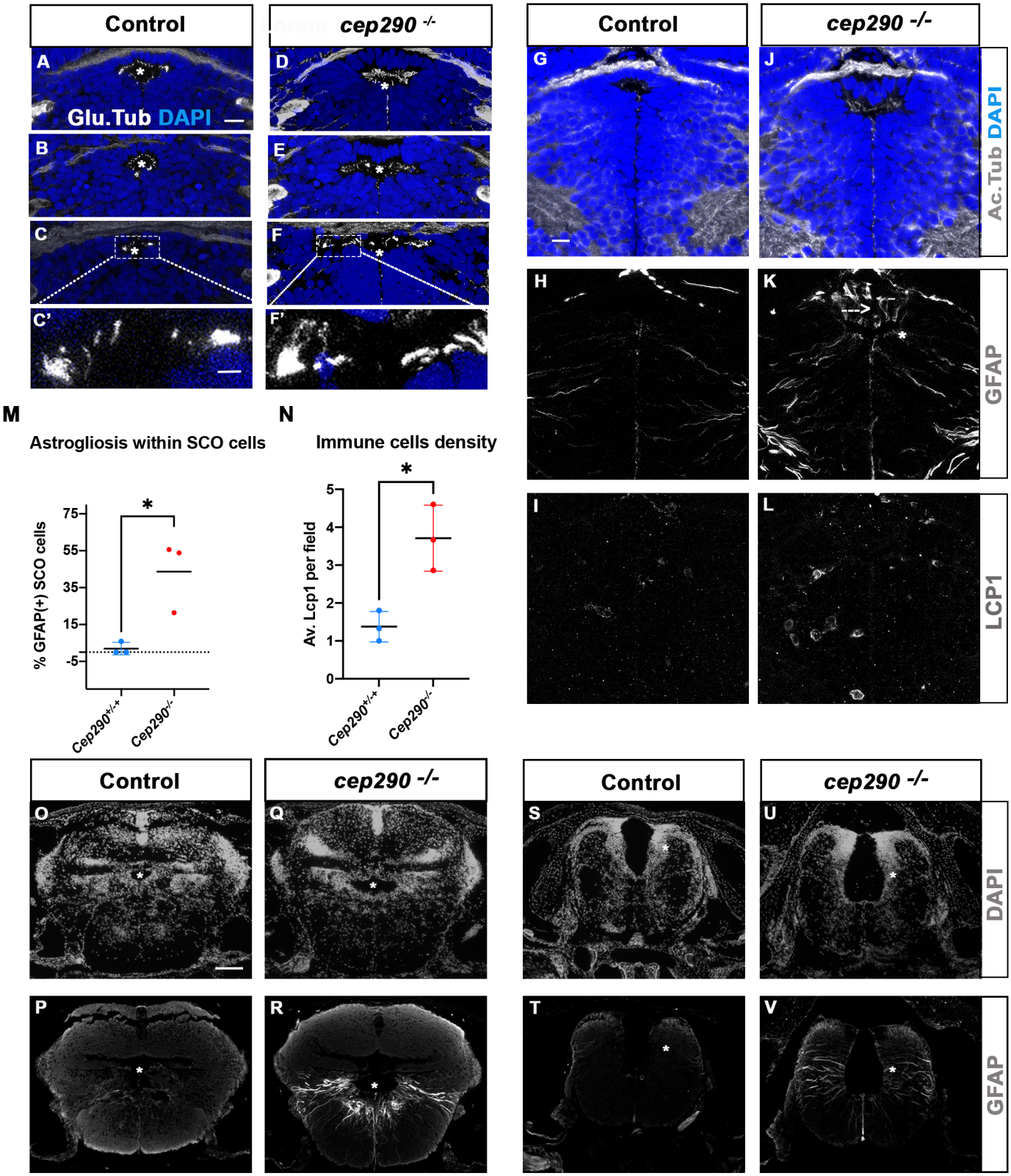
Control
cep290 -/-
A
B
C
C'
D
E
F
F'
Glu.Tub DAPI
G
H
I
J
K
L
Ac.Tub DAPI
GFAP
LCP1
M
Astrogliosis within SCO cells
% GFAP(+) SCO cells
75
55
35
15
-5
*
Cep290+/-+
Cep290-/-
N
Immune cells density
Av. Lcp1 per field
5
4
3
2
1
0
O
P
Q
R
S
T
U
V
DAPI
GFAP

A

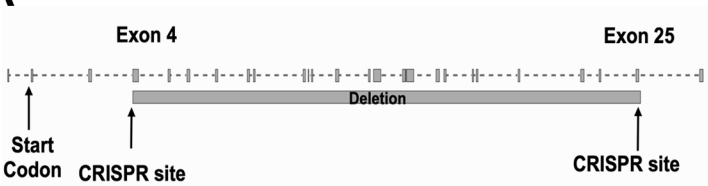

A'

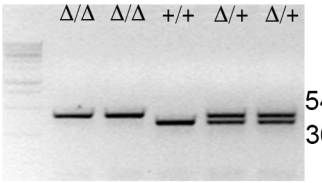

544 bp : ex4F/ex25R for MUT*
364 bp : ex25F/ex25R for WT

B

	Heart looping	Kidney cysts	Total nb embryos
wt	1	0	900
rpgrip1l $^{ex4/ex4}$	0	0	73
rpgrip1l $^{\Delta/\Delta}$	3	0	694

C

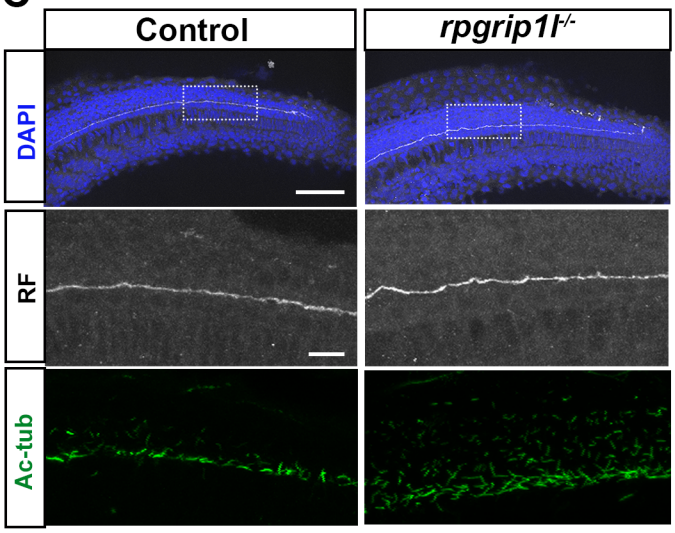

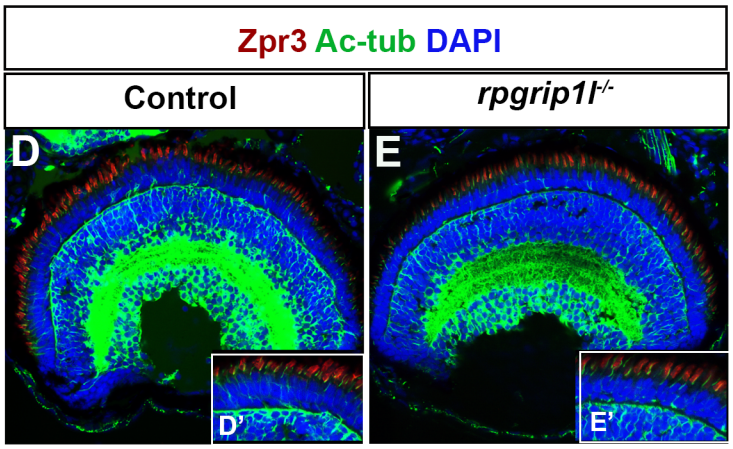

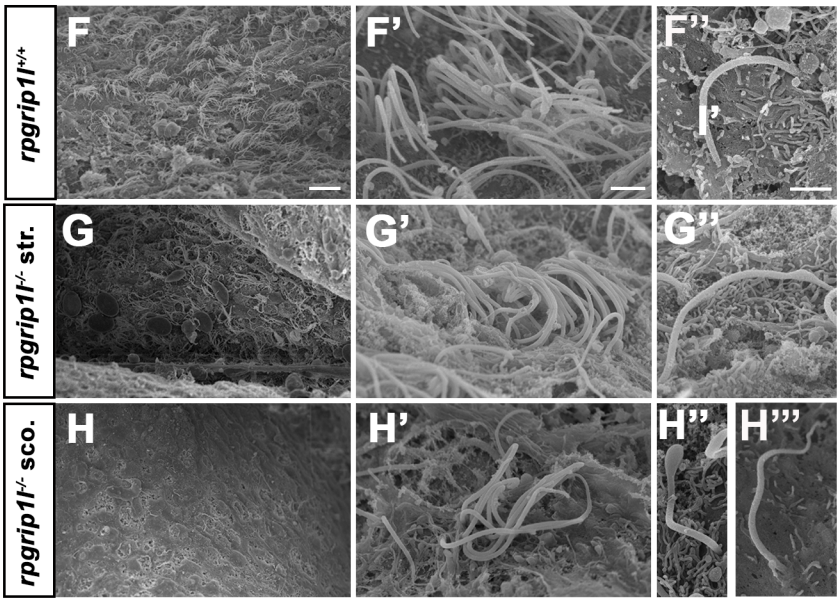

Supplementary Figure S1

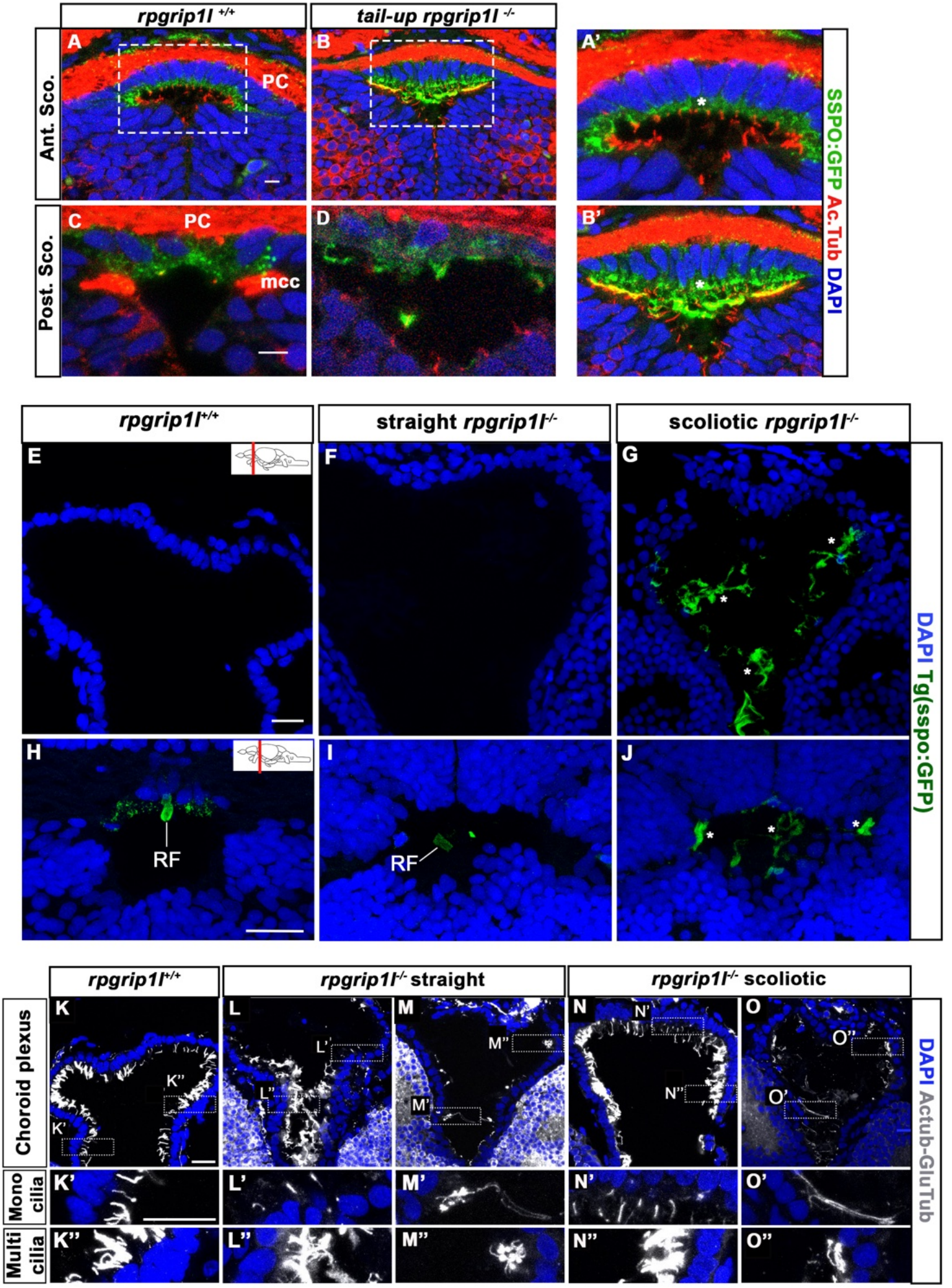

Supplementary Figure S2

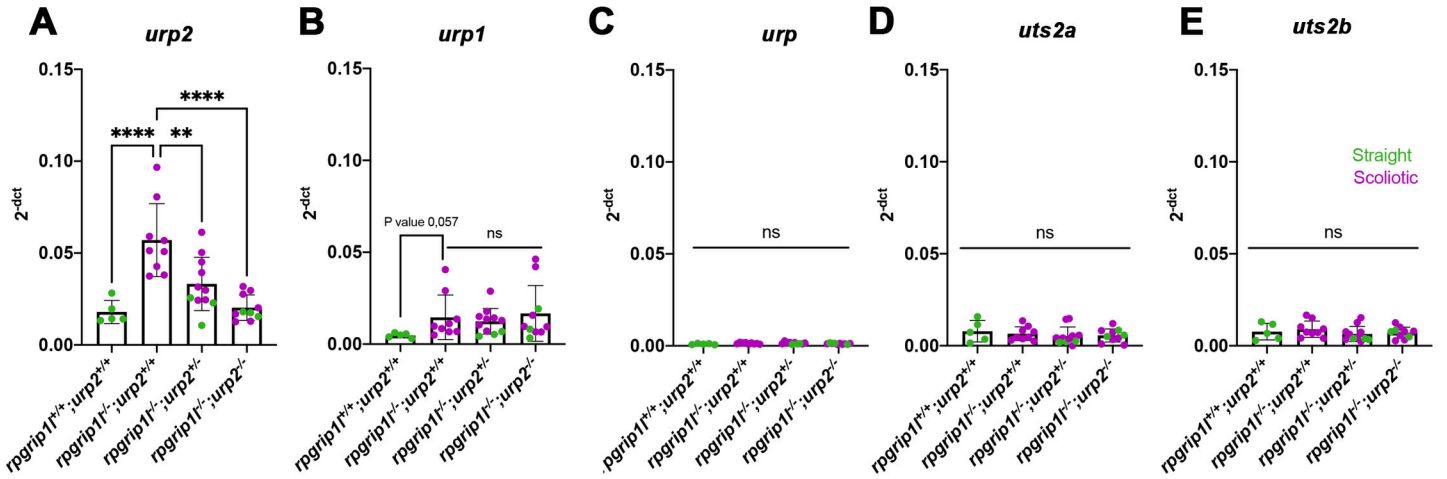

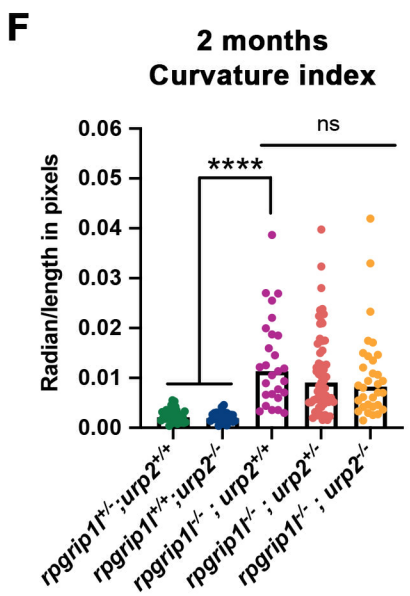

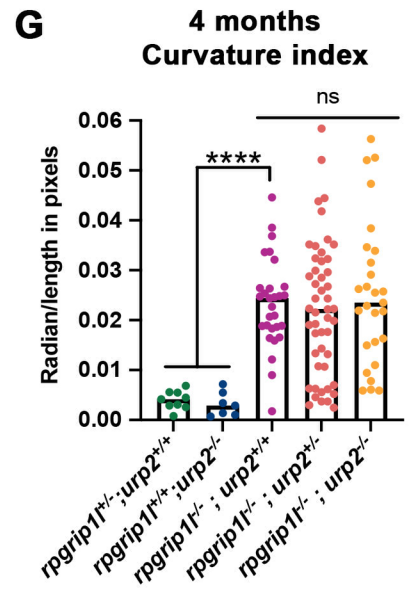

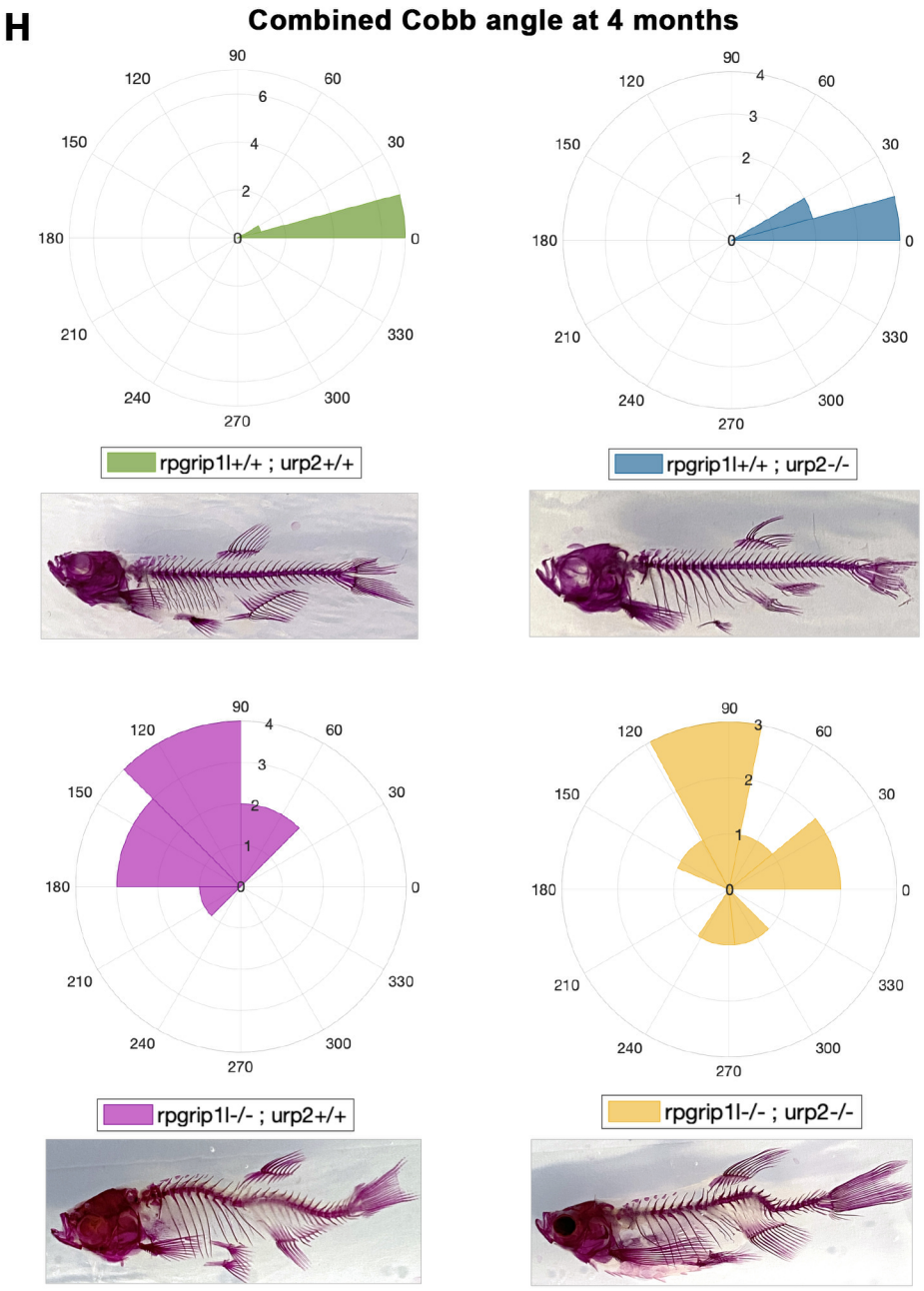

Supplementary Fig S3

A: Up-regulated genes in trunk

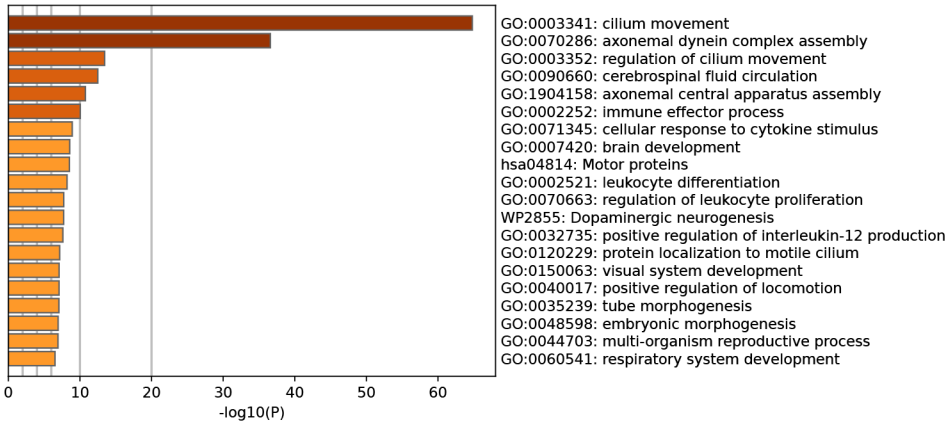

B: Enriched proteins in adult brain

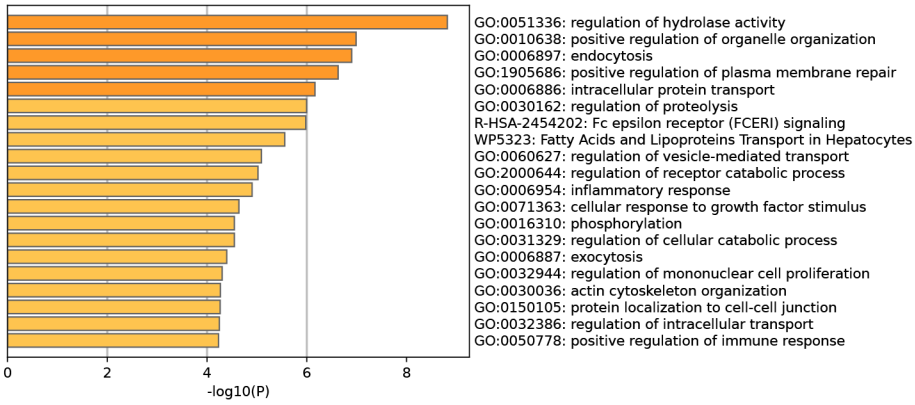

C: 25 highest P Value

Protein	FC	P value
anxa2a	7,28	4,82E-08
echdc2	4,97	1,99E-06
anxa1a	6,06	9,6856E-06
anxa5b	2,37	3,3303E-05
capsla	3,72	0,00011272
tagln2	2,53	0,00011315
psph	1,72	0,00011655
c7a	3,07	0,0002431
mapk9	2,49	0,00029106
vav3b	2,31	0,00036912
serpina7	2,46	0,0003851
gps1	1,92	0,00057247
synrg	2,08	0,00066171
c3 like	3,77	0,00068862
tut7	2,01	0,00102053
gsk3bb	2,40	0,00109597
tmed3	3,44	0,00148983
mrc1a	2,10	0,00152123
wdr12	2,78	0,00186884
wdfy2	1,97	0,00235225
plcd4b	2,24	0,00249521
itchb	1,81	0,00250875
ehd1b	1,94	0,00253596
exoc6	1,77	0,00298918
stat3	5,31	0,00319733

D: Activated astrocytes markers

Hum. Gene	Zf Gene	FC (trunk)	P.adj. Value
S100B	s100b	2,98	7,35711E-27
C4b	c4b	5,15	1,48224E-21
GFAP	gfap	2,49	1,99844E-09
CTSB	ctslb	3,60	1,29502E-08
CAPS	capsla	2,67	2,31406E-06
GLAST/SLC1A3	slc1a3b	2,68	1,46788E-05
PLCXD3	plcxd3	1,74	1,6557E-05
VIM	viml	2,14	8,30568E-05

Supplementary Figure S4

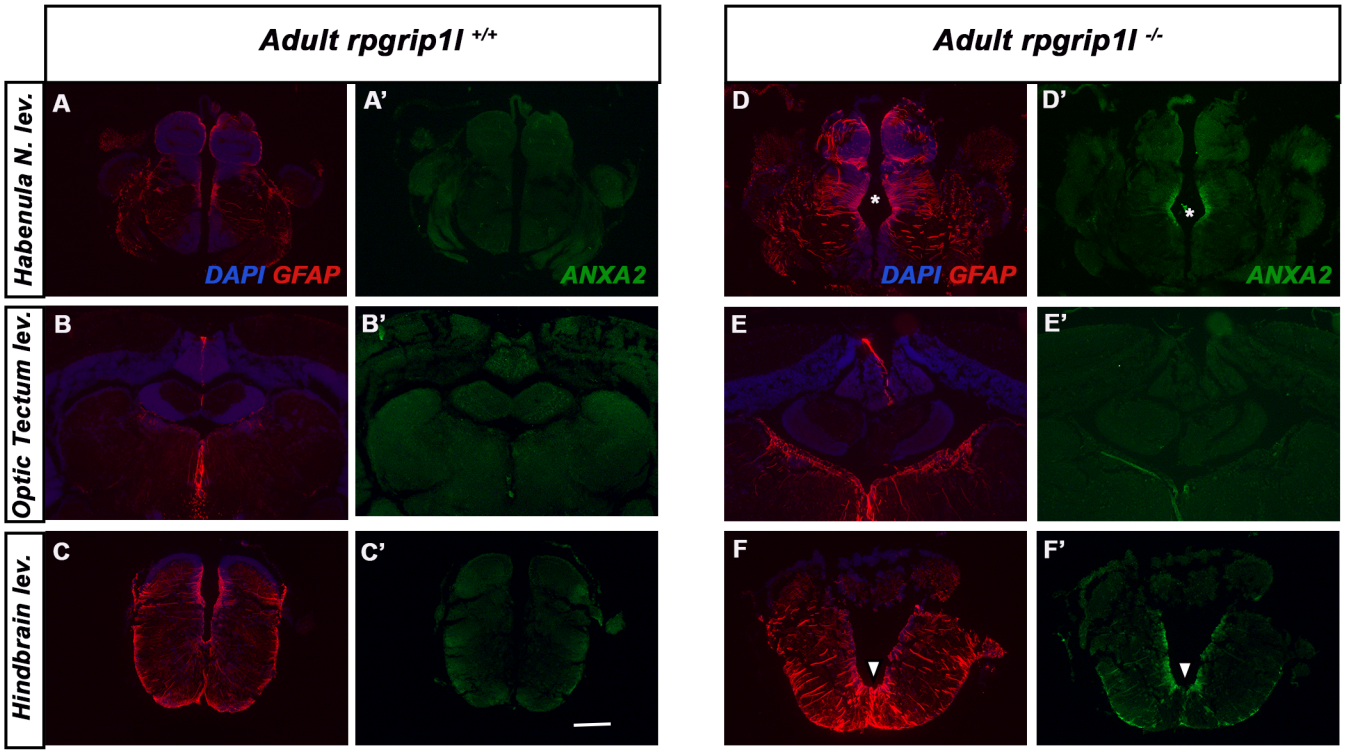

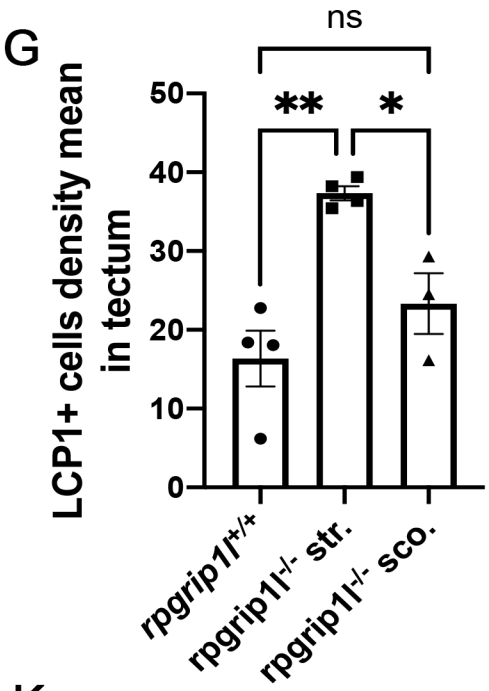

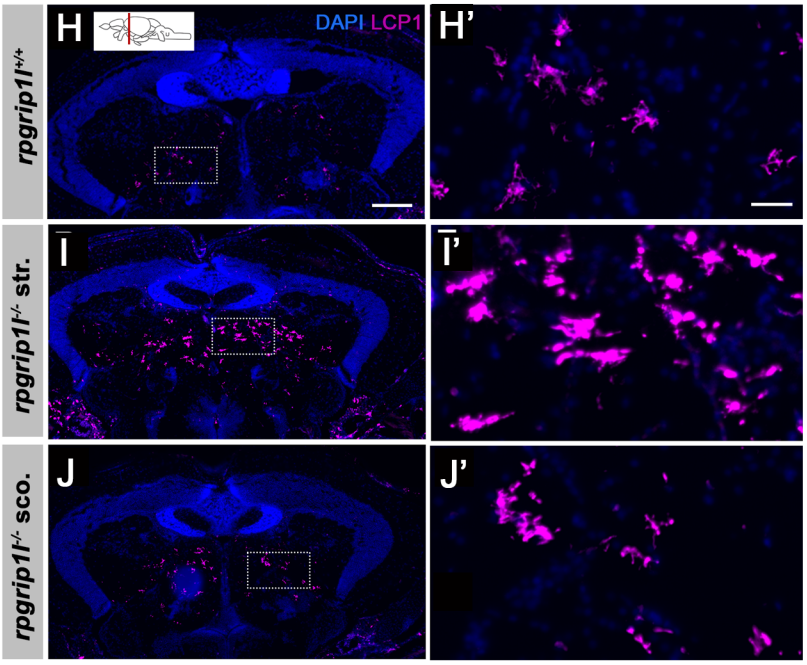

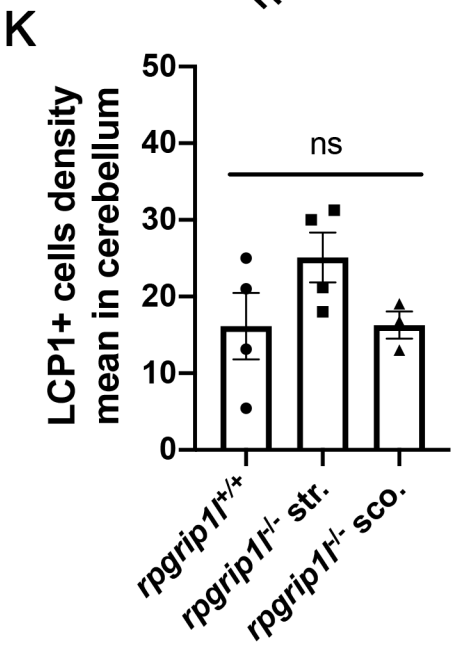

Supplementary Figure S5

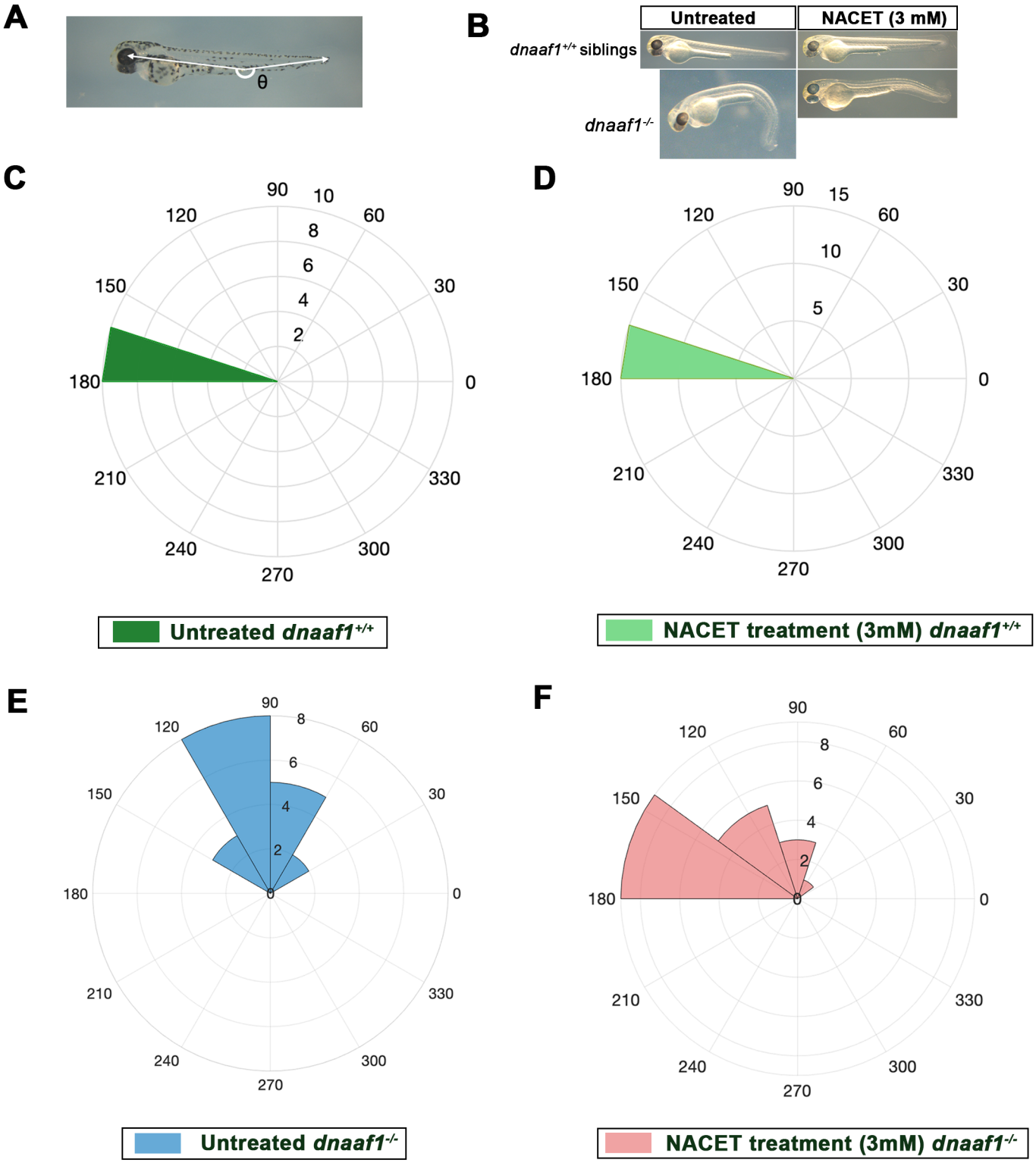

Supplementary Figure S6

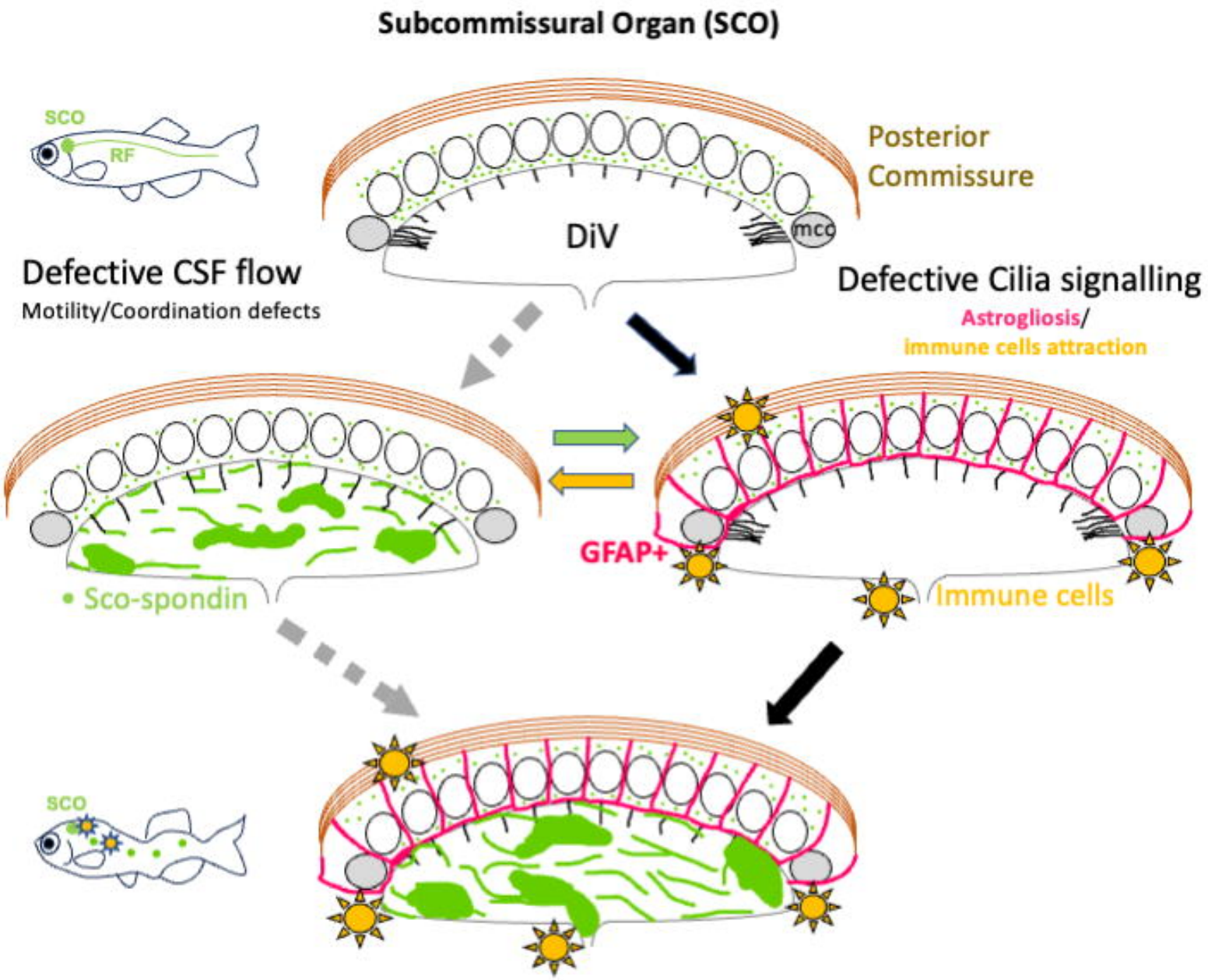
Subcommissural Organ (SCO)
SCO
RF
Posterior
Commissure
DiV
mcc
Defective CSF flow
Motility/Coordination defects
Defective Cilia signalling
Astrogliosis/
immune cells attraction
GFAP+
• Sco-spondin
Immune cells
SCO